Bayesian geoacoustic inversion and source tracking for horizontal line array data

by

Dag Tollefsen
Cand. Mag., University of Oslo, 1986
Cand. Scient., University of Oslo, 1988

A Dissertation Submitted in Partial Fulfillment
of the Requirements for the Degree of

DOCTOR OF PHILOSOPHY

in the School of Earth and Ocean Sciences

Supervisory Committee

Bayesian geoacoustic inversion and source tracking for horizontal line array data

by

Dag Tollefsen
Cand. Mag., University of Oslo, 1986
Cand. Scient., University of Oslo, 1988

Supervisory Committee

Dr. Stan E. Dosso (School of Earth and Ocean Sciences, University of Victoria)
Supervisor

Dr. N. Ross Chapman (School of Earth and Ocean Sciences, University of Victoria)
Departmental Member

Dr. Michael J. Wilmut (School of Earth and Ocean Sciences, University of Victoria)
Departmental Member

Dr. Adam Zielinski (Department of Electrical & Computer Engineering, University of Victoria)
Outside Member

Supervisory Committee
Dr. Stan E. Dosso (University of Victoria)
Supervisor
Dr. N. Ross Chapman (University of Victoria)
Departmental Member
Dr. Michael J. Wilmut (University of Victoria)
Departmental Member
Dr. Adam Zielinski (University of Victoria)
Outside Member

Abstract

The overall goal of this thesis is to develop non-linear Bayesian methods for three-dimensional tracking of a moving acoustic source in shallow water despite environmental uncertainty, with application to data from a horizontal line array (HLA) of hydrophones. As a precursor, Bayesian geoacoustic inversion is applied to estimate seabed model parameters and their uncertainties.

A simulation study examines the effect of source and array factors on geoacoustic information content in matched-field inversion of HLA data, as quantified in terms of model parameter uncertainties. Bayesian geoacoustic inversion is applied to both controlled-source and ship-noise data from a HLA deployed on the seafloor in a shallow-water experiment conducted in the Barents Sea. A new approach is introduced to account for data error reduction due to averaging data over time-series subsegments (snapshots), based on empirically apportioning measurement and theory error, with effects on inversion results compared to those of existing approaches. It is further demonstrated that combining data from multiple, independent time-series segments (for a moving source) in the inversion can significantly reduce geoacoustic parameter uncertainties. Geoacoustic uncertainties are also shown to depend on ship range and orientation, with

lowest uncertainties for short ranges and for the ship stern/propeller oriented toward the array. Sediment sound-speed profile and density estimates from controlled-source and ship-noise data inversions are found to be in good agreement with values from geophysical measurements.

Two non-linear Bayesian matched-field inversion approaches are developed for three-dimensional source tracking despite environmental uncertainty. Focalization-tracking maximizes the posterior probability density (PPD) over track and environmental parameters. Synthetic test cases show that the algorithm substantially outperforms tracking with poor environmental estimates and generally obtains results close to those achieved with exact environmental knowledge. Marginalization-tracking integrates the PPD over environmental parameters to obtain joint marginal distributions over source coordinates, from which track uncertainty estimates and the most probable track are extracted. Both approaches are applied to data from the Barents Sea experiment. Focalization-tracking successfully estimates the tracks of the towed source and a surface ship in cases where simpler tracking algorithms fail. Marginalization-tracking generally outperforms focalization-tracking and gives uncertainty estimates that encompass the true tracks.

Table of Contents

List of Tables

List of Figures

List of Abbreviations

ASSA	adaptive simplex simulated annealing
CSDM	cross-spectral density matrix
CW	continuous-wave
DHS	downhill simplex
ESNR	equivalent signal-to-noise ratio
GA	genetic algorithms
GS	Gibbs sampling
HLA	horizontal line array
HPD	highest probability density
IP	integrated probability
KS	Kolmogorov-Smirnov
MA	Metropolis algorithm
MAP	maximum a posteriori
MD	mean deviation
MFI	matched-field inversion
MFP	matched-field processing
MHS	Metropolis-Hastings sampling
ML	maximum likelihood
PAS	probability ambiguity surface
PAT	probability of acceptable track
PPD	posterior probability density
SA	simulated annealing
SNR	signal-to-noise ratio
SSP	sound-speed profile
VLA	vertical line array

Acknowledgments

I would like to thank my supervisor Dr. Stan E. Dosso for his expert guidance and support throughout the development of this thesis. Next, I thank Dr. N. Ross Chapman for introducing me to the area of geoacoustic inversion and kindly hosting my early visits to UVic, and Dr. Michael J. Wilmut for many discussions regarding the present work.

Colleagues and superiors at Forsvarets forskningsinstutt are acknowledged for their support to the pursuit of this thesis.

Til minne om min far,
Dr. Odont. Tore H. Tollefsen

Chapter 1 Introduction

Localizing and/or tracking an unknown acoustic source in the ocean is an important and challenging problem that has received considerable attention in underwater acoustics research in recent years. Much of this research is based on the use of the matched-field processing (MFP) technique for source localization (see, e.g., Baggeroer, Kuperman, and Mikhalevsky, 1993; Tolstoy, 1993). In MFP the acoustic field measured at an array of sensors (hydrophones) is compared (matched) with simulated fields computed using a numerical propagation model over a grid of trial source positions, with the source position estimate taken to be the point of maximum match (minimum mismatch) on this grid. For a moving source, additional properties of source speed and course can be derived; several matched-field tracking methods (Bucker, 1994; Wilmut, Ozard, and Brouwer, 1995; Fialkowski et al., 2001) have been proposed to estimate source track parameters.

MFP requires knowledge of the acoustic environment including water-column sound-speed profile (SSP) and seabed geoacoustic parameters, and environmental uncertainty (mismatch) can pose a severe limitation for localization (Del Balzo, Feuillade, and Rowe, 1988; Tolstoy, 1989). One approach to reducing environmental model mismatch is to carry out a geoacoustic inversion survey using controlled sources at known positions to estimate seabed parameters, e.g., by matched-field inversion (MFI) (Collins, Kuperman, and Schmidt, 1992; Dosso et al., 1993; Lindsay and Chapman, 1993; Gerstoft, 1994),

then use the estimated (fixed) seabed model in subsequent matched-field localization of unknown sources (Gingras and Gerstoft, 1995; Nicholas et al., 2004).

An alternative approach to source localization/tracking in an uncertain environment that does not require a preliminary geoacoustic survey is to treat environmental model parameters and source positions as joint unknowns. Two methods can then be applied. The first method (focalization) minimizes mismatch over all unknown parameters to obtain source position (Collins and Kuperman, 1991; Fialkowski et al., 1997) and/or track estimates (Dosso and Wilmut, 2009). The second method integrates (marginalizes) over unknown environmental parameters to obtain estimates of source positions/track parameters and their uncertainties (Richardson and Nolte, 1991; Shorey, Nolte, and Krolik, 1994; Shorey and Nolte, 1998; Tantum and Nolte, 1998; Tantum et al., 2002; Dosso, 2003; Dosso and Wilmut, 2007, 2008; Huang, Gerstoft, and Hodgkiss, 2009). In both cases, due to the strong nonlinearity of the localization/tracking problem, numerical solutions are required.

1.1. Geoacoustic inversion

Geoacoustic characterization of the seabed by inversion of acoustic data has been subject to extensive research, with perhaps the widest attention given to MFI methods that exploit the spatial coherence of the acoustic field as measured at an array of sensors (hydrophones). Early work on MFI typically employed optimization for geoacoustic models of minimum mismatch (Collins, Kuperman, and Schmidt, 1992; Dosso et al., 1993; Lindsay and Chapman, 1993; Jesus and Caiti, 1996; Tolstoy, Chapman, and

Brooke, 1998), via algorithms such as simulated annealing (SA) and genetic algorithms (GA), without rigorously assessing the non-uniqueness or uncertainty of the solutions. Subsequent work has applied a Bayesian formulation and non-linear sampling methods to the ocean acoustic inverse problem (Gerstoft and Mecklenbräuker, 1998; Dosso, 2002). In Bayesian MFI, the solution is characterized by its posterior probability density (PPD), which combines prior model information with data information obtained from an acoustic experiment. The multi-dimensional PPD is characterized in terms of its moments such as the mean, covariance and marginal probability distributions. Bayesian MFI has been applied to data from several shallow-water acoustic experiments (Dosso and Nielsen, 2002; Huang, Gerstoft, and Hodgkiss, 2006; Jiang, Chapman, and Badiey, 2007).

Much work on MFI has been performed using high-level acoustic sources and vertical line arrays (VLAs) of sensors (Dosso et al., 1993; Lindsay and Chapman, 1993; Gingras and Gerstoft, 1995; Dosso and Nielsen, 2002; Huang and Hodgkiss, 2004; Jiang, Chapman, and Badiey, 2007). Recent interest has expanded to include applications to data from horizontal line arrays (HLAs), including towed arrays (Caiti, Jesus, and Kristensen, 1996; Jesus and Caiti, 1996; Siderius, Nielsen, and Gerstoft, 2002; Battle et al., 2003, 2004; Fialkowski et al., 2006) and bottom-moored arrays (Knobles et al., 2003; Barlee, Chapman, and Wilmut, 2005; Koch and Knobles, 2005; Tollefsen, Wilmut, and Chapman, 2005), and the use of alternative sound sources such as noise from the tow-ship received on a towed array (Battle et al., 2003, 2004), or from ships-of-opportunity received on moored arrays (Chapman, Dizaji, and Kirlin, 2000; Nicholas et al., 2004; Koch and Knobles, 2005; van Leijen, Hermand, and Meyer, 2009). A towed HLA can offer the advantages of being easily deployed and mobile, but practical limitations such

as array length may limit the amount of geoacoustic information that can be extracted using this type of system. An HLA on the seabed can be a preferable choice of instrument from the point of view of array stability, covertness, ease of deployment, and sustainability to shipping activity. In both cases, HLAs sample the horizontal (radial) structure of rather than the vertical structure of the interference field of the propagating acoustic modes, and may have different characteristics for geoacoustic inversion than a VLA. Ship noise provides a convenient, unobtrusive acoustic source that is readily available for many inversion applications, but typically at lower signal-to-noise ratios (SNRs) and lower frequencies than controlled-source experiments.

Several studies to date have considered the effectiveness of geoacoustic inversion with an HLA in a relative and/or qualitative sense. For instance, Dosso, Wilmut, and Lapinski (2001); Siderius, Nielsen, and Gerstoft (2002); Battle et al. (2003); Knobles et al. (2003); and Tollefsen, Wilmut, and Chapman (2005) considered scatter plots of mismatch versus parameter values for the models visited in the course of an optimization-inversion to assess relative sensitivities, including multi-dimensional effects. Fialkowski et al. (2006) considered parameter means and standard deviations computed from multiple inversions of the same data set to obtain a measure of the uncertainty inherent in the inversion algorithm itself. HLA factors that have been considered (in the context of towed arrays) include the effect of array length and number of sensors (Jesus and Caiti, 1996), source-array separation (Battle et al., 2003), and array shape (Battle et al., 2004; Fialkowski et al., 2006). However, such sensitivity studies essentially consider the relative effect of experiment factors on the acoustic data, while the problem of interest is the absolute effect of these factors on the geoacoustic parameter estimates.

The use of ship noise in MFI reduces environmental impact over a controlled source. The use of moored arrays and noise from ships-of-opportunity allows for unobtrusive geoacoustic characterization, and has further advantages over the use of a towed array in terms of simplicity and economy, i.e., a dedicated tow-ship is not required. Geoacoustic inversion using noise from ships of opportunity and a VLA has been reported by Chapman, Dizaji, and Kirlin (2000) who applied MFI to broadband ship noise, and by Nicholas et al. (2004) who applied MFI to narrowband noise from a research ship. Koch and Knobles (2005) used broadband noise from a ship endfire to a bottom-moored HLA for geoacoustic inversion, and provided a qualitative discussion of the shape of the distributions of model samples collected via simulated annealing. However, no work to date has provided a quantitative assessment of the information content of ship noise for geoacoustic inversion in terms of rigorous parameter uncertainty estimation, including how information content varies with ship range and orientation, and with number of data observations.

1.2. Source localization

In its original formulation, the method of focalization (Collins and Kuperman, 1991) searched for environmental model parameters and a single source position through a series of parameter and coordinate perturbations driven by the global search method of simulated annealing. This approach was designed for improved source localization, without necessarily obtaining the correct environmental parameters due to the non-uniqueness of the acoustic inverse problem. Subsequent formulations (Fialkowski et al.,

2001) used environmental parameter perturbations with source coordinates searched exhaustively over ambiguity surfaces (range-depth grids of match between measured and modelled acoustic fields). Focalization has recently been extended to two-dimensional (2D) tracking of a moving source, with an efficient Bayesian focalization-tracking approach developed and applied to synthetic data on a VLA (Dosso and Wilmut, 2009).

Bayesian marginalization approaches to source localization in an uncertain environment are based on integrating the PPD over uncertain environmental parameters to produce joint marginal probability distributions over source (range and depth) coordinates (Richardson and Nolte, 1991; Shorey, Nolte, and Krolik, 1994; Dosso, 2003; Dosso and Wilmut, 2007; Huang, Gerstoft, and Hodgkiss, 2009). The joint distributions are used to define the most probable source location and to quantify uncertainty in localization. Bayesian source localization has been extended to Bayesian source tracking in an uncertain environment (Tantum and Nolte, 1998; Dosso and Wilmut, 2008), for consecutive data observations and with prior constraints on source motion applied. Applications to experimental data include source localization (Shorey and Nolte, 1998; Dosso and Wilmut, 2007) and source tracking (Tantum et al., 2002) using data from a VLA in shallow water.

1.3. Outline of work

The overall goal of this thesis is to develop methods for estimating source track parameters and their uncertainties applicable to data collected with a bottom-moored HLA in shallow water. This includes developing methods for estimation of seabed

geoacoustic parameters and their uncertainties for use in matched-field localization, as well as developing three-dimensional (3D) focalization and marginalization approaches to source tracking in an uncertain environment.

All methods are applied to acoustic data recorded on a bottom-moored HLA (18-element array of length 900 m) in an experiment conducted by the Norwegian Defence Research Establishment in shallow waters of the Barents Sea in 2003. This comprises data due to a continuous-wave towed acoustic source and ship noise due to the R/V H U SVERDRUP II for several bearings and ranges with respect to the array. The Barents Sea 03 data set also contains geophysical data including echo-sounder, bottom-penetrating sonar, gravity core, and seismic reflection and refraction data collected at the experiment site and used to provide independent information on sea bottom properties.

The remainder of this thesis is organized into seven chapters, followed by a summary. The outline of the thesis is as follows: Chapter 2 contains a description of the acoustic experiment. Chapter 3 outlines Bayesian inversion theory as applied in this thesis. Chapter 4 uses simulated data to examine the geoacoustic information content of HLA data dependence on experimental factors. Chapter 5 applies Bayesian geoacoustic inversion to controlled-source experimental HLA data. Chapter 6 applies Bayesian geoacoustic inversion to ship-noise experimental HLA data. Chapter 7 develops a focalization approach to 3D source track estimation for HLA data. Chapter 8 develops a marginalization approach to 3D source track parameter and uncertainty estimation for HLA data. Chapters 4–8 are more fully described below.

Chapter 4 (Tollefsen and Dosso, 2007) examines the effectiveness of HLAs for MFI by quantifying geoacoustic information content for a variety of experiment and array factors,

including array length and number of sensors, and source range and bearing. The effects of source frequency content and SNR are also considered, and HLA and VLA performances are compared. Geoacoustic information content is quantified in terms of marginal posterior probability distributions for model parameters computed via numerical integration within a Bayesian inversion framework. This produces a quantitative estimate of the geoacoustic parameter uncertainties which can be directly compared for various experiment/array factors. A similar approach has been applied to study VLA inversion characteristics (Dosso and Wilmut, 2002). The emphasis in this chapter is on bottom-moored HLAs and controlled-source data; however, comparisons are also made to inversions using a towed HLA, a VLA, and ship-noise data.

Chapter 5 (Tollefsen, Dosso, and Wilmut, 2006) applies Bayesian MFI to acoustic data recorded on a bottom-moored HLA due to a low-level continuous-wave towed source in the Barents Sea 03 experiment. The Bayesian inversion method consists of estimating parameter values, mean deviation uncertainties, marginal probability distributions, and inter-parameter correlations for a layered seabed model using a nonlinear numerical approach based on Markov-chain Monte Carlo sampling (Dosso, 2002). Inversion is applied to cross-spectral density matrices (CSDMs) formed by averaging spectra from a sequence of time-series sub-segments (snapshots). The chapter puts particular emphasis on defining the data error uncertainties (Dosso and Wilmut, 2006; Huang, Gerstoft, and Hodgkiss, 2006), and develops a new approach to quantifying errors for snapshot-averaged data. Geoacoustic parameter estimates are obtained for data collected at several source ranges and bearings and compared with data from supporting geophysical measurements and historical data from the region of experiment.

Chapter 6 (Tollefsen and Dosso, 2008a) considers geoacoustic inversion of noise from a relatively quiet surface ship collected at a bottom-moored HLA in the Barents Sea 03 experiment. A Bayesian MFI method is employed to estimate model parameters and to quantify their uncertainty distributions. This allows for meaningful comparisons of the geoacoustic information content of different data sets. The chapter demonstrates that including multiple, independent data (time-series) segments in the inversion can significantly reduce uncertainties in the geoacoustic parameter estimates. The effects of ship orientation and ship range on inversion results are also quantified and discussed. Finally, results from inversion of ship noise are compared with results from inversion of controlled-source data (Chapter 5) as well as with results from reference geophysical measurements.

Chapter 7 (Tollefsen and Dosso, 2009) develops an approach for 3D source tracking in an uncertain shallow-water environment with application to HLA data. The approach is similar to the 2D focalization-tracking algorithm developed by Dosso and Wilmut (Dosso and Wilmut, 2009), but is extended to 3D tracking with a HLA. It makes use of data from multiple source positions along the track, the adaptive simplex simulated annealing (ASSA) optimization algorithm (Dosso, Wilmut, and Lapinski, 2001), and the Viterbi algorithm (Viterbi, 1967) to determine the most probable source track within applied limits on source horizontal and vertical velocities. The method is applied to noisy synthetic data in a series of test cases that include different track geometries, varying SNRs, and varying prior information on seabed and water-column parameters. The results are evaluated in terms of the probability of estimating a track that is acceptably close to the true track. The focalization-tracking algorithm is shown to substantially

outperform tracking with poor environmental estimates, and in general obtains results close to those obtained with exact environmental knowledge. The method is also applied to data from the Barents Sea 03 data set, including narrowband data due to a continuous-wave towed source and due to ship noise at several ranges, and is shown to successfully track both the towed source and the ship in cases where simpler tracking algorithms failed.

Chapter 8 extends the 2D marginalization approach for source tracking in an uncertain environment of Dosso and Wilmut (2008) to 3D tracking using a HLA. The approach integrates the PPD over environmental parameters to obtain a sequence of joint two-dimensional (range-depth and range-bearing) marginal probability distributions, then applies the Viterbi algorithm (with source velocity constraints) to determine the most probable source track, with uncertainties estimated from the marginal distributions. The marginalization-tracking approach is applied to synthetic HLA data for test cases defined in Chapter 7, with tracking performance compared to the focalization-tracking results. The method is also applied to narrowband towed-source and ship-noise data from the Barents Sea 03 data set, with excellent approximations to the true tracks obtained.

Chapter 2 Experiment, data, and model

2.1. Acoustic measurements

The acoustic experiment analyzed in this thesis was conducted by the Norwegian Defence Research Establishment (FFI) in June, 2003, in a relatively little-surveyed area of the south-western Barents Sea. The area of the experiment represents a typical high-latitude continental-shelf environment, with the upper part of the seabed characterized by 50–100 m and more of glacigenic sediment (Eldholm and Talwani, 1977; Sættem, Rise, and Westgaard, 1991).

A 900-m long HLA was deployed on the seabed by the FFI research vessel R/V H U SVERDRUP II (55 m length overall, 400 ton displacement, 5.2 m draft) in a north-south orientation on the relatively flat seabed at a depth of approximately 282 m, as shown in Fig. 2.1. The array was comprised of 18 sensors (hydrophones), with 7 sensors spaced at 10-m intervals at the north end of the array, and sensor separation increasing over the remaining 11 elements to a maximum of 160 m at the south end. The position and orientation of the HLA were determined using travel-time measurements from an airgun source towed in a circle of 1-km radius around the center of the array. Results indicated that the array did not deviate significantly from the nominal linear configuration (Tollefsen, 2004), and a straight HLA is assumed throughout this thesis.

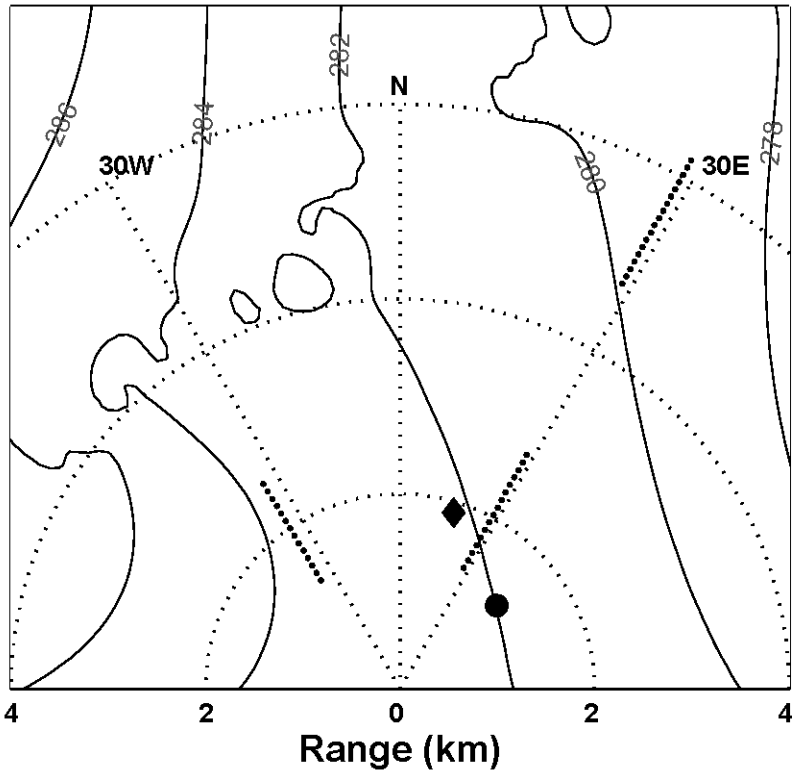

Figure 2.1: Experiment region. The HLA was laid north-south with the north end at the origin of the coordinate system. Solid lines are water depth (m) contours; dotted lines indicate range (km) and azimuth (º) to the array; heavy dotted lines indicate source/ship tracks analyzed in this thesis. The diamond indicates the location of the gravity core; the filled circle indicates the sonobuoy location for the seismic refraction experiment.

An acoustic source was towed at nominal depth of 54 m and speed of approximately 5 kn by the R/V H U SVERDRUP II along radial tracks oriented at approximately 30º angles east and west of endfire to the HLA. The ship was outbound with the stern oriented toward the array during the east track, and inbound with the bow oriented toward the array on the west track. The two tracks are henceforth referred to as the east/outbound and west/inbound tracks, as illustrated in Fig. 2.1. Ship position information was provided from a Trimble 4000 series differential global positioning

system (DGPS) receiver and logged continuously to computer disc. The ship-to-array (north end) ranges along the tracks extended from approximately 1.4 km to 6.5 km.

The acoustic source consisted of a moving-coil type transducer (Lurton, 2002) installed in a pressure-compensated tow body, producing an omni-directional low-frequency signal at maximum source levels comparable to those of a merchant ship. The source transmitted continuous-wave (CW) tones at five frequencies (simultaneously) within 30–160 Hz. Source levels were changed in steps of 6 dB at approximately 10 min intervals.

Acoustic pressure-time series at the array hydrophones were transmitted to a surface buoy via a cable, digitized at 3 kHz and transmitted from the buoy to the receiving ship via radio-frequency data link where they were recorded on computer disc. All acoustic data analyzed in this thesis were collected within a 3 h time interval. Details of the acoustic signals and signal processing are given in Chapters 5 and 6.

2.2. Environmental data

As part of the experiment, several types of supporting oceanographic and geophysical measurements were made from the R/V H U SVERDRUP II, as summarized in Fig. 2.2. Water depth measurements were recorded continuously along the source tracks with a Kongsberg EA 600 single beam echo-sounder and recorded to computer disc. Water-column temperature and salinity profiles were measured using a conductivity-temperature-depth probe (Neil Brown model 1150) at the beginning of the east track, and by expendable bathythermograph casts (Sippican Inc. model Deep Blue) from the ship along both tracks. The SSPs calculated from these measurements exhibited little variation

over time or position, and indicated a higher-speed (warmer) surface layer of approximately 1475 m/s extending to 40 m depth; below this layer the sound speed decreased abruptly to 1470 m/s then increased to 1473 m/s at the seabed; see Fig. 2.2 for a representative profile. In the inversions described in the following chapters, each acoustic track was analyzed using a SSP measured during that track. The seas were calm (sea state 1) during the experiment.

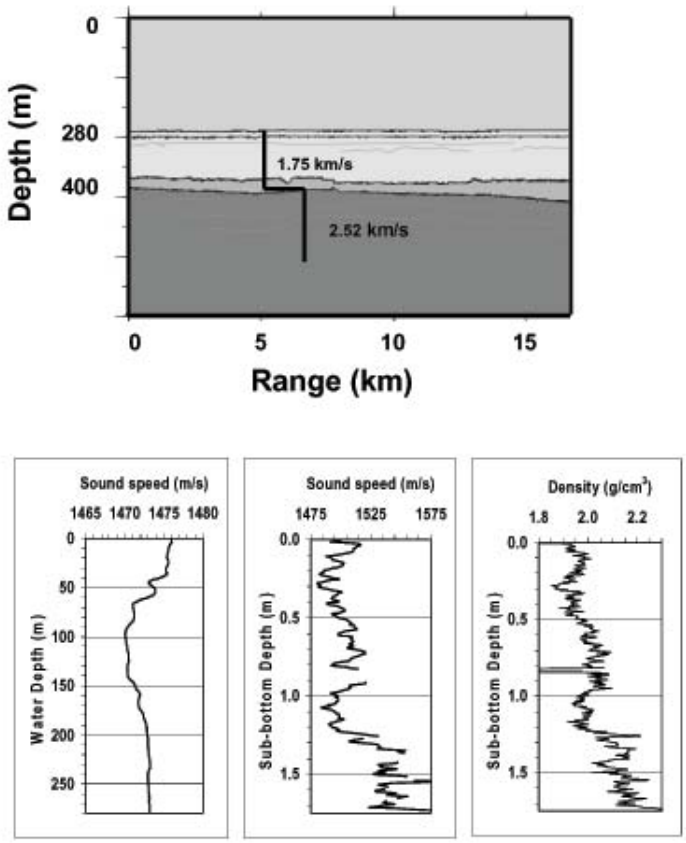

Figure 2.2: Environmental data. Upper plot: Interpreted seismic section, with inset sound-speed profile in seabed from wide-angle bottom refraction measurements; HLA (north end) located at zero range. Lower plots: Water-column sound-speed profile (left panel), and sediment sound-speed (middle) and density (right) profiles from gravity core measurements.

To obtain an indication of the sub-bottom structure, seismic-reflection and bottom-penetrating sonar data were collected simultaneously (by the R/V H U SVERDRUP II subsequent to the acoustic experiment) along a track that closely approximated the east track of the acoustic experiment. The seismic reflection survey employed a source array of two 40-cubic-in. airguns (Texas Instruments) recorded on a 10-m single-channel towed streamer. The reflection data indicate the seabed consists of an upper layer, approximately 120–140 m thick, which is interpreted to be Quaternary sediments, overlying several layers of consolidated (Triassic) sediments (Solberg, 2004). Data from a Kongsberg TOPAS PS 18 parametric sub-bottom profiling sonar, operated with a frequency-modulated sweep at frequencies of 2–4 kHz (pulse length 20 ms), suggested some internal structure in the sediments near the seafloor and a possible weak reflector at approximately 10–20 m depth. The seismic-reflection and sonar data, interpreted in Fig. 2.2, indicate essentially range-independent structure within the Quaternary sediments along the track.

Further estimates of the geophysical properties were obtained from a gravity core (length ~1.7 m, diameter 70 cm), analysis conducted with a GEOTEK Multi Sensor Core Logger at the University of Bergen, Norway, and a wide-angle bottom refraction survey based on recordings of the airgun source on a sonobuoy hydrophone (see Fig. 2.1 for locations). Analysis of the core indicated a silty-clay sediment composition, with sound speed (measured at 220 kHz) and density (measured by gamma ray attenuation) of approximately 1500 m/s and 2.0 g/cm^3, respectively, over the top 0.8 m, increasing to about 1520 m/s and 2.1 g/cm^3 over the lower 0.9 m (Lepland, 2004). The relatively high density values from the core measurement are consistent with values reported for

glacigenic sediments of this type from other sites in the Barents Sea (Orsi and Dunn, 1991; Sættem, Rise, and Westgaard, 1991; Lepland, 2004). Standard slope-intercept analysis of the refraction data, based on the assumption of constant-speed layers (e.g., Telford, Geldart, and Sheriff, 1990) indicated an overall sound speed of 1745 m/s for the Quaternary sediments and 2520 m/s for the Triassic sediments (Solberg, 2004).

2.3. Geoacoustic model

A simple geoacoustic model of the seabed, consistent with the geophysical data, was developed for the purposes of inversion. The seabed model (Fig. 2.3) consists of an upper layer with depth-dependent properties overlying a homogeneous halfspace. The two seabed layers are designed to represent geoacoustic variations within the upper few tens of metres of the Quaternary sediment layer. The parameters that describe the upper sediment layer are the layer thickness, h, sound speed at the top and bottom of the layer, c_1 and c_2, attenuation coefficient at the top and bottom of the layer, α_1 and α_2, and a depth-

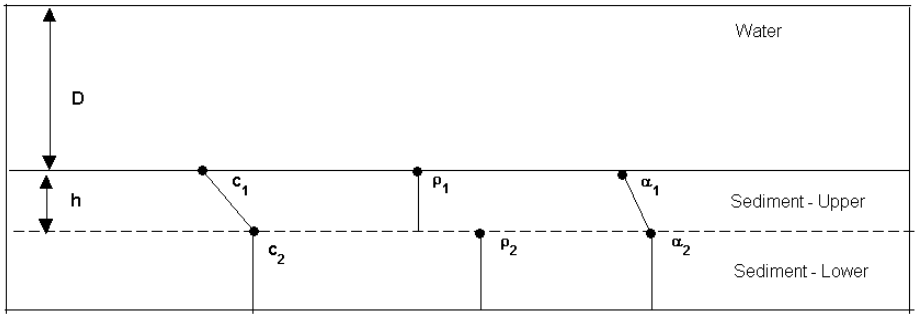

Figure 2.3: Geoacoustic model for the Barents Sea site. The upper layer represents the water column; the seabed is divided into two sediment layers. Symbols are defined in the text.

independent density ρ_1. The lower sediment layer is described by constant sound-speed and attenuation values that are identical to those at the base of the upper layer (c_2 and α_2, respectively), and by an independent density ρ_2. In addition, the model includes the water depth D. Table 2.1 summarizes geoacoustic model parameters and reference values from geophysical measurements.

Parameter and units	Geophysical data
h (m)	10-20
c_1 (m/s)	1500-1520
c_2 (m/s)	1745
ρ_1 (g/cm^3)	2.0-2.1
ρ_2 (g/cm^3)	
α_1 (dB/m kHz)	
α_2 (dB/m kHz)	
D (m)	282

Table 2.1: Geoacoustic model parameters and approximate values from supporting geophysical measurements from the Barents Sea 03 experiment.

The parameterization provides continuous profiles for sound speed and attenuation in the upper sediments where strongly discontinuous layering is not expected (not indicated by bottom-penetrating sonar), with gradients assumed in the upper layer (restricted to positive gradients for sound speed). Constant densities are assumed in the two sediment layers, since pressure-field data for the situations considered (low-frequency, long-range/low grazing-angle propagation) are expected to show little sensitivity to density gradients, and density variations with depth are effectively modelled by step changes (Rutherford and Hawker, 1978; Robins, 1991). For the relatively low sound speed shallow sediments at the experiment site, shear wave effects were assumed negligible. A prior modelling study indicated that the acoustic data analyzed in this thesis were not sensitive to properties of the underlying Triassic sediments.

Chapter 3 Theory

3.1. The inverse problem

The inverse problem can be defined as the estimation of parameters of a postulated model for a physical system from observations of some process that interacts with the system. In the context of this thesis, the physical system is the ocean, the process is acoustic propagation through the ocean, and the model parameters are geophysical (geoacoustic) properties of the seabed and the location of an (unknown) acoustic source.

In mathematical terms, the forward problem can be defined as the mapping from a specified set of model parameters **m** to the acoustic data **d** that would be observed in an acoustic experiment:

$$\mathbf{G[m]} = \mathbf{d} \tag{3.1}$$

where the operator **G** simulates the physical process leading to the data. Key properties of the forward problem are that a solution exists, is unique, and is stable (i.e., a small change in a model parameter leads to a small change in data). Conversely, the inverse problem can be expressed as a mapping from a given set of acoustic data to a model that produced the data:

$$\mathbf{G^{-1}[d]} = \mathbf{m} \tag{3.2}$$

where an operator $\mathbf{G^{-1}}$ is introduced for notational purposes, but may not be known. For the inverse problem, a solution may not exist, is generally not unique (i.e., there is often an infinite number of acceptable solutions), and is often unstable (i.e., a small change in

data can lead to a large change in model parameters). In linear inverse theory, one assumes a linear forward operator and solves for its mathematical inverse. While many systems in nature are linear, or can be linearized, ocean acoustic problems are in general strongly non-linear and a non-linear solution to the inverse problem has to be developed.

3.2. Bayesian formulation

In Bayesian inversion, information regarding the model of parameters **m** is obtained from the posterior probability density, $P(\mathbf{m}|\mathbf{d})$, according to Bayes' rule

$$P(\mathbf{m} \mid \mathbf{d})P(\mathbf{d}) = P(\mathbf{d} \mid \mathbf{m})P(\mathbf{m}). \tag{3.3}$$

Here, $P(\mathbf{m})$ is the prior model distribution, and for measured data **d**, $P(\mathbf{d})$ is a constant normalization factor. The quantity $P(\mathbf{d}|\mathbf{m})$ is (for measured data) interpreted as a function of **m**, the likelihood function. This function can generally be expressed as $L(\mathbf{m}) \propto \exp[-E(\mathbf{m})]$ for an appropriate data error (misfit) function E (considered below). Defining a generalized misfit

$$\phi(\mathbf{m}) = E(\mathbf{m}) - \log_e P(\mathbf{m}), \tag{3.4}$$

the PPD can be written

$$P(\mathbf{m} \mid \mathbf{d}) = \frac{\exp[-\phi(\mathbf{m})]}{\int \exp[-\phi(\mathbf{m}')]d\mathbf{m}'}, \tag{3.5}$$

where the integration spans the model space. The multidimensional PPD is interpreted in terms of properties defining parameter estimates, uncertainties, and interrelationships, such as the maximum *a posteriori* (MAP) estimate, the posterior mean estimate, the

model covariance matrix, parameter mean deviations (MDs), and one- and two-dimensional marginal probability distributions defined, respectively, as

$$\hat{\mathbf{m}} = \mathrm{Arg}_{\max}\{P(\mathbf{m} \mid \mathbf{d})\} = \mathrm{Arg}_{\min}\{\phi(\mathbf{m})\}, \tag{3.6}$$

$$\overline{\mathbf{m}} = \int \mathbf{m}' P(\mathbf{m}' \mid \mathbf{d})\, d\mathbf{m}', \tag{3.7}$$

$$\mathrm{C}_{\mathbf{m}} = \int (\mathrm{m}' - \overline{\mathbf{m}})(\mathrm{m}' - \overline{\mathbf{m}})^T P(\mathrm{m}' \mid \mathrm{d})\, d\mathbf{m}', \tag{3.8}$$

$$\mathrm{MD}_i = \int \left| m_i' - \overline{m}_i \right| P(\mathbf{m}' \mid \mathbf{d})\, d\mathbf{m}', \tag{3.9}$$

$$P(m_i \mid \mathbf{d}) = \int \delta(m_i - m_i') P(\mathbf{m}' \mid \mathbf{d})\, d\mathbf{m}', \tag{3.10}$$

$$P(m_i, m_j \mid \mathbf{d}) = \int \delta(m_i - m_i') \delta(m_j - m_j') P(\mathbf{m}' \mid \mathbf{d})\, d\mathbf{m}', \tag{3.11}$$

where δ is the Dirac delta function, and m_i and m_j are model parameters. Uncertainties of parameter estimates can also be quantified in terms of the highest probability density (HPD) credibility intervals. The β% HPD interval is defined as the interval of minimum width that contains β% of the marginal probability distribution. Parameter correlations are quantified by normalizing the model covariance matrix to produce the correlation matrix,

$$S_{ij} = C_{ij} \Big/ \sqrt{C_{ii} C_{jj}}\,. \tag{3.12}$$

Elements S_{ij} are within [–1,1], with a value of +1 (–1) indicating perfect correlation (anticorrelation) between m_i and m_j.

For nonlinear problems, analytic solutions to Eqs. 3.6–3.11 are generally not available, and numerical approaches must be applied. Computing the MAP estimate requires minimizing ϕ, which is typically carried out using global-search optimization schemes, such as simulated annealing or genetic algorithms (Sen and Stoffa, 1995), or hybrid optimization schemes such as adaptive simplex simulated annealing (Dosso, Wilmut, and Lapinski, 2001). For unimodal probability distributions, the posterior mean can provide parameter estimates that better represent the parameter uncertainty distribution. The integrals in Eqs. 3.7–3.11 can be solved using the Markov-chain Monte Carlo methods of Metropolis-Hastings sampling (MHS) and Gibbs (heat-bath) sampling (GS) (Dosso, 2002; Mosegaard and Sambridge, 2002; Sambridge and Mosegaard, 2002; Dosso and Wilmut, 2008).

The priors $P(\mathbf{m})$ employed here consist of uniform distributions for each of M model parameters on bounded intervals $m_i \in [m_i^-, m_i^+]$, i.e.,

$$P(\mathbf{m}) = \begin{cases} \prod_{i=1}^{M} (m_i^+ - m_i^-)^{-1} & \text{if } m_i^- \le m_i \le m_i^+, i = 1, M, \\ 0 & \text{otherwise.} \end{cases} \tag{3.13}$$

The remainder of this chapter considers only the likelihood function, with the understanding that the prior is included as per Eq. 3.4. Note that in this formulation, prior distributions are not limited to uniform; e.g., Gaussian distributions (Ó Ruanaidh and Fitzgerald, 1996), or (non-Gaussian) marginal distributions from a preceding/previous inversion (Dettmer, Dosso, and Holland, 2008) can be used as priors.

3.3. Data error function

Specifying the data uncertainty (error) distribution defines the likelihood function and is an important aspect of Bayesian inversion (Mecklenbräuker and Gerstoft, 2000; Dosso, 2002; Dosso and Wilmut, 2006). Data uncertainties, which include both measurement and theory errors, are generally not known *a priori,* and physically reasonable assumptions are required; for example, independent, Gaussian-distributed errors. These assumptions should be examined *a posteriori* by applying appropriate statistical tests to the data residuals (Chapter 3.9). This section considers defining the likelihood function for the case of a single data snapshot (time-series segment) and known data error variance. Approaches for treating multiple-snapshot data and unknown variance are developed in Chapter 5.

Consider the case of a single data snapshot, $\mathbf{d}_f$, representing complex acoustic pressure vectors at N sensors for each of f=1,F frequencies. Assuming the data errors are complex, zero-mean, Gaussian-distributed random variables uncorrelated over space and frequency with error variance v_f at the fth frequency, the likelihood function is given by

$$L(\mathbf{m}) = \prod_{f=1}^{F} \frac{1}{(\pi v_f)^N} \exp[-|\,\mathbf{d}_f - A_f e^{i\theta_f} \mathbf{d}_f(\mathbf{m})\,|^2 \,/\, v_f\,], \tag{3.14}$$

where $\mathbf{d}_f(\mathbf{m})$ represents modelled (replica) data predicted for model $\mathbf{m}$, and A_f and θ_f represent unknown source amplitude and phase. The likelihood can be maximized analytically over unknown source spectrum by setting $\partial L(\mathbf{m}) / \partial A_f = \partial L(\mathbf{m}) / \partial \theta_f = 0$ leading to

$$A_f e^{i\theta_f} = \frac{\mathbf{d}_f^\dagger(\mathbf{m})\mathbf{d}_f}{|\,\mathbf{d}_f(\mathbf{m})\,|^2}, \tag{3.15}$$

where † represents conjugate transpose. Using Eq. 3.15 in Eq. 3.14 leads to the likelihood function

$$L_1(\mathbf{m}) = \prod_{f=1}^{F} \frac{1}{(\pi\nu_f)^N} \exp[-B_f(\mathbf{m})/\nu_f], \tag{3.16}$$

and corresponding data error function

$$E_1(\mathbf{m}) = \sum_{f=1}^{F} B_f(\mathbf{m})/\nu_f. \tag{3.17}$$

In Eqs. 3.16 and 3.17, $B_f(\mathbf{m})$ represents the Bartlett mismatch, which may be written

$$B_f(\mathbf{m}) = \mathrm{Tr}\{\mathbf{C}_f\} - \frac{\mathbf{d}_f^\dagger(\mathbf{m})\mathbf{C}_f\mathbf{d}_f(\mathbf{m})}{|\,\mathbf{d}_f(\mathbf{m})\,|^2}, \tag{3.18}$$

where $\mathrm{Tr}\{\bullet\}$ represents the matrix trace, and $\mathbf{C}_f$ is the data cross-spectral density matrix at the *f*th frequency for a single data snapshot,

$$\mathbf{C}_f = \mathbf{d}_f\mathbf{d}_f^\dagger. \tag{3.19}$$

3.4. Optimization

The search for the MAP model (Eq. 3.6) is here driven by the adaptive simplex simulated annealing (ASSA) hybrid search algorithm (Dosso, Wilmut, and Lapinski, 2001), which combines the global search method of very fast simulated annealing (Ingber, 1989) with the local downhill simplex (DHS) method (Nelder and Mead, 1965). In simulated annealing (Kirkpatrick, Gelatt, and Vecchi, 1983), the probability that a

system in equilibrium at temperature T is in a state $\mathbf{m}_k$ with energy $\phi(\mathbf{m}_k)$ is given by the Gibbs-Boltzmann distribution

$$P_G(\mathbf{m}_k) = \frac{\exp[-\phi(\mathbf{m}_k)/T]}{\sum_j \exp[-\phi(\mathbf{m}_j)/T]}, \tag{3.20}$$

where the sum extends over all possible states of the system. The equilibrium behaviour of this system can be simulated by the Metropolis algorithm (MA): random perturbations are applied to model parameters, with the resulting model conditionally accepted based on the Metropolis criterion, i.e., if a random number ξ drawn from a uniform distribution on [0,1] satisfies

$$\xi \le e^{-\Delta\phi/T}, \tag{3.21}$$

where $\Delta\phi$ is the energy difference from the original model. The DHS method operates on a simplex of models and repeatedly applies the geometric operations of reflection, expansion, and contraction to the highest-energy model of the simplex. In ASSA, DHS operations are followed by a random perturbation of model parameters, with acceptance based on MA. After a required number of accepted perturbations, the temperature is reduced according to $T_{k+1} = \beta T_k$ with β<1 to decrease the probability of accepting a higher-energy model. This procedure is repeated until convergence, defined to be when the difference between the highest and lowest energies in the simplex (relative to their average) is less than a pre-defined threshold. The ASSA algorithm employs several techniques for increased efficiency, including adaptive adjustment of the perturbation size for each parameter and drawing the parameter perturbations from Cauchy distributions, i.e.,

$$\delta m_i = k_i \tan(\eta_i \pi) \tag{3.22}$$

with k_i the perturbation widths, and η_i a uniform random variable on [–½,½]. (For example, k_i can be set to 3 times the mean absolute value of the 30 last accepted perturbations.) Note that the Cauchy distribution has heavier tails than a Gaussian distribution, and thus allows for wider sampling.

3.5. Metropolis-Hastings sampling

The integral properties of the PPD (Eqs. 3.7–3.11) requires evaluation of integrals of the general form

$$I = \int f(\mathbf{m}) P(\mathbf{m} \mid \mathbf{d}) \, d\mathbf{m}. \tag{3.23}$$

These integrals can be evaluated numerically by the Monte Carlo method of importance sampling. Let $g(\mathbf{m})$ define a (normalized) sampling distribution from which Q models are drawn. Equation 3.23 can be written

$$I = \int \left[\frac{f(\mathbf{m}) P(\mathbf{m} \mid \mathbf{d})}{g(\mathbf{m})} \right] g(\mathbf{m}) \, d\mathbf{m} \approx \frac{1}{Q} \sum_{k=1}^{Q} \frac{f(\mathbf{m}_k) P(\mathbf{m}_k \mid \mathbf{d})}{g(\mathbf{m}_k)}. \tag{3.24}$$

In Metropolis-Hastings sampling, the PPD is used as the sampling function, i.e., $g(\mathbf{m})=P(\mathbf{m}|\mathbf{d})$. Thus

$$I \approx \frac{1}{Q} \sum_{k=1}^{Q} f(\mathbf{m}_k), \tag{3.25}$$

i.e., the integral can be estimated as the average of $f(\mathbf{m})$ over the Q models drawn from the PPD. Comparing the PPD (Eq. 3.5) with the Gibbs-Boltzmann distribution (Eq. 3.20)

shows that these expressions are identical at temperature T=1. Thus samples can be drawn by the MA at T=1 as described above.

To decrease the number of required samples and thus reduce the computational effort, several techniques are employed (Dosso, 2002; Dosso and Wilmut, 2008). This includes initiating MHS from a reasonably good starting model such as the MAP model, and drawing samples from a proposal distribution (described below). Convergence of sampling is monitored by comparing estimates for marginal distributions from two independent samples collected in parallel. A difference between the cumulative marginal distributions for all parameters of less than 0.10 is typically required for convergence. The moments of the PPD (Eqs. 3.7–3.11) are then computed from the union of the two samples after convergence.

3.6. Proposal distributions

In MHS, parameter perturbations can be drawn from any distribution, known as the proposal distribution. The choice of proposal distribution does not affect the integral estimates, but can improve sampling efficiency (Gilks, Richardson, and Spiegelhalter, 1996). Typical proposal distributions used in geoacoustic inversion have been uniform distributions applied in rotated coordinates (Dosso, 2002; Battle et al., 2004).

Sampling in rotated coordinates is advantageous because parameter correlations can cause oblique regions of low misfit which are not aligned with the parameter axes; such regions are inefficiently sampled with perturbations along the axes. The transformation between physical parameters $\mathbf{m}$ and rotated parameters $\mathbf{m}'$ is given by

$$\mathbf{m}' = \mathbf{U}^T\mathbf{m}, \qquad \mathbf{m} = \mathbf{U}\mathbf{m}', \tag{3.26}$$

where T here denotes transpose, $\mathbf{U}$ is the eigenvector matrix of the model covariance matrix,

$$\mathbf{C_m} = \mathbf{U}\mathbf{W}\mathbf{U}^T, \tag{3.27}$$

and $\mathbf{W}=\mathrm{diag}\{w_1,...,w_M\}$ is the eigenvalue matrix. The eigenvalues w_i represent the parameter variance projected along eigenvector $\mathbf{u}_i$. After the rotation matrix has been obtained, parameters are perturbed individually in rotated coordinates, then rotated back to physical coordinates for evaluation of misfit. To increase numerical stability, rotations and perturbations are applied to nondimensionalized parameters scaled to vary over the interval [0,1]. Rotation matrices can be obtained by applying unrotated sampling during an initial *burn-in* phase to estimate $\mathbf{C_m}$ (via Eq. 3.8), then update this estimate as further samples are collected in rotated coordinates (Dosso, 2002). The samples collected in the burn-in phase are not used for the final PPD estimate. Convergence of the burn-in phase is monitored by comparing the correlation matrices for two independent samples collected in parallel; a maximum difference (of matrix elements) of 0.3 is here required to get a reasonably good estimate of $\mathbf{C_m}$.

The distribution widths of the parameter perturbations can be adaptively adjusted; a typical scheme (Dosso, 2002), adopted in Chapters 4–6, is to set the perturbation widths k_i equal to a constant factor times the maximum accepted perturbation (e.g., k_i=2 during burn-in and initial collection of samples in rotated coordinates, reduced to k_i=1.2 after a suitably large number of collected samples).

Further efficiency is obtained by drawing parameter perturbations from scaled Cauchy distributions (Eq. 3.22), with k_i taken to be the rotated parameter standard deviations $\sqrt{w_i}$ (Eq. 3.27) (Dosso and Wilmut, 2008); this approach is adopted in Chapter 8.

For a more efficient approach to estimation of $\mathbf{C_m}$ (Dosso and Wilmut, 2008), one can start with the model covariance matrix for a local linear approximation to the PPD in the vicinity of a reference model. From linear inverse theory, the model covariance matrix for the linearized solution is given by

$$\mathbf{C_m} = \left[\mathbf{J}^T \mathbf{C_D^{-1}} \mathbf{J} + \mathbf{C_{m0}^{-1}}\right]^{-1}, \tag{3.28}$$

where $\mathbf{C_D}$ is the data covariance matrix, $\mathbf{C_{m0}}$ the prior model covariance matrix of an assumed Gaussian distribution around the reference model $\mathbf{m}_0$, and $\mathbf{J}$ is the Jacobian matrix of partial derivatives with elements

$$J_{ji} = \frac{\partial d_j(\mathbf{m}_0)}{\partial m_i}, \tag{3.29}$$

with d_j the modelled data (at sensor j) evaluated at $\mathbf{m}_0$. More specifically, $\mathbf{m}_0$ is taken to be the MAP model $\hat{\mathbf{m}}$, $\mathbf{C_D}$ is a diagonal matrix with representative data error variances (considered below), and $\mathbf{C}_{m0}$ a diagonal matrix with variances equal to those of the uniform prior distribution, i.e., $(m_i^+ - m_i^-)^2/12$. This starting estimate for $\mathbf{C_m}$ is updated as further samples are collected in rotated coordinates.

3.7. Data error variance estimation

This thesis assumes that data errors are uncorrelated spatially and over frequency (i.e., data covariance matrix given by $\mathbf{C_D} = v_f \mathbf{I}$ with v_f the variance at frequency f and $\mathbf{I}$ the

$N \times N$ identity matrix). Explicit variance estimates can be obtained from (Gerstoft and Mecklenbräuker, 1998; Dosso and Wilmut, 2006):

$$\hat{v}_f = B_f(\hat{\mathbf{m}})/N, \tag{3.30}$$

with B_f the Bartlett mismatch (Eq. 3.18) and $\hat{\mathbf{m}}$ the maximum-likelihood (ML) model estimate obtained by minimizing the misfit function

$$E_2(\mathbf{m}) = N\sum_{f=1}^{F} \log_e B_f(\mathbf{m}) \tag{3.31}$$

using numerical optimization. The variance estimate (Eq. 3.30) is obtained by maximizing the likelihood L_1 (Eq. 3.16) over unknown variance by setting $\partial L_1(\mathbf{m})/\partial v_f = 0$. The misfit function $E_2(\mathbf{m})$ is obtained by substituting the estimate $\hat{v}_f$ back into the likelihood.

3.8. Gibbs and high-temperature sampling

For application to source localization, discrete sampling over range and depth coordinates (ambiguity surfaces) is required. These surfaces can contain regions of isolated local minima, and MHS has proved inefficient (Dosso and Wilmut, 2007, 2008). In Gibbs sampling, one forms for each parameter m_i the *conditional* probability distribution $P(m_i \mid \mathbf{d}) \propto \exp[-\phi(m_i)/T]$, with all other parameters fixed. A new value m_i' is drawn at random from this distribution and accepted unconditionally. To do so, one forms the (normalized) *cumulative* distribution

$$C(m_i) = \int_{m_i^-}^{m_i} \exp[-\phi(\zeta)/T]\, d\zeta, \tag{3.32}$$

draws a random number ξ from a uniform distribution on [0,1], and selects the value m_i' for which $C(m_i')$ is equal to ξ. Note that for range-independent problems, ambiguity surfaces and thus conditional distributions can be computed efficiently using normal-mode propagation models (Dosso and Wilmut, 2007, 2008).

For some problems, in particular tracking problems with prior track constraints, it can be required to sample at non-unity temperatures T>1 in order to more widely wander the parameter space (Brooks and Frazer, 2005; Dosso and Wilmut, 2008). The results must then be corrected back to T=1. Following Dosso and Wilmut (2008), first rewrite the integral of Eq. 3.23 as

$$I = \frac{Z_T}{Z_1} \int f(\mathbf{m}) \exp\left[-\phi(\mathbf{m})(1-1/T)\right] \frac{\exp\left(-\phi(\mathbf{m})/T\right)}{Z_T}\, d\mathbf{m}, \tag{3.33}$$

where

$$Z_1 = \int \exp\left[-\phi(\mathbf{m})\right] d\mathbf{m} \tag{3.34}$$

and

$$Z_T = \int \exp\left[-\phi(\mathbf{m})/T\right] d\mathbf{m} \tag{3.35}$$

are the partition functions for sampling at T=1 and non-unity temperature T, respectively. Drawing a sample of Q models $\{\mathbf{m}_k,\ k = 1, Q\}$ from $\exp[-\phi(\mathbf{m})/T]/Z_T$ using GS or MHS at temperature T, the integral I can be approximated by

$$I \approx \frac{Z_T}{Z_1} \frac{1}{Q} \sum_{k=1}^{Q} f(\mathbf{m}_k) \exp\left[-\phi(\mathbf{m}_k)(1-1/T)\right], \tag{3.36}$$

which can be rearranged to

$$I \approx \frac{1}{\sum_{k=1}^{Q} \exp[-\phi(\mathbf{m}_k)(1-1/T)]} \sum_{k=1}^{Q} f(\mathbf{m}_k) \exp\left[-\phi(\mathbf{m}_k)(1-1/T)\right]. \tag{3.37}$$

Thus the integral can be estimated from GS or MHS at non-unity temperature by weighting each model $\mathbf{m}_k$ by a factor that depends on its misfit ϕ and temperature T, with appropriate normalization. GS and MHS at non-unity temperature is employed in Chapter 8.

3.9. Posterior statistical tests

The data error functions used in this thesis (e.g., Eq. 3.17) are based on the assumptions of uncorrelated, zero-mean, complex Gaussian-distributed random errors. If these assumptions are not valid, the inversion results, in particular uncertainty estimates, may not be reliable. Hence, the assumptions on error statistics should be checked *a posteriori* (Dosso, Nielsen, and Wilmut, 2006).

The assumptions can be checked by considering the standardized data residuals,

$$\mathbf{r}_f(\hat{\mathbf{m}}) = \left(\mathbf{d}_f - A_f e^{i\theta_f} \mathbf{d}_f(\hat{\mathbf{m}})\right) \Big/ \hat{v}_f^{1/2} \tag{3.38}$$

where $\hat{\mathbf{m}}$ is the ML model, $\hat{v}_f$ the variance estimate (Eq. 3.30), and A_f and $e^{i\theta_f}$ the source amplitude and phase ML-estimates (Eq. 3.15). The assumption of Gaussian-distributed errors can be considered qualitatively by comparison of (normalized) histograms of the residuals to the standard normal distribution. One can also apply quantitative statistical tests such as the Kolmogorov-Smirnov (KS) test to provide a *p*-value indicating the level of evidence against the null hypothesis H_0 of Gaussian-distributed errors. A value of $p \geq 0.05$ is considered to provide no significant evidence against H_0, while $p < 0.05$

provides significant evidence against H_0. The runs (median-delta) test (e.g., Walpole et al., 2007) can be applied to quantify the level of evidence against the null hypothesis of uncorrelated errors. The test considers the number of runs of residuals of either side of their median value. The test is applied to both the real and the imaginary parts of the residuals separately, to establish that these are spatially uncorrelated from sensor to sensor. The runs test can also be considered for correlations at each sensor, between frequencies, and data snapshots, respectively, if appropriate. If either of the tests are failed, i.e., the hypotheses significantly violated, it may be necessary to estimate and include the full data covariance matrix in the inversion analysis (Dosso, Nielsen, and Wilmut, 2006; Huang, Gerstoft, and Hodgkiss, 2006; Jiang, Chapman, and Badiey, 2007; Dettmer, Dosso, and Holland, 2008).

Chapter 4 Simulation study: geoacoustic information content of HLA data

4.1. Introduction

This chapter examines the effectiveness of horizontal line arrays for matched-field inversion by quantifying geoacoustic information content for a variety of experiment and array factors, including array length and number of sensors, and source range and bearing. The effects of source frequency content and SNR are also considered, and HLA and VLA performances are compared. Geoacoustic information content is quantified in terms of marginal PPDs for model parameters computed via numerical integration within a Bayesian inversion framework. This produces a quantitative estimate of the geoacoustic parameter uncertainties which can be directly compared for various experiment/array factors. A similar approach has been applied to study VLA inversion characteristics by Dosso and Wilmut (2002). The approach is general, and it is beyond the scope of this chapter to provide an exhaustive analysis of all possible cases of interest. The emphasis is on bottom-moored HLAs and controlled-source data, which is considered to define the canonical test case. The features of this case are examined in detail, and comparisons are made to inversion using ship-noise sources, a towed HLA, and a VLA. The work in this chapter has been published as Tollefsen and Dosso (2007).

4.2. Theory

Bayesian inversion is described in Chapter 3. The study in this chapter uses the standard assumptions of uncorrelated complex-Gaussian distributed data errors with variance ν_f at the *f*th frequency and unknown source amplitude and phase. The data error function is given by Eq. 3.17, with the Bartlett mismatch given by Eq. 3.18.

To simulate noisy data in MFI, the CSDM can be computed using synthetic acoustic fields for the true model and the error variance added to the main diagonal of $\mathbf{C}_f$, i.e.,

$$\mathbf{C}_f = \mathbf{d}_f \mathbf{d}_f^\dagger + \nu_f \mathbf{I}, \tag{4.1}$$

where $\mathbf{d}_f$ is the error-free data vector and $\mathbf{I}$ is the identity matrix (Huang, Gerstoft, and Hodgkiss, 2006). Under the assumption of independent Gaussian errors, data error variances that are representative of experimental data can be computed as

$$v_f = \left|\mathbf{d}_f\right|^2 10^{-\mathrm{ESNR}_f/10} / N, \tag{4.2}$$

where N is the number of array elements and ESNR is the equivalent signal-to-noise ratio which takes into account all sources of uncertainty (measurement and theory error). ESNR estimates can be computed according to (Dosso and Nielsen, 2002)

$$\mathrm{ESNR}_f = 10\log_{10}\frac{\mathrm{Tr}\{\mathbf{C}_f\} - B_f(\hat{\mathbf{m}})}{B_f(\hat{\mathbf{m}})}, \tag{4.3}$$

where $B_f(\hat{\mathbf{m}})$ is the Bartlett mismatch (Eq. 3.18) for the maximum-likelihood geoacoustic model estimate $\hat{\mathbf{m}}$. ML-model mismatch values reported in the literature (Dosso and Nielsen, 2002; Huang, Gerstoft, and Hodgkiss, 2006) translate to ESNR values within 0–8 dB, and typically decrease with increasing frequency.

For MFI as applied in this chapter, the spatial sampling capability of an HLA can be

discussed in terms of its effective vertical aperture (Bogart and Yang, 1994), approximated by the expression

$$L_{eff} = L \tan \varphi \tag{4.4}$$

where L is the longitudinal aperture of the array, and φ the grazing angle of the highest-order mode of the measured acoustic field (Barlee, Chapman, and Wilmut, 2005). The effective vertical aperture is largest for a source endfire to the array, and diminishes as the source is moved to array broadside.

4.3. Examples

4.3.1. Canonical environment and array

An environmental model representative of the shallow continental shelf was chosen for this study. The environment (Fig. 4.1) consists of a 115-m water column over a seabed with a 12-m thick sediment layer over a semi-infinite basement. A downward refracting SSP in water is assumed, with sound speed decreasing from 1472 m/s at the surface to 1468 m/s at the seabed. Sound speed in the sediment increases from 1503 m/s at the seabed to 1560 m/s at 12 m depth (an increase equivalent to $h^{0.015}$, for sediment thickness h, typical of sandy sediments (Hamilton, 1980)). The sound speed in the basement is 1750 m/s, representative of consolidated material; this provides a hard reflecting interface at the sediment-basement boundary. The true values and *a priori* search bounds for the eight seabed geoacoustic parameters and water depth are given in Table 4.1. In addition,

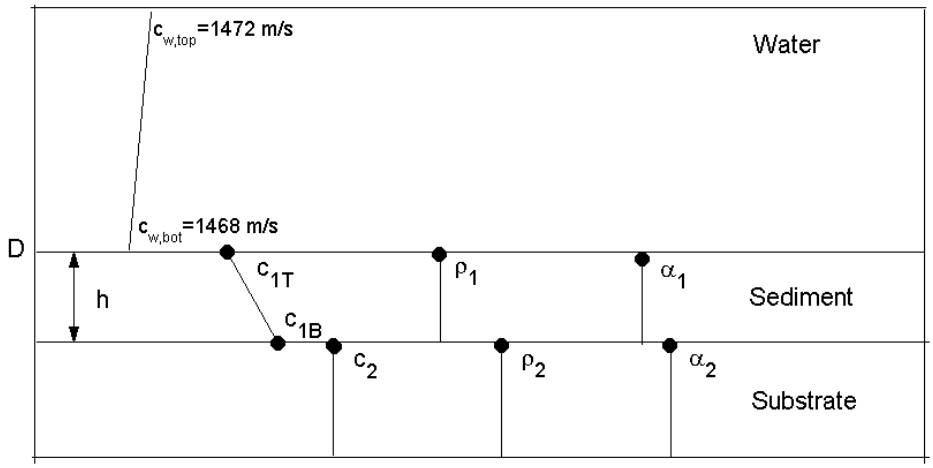

Figure 4.1: Geoacoustic model for simulation study (continental shelf environment). See Table 4.1 for parameters and definitions.

Parameter Name	Symbol	Unit	Lower Bound	Upper Bound	True Value
Sediment thickness	h	m	0	40	12
Sediment p-velocity surface	c_{1T}	m/s	1450	1600	1503
Sediment p-velocity bottom	c_{1B}	m/s	1500	1650	1560
Substrate p-velocity	c_2	m/s	1600	1900	1750
Sediment density	ρ_1	g/cm³	1.20	2.00	1.50
Substrate density	ρ_2	g/cm³	1.40	2.20	1.85
Sediment p-wave attenuation	α_1	dB/λ	0.01	1.00	0.22
Substrate p-wave attenuation	α_2	dB/λ	0.01	1.00	0.12
Water depth	D	m	113	117	115

Table 4.1: Geoacoustic model parameters, prior search bounds, and true values for simulation study.

source range and depth and (in some cases) bearing are included as geometric search parameters with small search bounds around their true values.

A variety of source and array configurations are considered in a series of examples in the following sections. These cases are compared to the baseline or canonical case which involves a 256-m HLA with 33 sensors on the seafloor spaced at 8-m intervals. The

acoustic source is at 25-m depth and 3.23-km range from the closest array element in the array endfire direction. The canonical case considers data at 7 frequencies at 50-Hz intervals over the band 200–500 Hz. ESNR values were set to 6 dB at 200 Hz decreasing linearly to 4.5 dB at 500 Hz. The canonical case is considered representative of a typical controlled experiment with a high-level source operated in the vicinity of a bottom-moored HLA.

The normal-mode numerical propagation model ORCA (Westwood, Tindle, and Chapman, 1996) was used to compute synthetic data and replica pressure fields. The model was executed using a fast real-axis mode search with a perturbation approach to approximate modal attenuations and ignoring near-field effects. For cases involving short-range propagation (to towed arrays), the model applied a complex-plane mode search to incorporate near-field effects. Propagation from sources off endfire direction was accommodated by computing individual source-array element ranges using the law of cosines.

4.3.2. Source frequency

The effect of source frequency content is examined first for the canonical HLA by considering three cases involving frequency bands of 200–800 Hz and 200–500 Hz with 100-Hz spacing, and 200–500 Hz with 50-Hz spacing. Figure 4.2 shows (one-dimensional) marginal PPDs computed for these three data sets for the eight geoacoustic parameters, water depth, and two geometric parameters, as well as for an additional geoacoustic parameter representing the average sound speed in sediment layer defined by

$$c_{\mathrm{AVE}} = \frac{1}{h}\int_0^h c(z)dz = 2c_{1T}c_{1B}/(c_{1T}+c_{1B}), \tag{4.5}$$

where $c(z)$ represents a $1/c^2$-linear function varying from c_{1T} at the top of the sediment layer (thickness h) to c_{1B} at the bottom, as assumed by ORCA. Marginal PPDs for c_{AVE} are readily computed from the collected model samples, and provide a useful additional measure of information (e.g., in some problems, c_{AVE} can be better determined than c_{1T} and c_{1B} indicating that the average sound speed is more important acoustically than the sound-speed gradient).

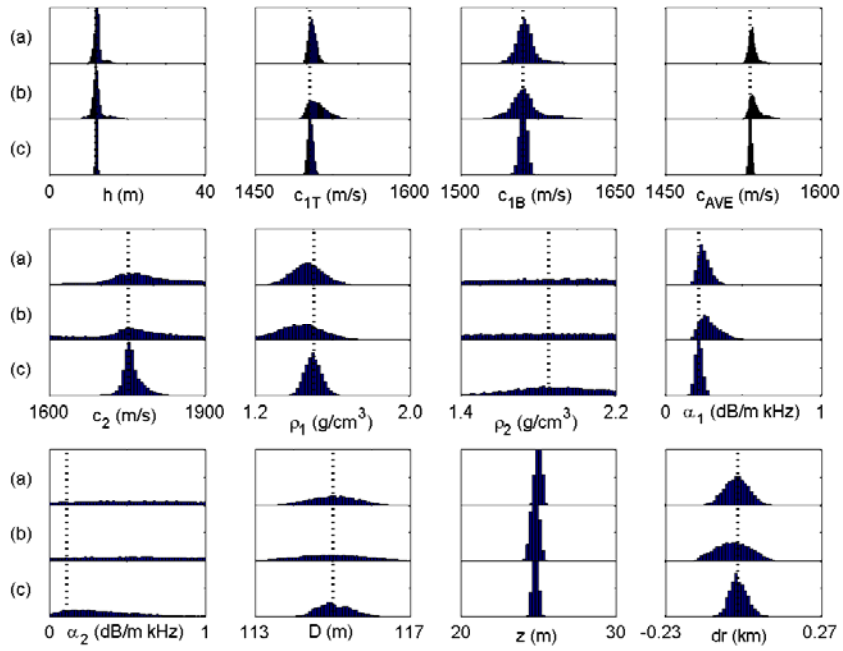

Figure 4.2: Effect of source frequency content. Marginal PPDs for canonical case and data consisting of: (a) 200–800 Hz band with 100-Hz spacing, (b) 200–500 Hz band with 100-Hz spacing, and (c) 200–500 Hz band with 50-Hz spacing. Dotted lines indicate true parameter values.

The most sensitive geoacoustic parameters for all cases are those defining the sediment sound-speed profile (h, c_{1T}, c_{1B}), with c_{1T} better resolved than c_{1B}, and the basement

sound speed (c_2) even less well resolved. The average sound speed is better resolved than c_{1B}, and c_{AVE} provides a useful additional indicator of geoacoustic information content. There is some sensitivity to sediment density (ρ_1) and attenuation (α_1), while basement density and attenuation (ρ_2 and α_2) are unresolved. The source depth (z) is well resolved within its search bounds, while source range (r) and water depth (D) are reasonably well resolved.

Figure 4.2 indicates that the 200–500 Hz frequency band and 50-Hz spacing provides the highest geoacoustic information content, i.e., the narrowest marginal uncertainty distributions for the geoacoustic and geometric parameters. For the less informative cases, the distributions are wider and for some parameters have a peak offset from the true parameter value; both are manifestations of loss of information content. Further examples (results not shown) indicated that including more frequencies (200–500 Hz at 25-Hz spacing) did not yield an appreciable improvement over the best case shown in Fig. 4.2. Unless otherwise noted, the following examples employ the 200–500 Hz band with 50-Hz spacing.

4.3.3. Array length and number of sensors

The array configuration parameters of length, number of sensors, and sensor spacing are inter-related; the study is here limited to equidistant sensor spacing with one of the two remaining parameters held fixed. Array length is considered first, with sensor spacing held fixed at 8 m. Figures 4.3 and 4.4 show marginal PPDs and 95% HPD

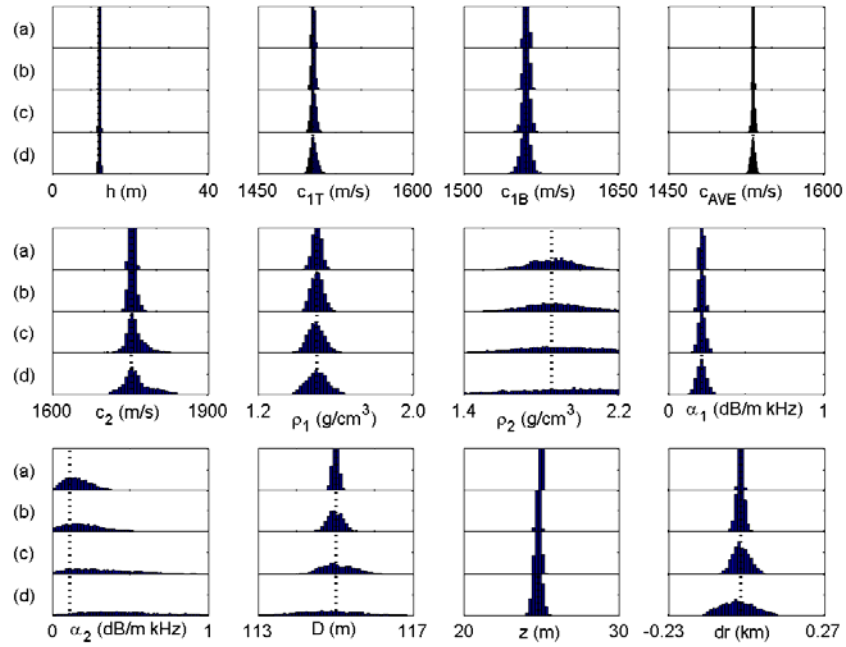

Figure 4.3: Effect of array length (8-m sensor spacing). Marginal PPDs for: (a) 1024-m array with 129 sensors, (b) 512-m array with 65 sensors, (c) 256-m array with 33 sensors, and (d) 128-m array with 17 sensors.

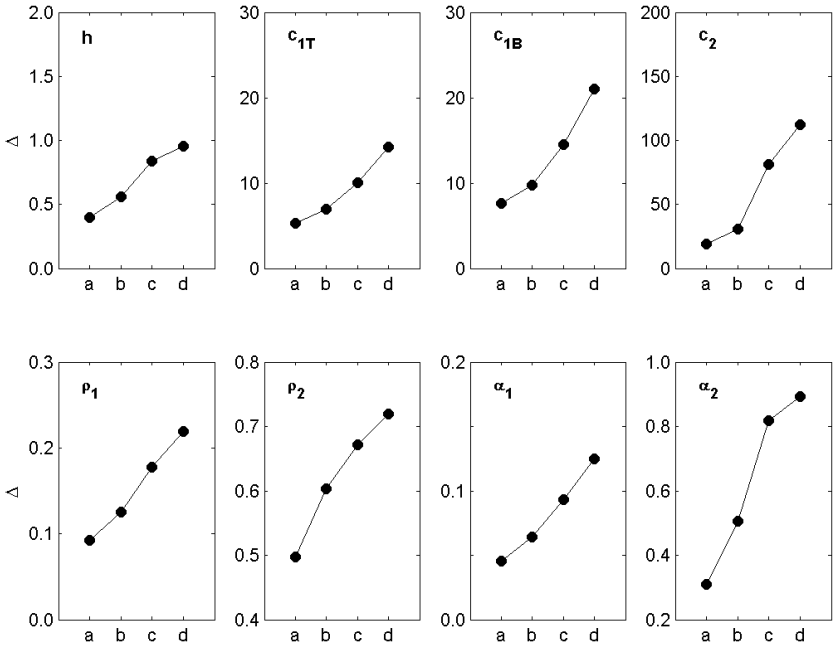

Figure 4.4: 95% HPD credibility intervals for cases described in Fig. 4.3.

credibility intervals for four arrays with length/number of sensors of: 1024 m/129 sensors, 512 m/65 sensors, 256 m/33 sensors (the canonical case), and 128 m/17 sensors. Figures 4.3 and 4.4 show that geoacoustic information content decreases monotonically with array length. This decrease in resolution is, of course, expected; however, the Bayesian analysis quantifies the effect. For example, 95% credibility intervals for c_{1T} and c_2 are 5 m/s and 20 m/s respectively for the longest array, increasing to 15 m/s and 115 m/s for the shortest array. Similar substantial decreases in resolution are observed for other parameters, with credibility intervals more than doubling as array length is reduced by a factor of four from 1024 m to 256 m (except for ρ_2 which is limited by the prior search bounds). It is interesting to note that for a sufficiently long array, even the relatively insensitive parameters of basement attenuation and (to some extent) basement density are resolved.

Short HLAs can be desirable for practical reasons, and further examples are considered here to investigate lower limits of useful array length in geoacoustic inversion. Figure 4.5 shows marginal PPDs for a fixed sensor spacing reduced to 4 m and array length/number of sensors of: 128 m/33 sensors, 64 m/17 sensors, and 32 m/9 sensors. The results for the 128-m array are reasonably good for the sediment parameters and basement sound speed, and represent a significant improvement over the results for the 128-m array with 8 m spacing in Fig. 4.3. The 64-m array resolves the sediment sound speeds reasonably well, but c_2 and ρ_1 are notably degraded. The 32-m array produces generally poor results (however, including more frequencies in the inversion or use of sources with different frequency content could yield useful results for the 32-m array; this has not been further investigated here).

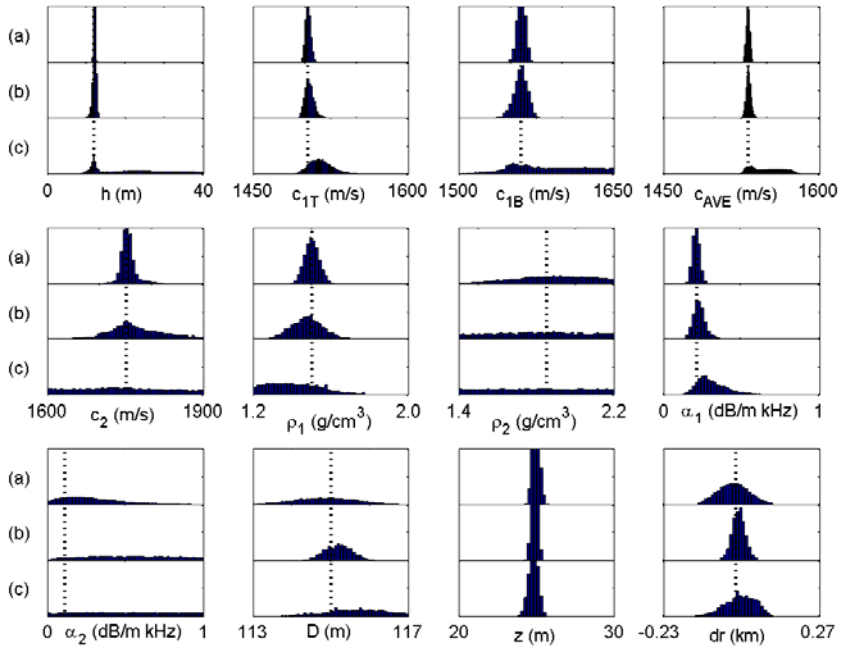

Figure 4.5: Effect of array length (4-m sensor spacing). Marginal PPDs for: (a) 128-m array with 33 sensors, (b) 64-m array with 17 sensors, and (c) 32-m array with 9 sensors.

To consider the effect of the number of sensors and inter-sensor spacing with constant HLA length, Figs. 4.6 and 4.7 show marginal PPDs and credibility intervals computed for the 256-m long array when the number of sensors is varied from 65 at 4-m spacing to 9 at 32-m spacing. The inter-sensor spacing (number of sensors) has a substantial effect on information content; e.g., 95% credibility intervals for c_{1T} and c_2 are 7 m/s and 25 m/s respectively for the densest array, increasing to 20 m/s and 170 m/s for the sparsest array. The 95% credibility intervals increase with inter-sensor spacing for all parameters except ρ_2 and α_2. However, the minor reversal of the trend observed for these insensitive basement parameters is not significant as the intervals are near their upper limit of 95% of the prior search bounds.

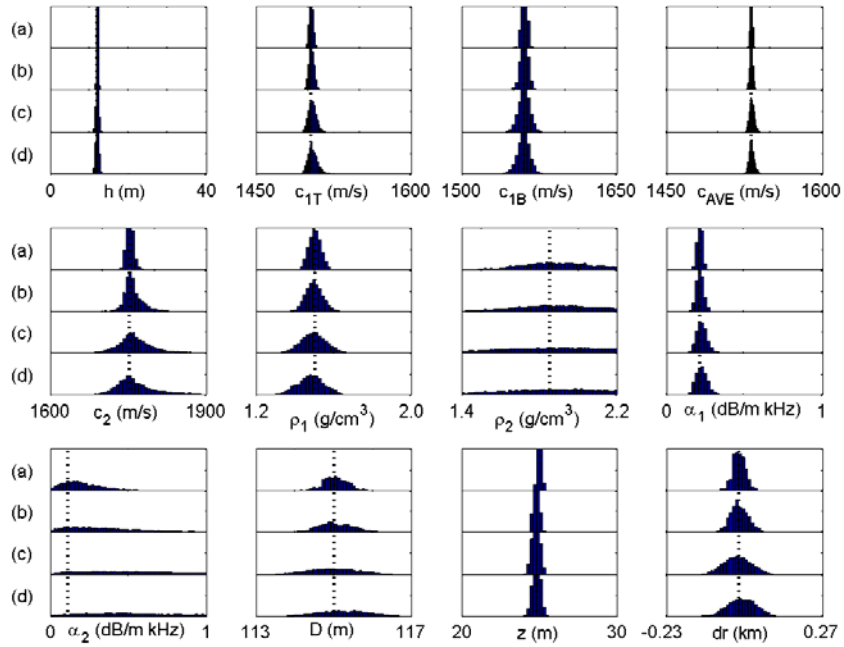

Figure 4.6: Effect of number of sensors (array length 256 m). Marginal PPDs for: (a) 65 sensors at 4-m spacing, (b) 33 sensors at 8-m spacing, (c) 17 sensors at 16-m spacing, and (d) 9 sensors at 32-m spacing.

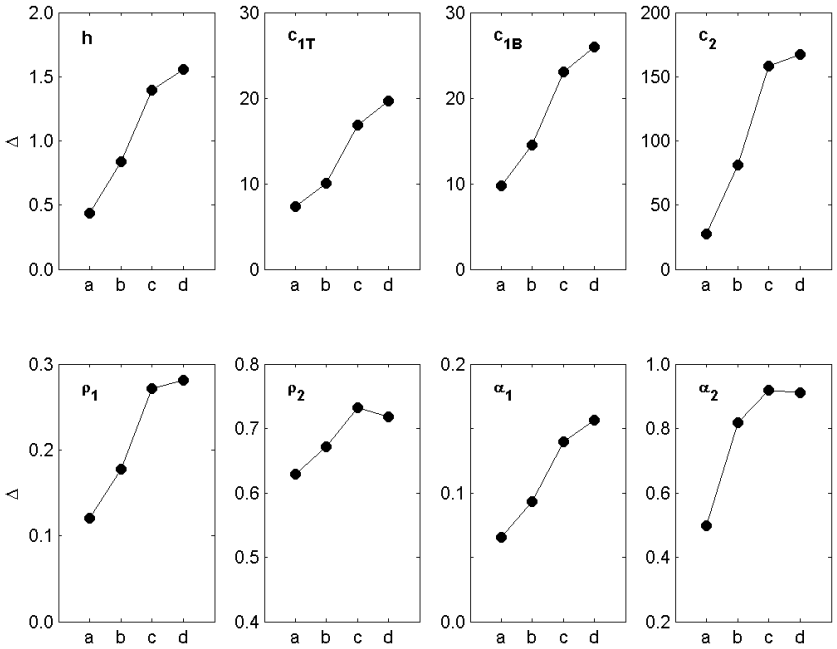

Figure 4.7: 95% HPD credibility intervals for cases described in Fig. 4.6.

4.3.4. Source range

The effect of source-array range on geoacoustic inversion was addressed in Dosso and Wilmut (2002) for the case of noisy synthetic VLA data in an environment similar to that used here. It was observed that the uncertainty of all parameters, in particular those representing deeper seabed structure, increased with source-array range. The only exception was sediment density, ρ_1, for which uncertainty decreased with range. This was attributed to the attenuation with range of the higher-order modes, which penetrate more deeply into the seabed, with a consequent loss of information on deeper structure. Similar observations were made for inversions of measured HLA data in Knobles et al. (2003), and Koch and Knobles (2005). It can also be argued that attenuation of higher-order modes with range can degrade results for parameters of the upper part of sediment, since the relatively short vertical wavelength of these modes provides information for small penetration depths. It is also worth noting that as the higher-order modes attenuate with range, the modes sampled at the array correspond to shallower propagation angles, which, from Eq. 4.4, requires a longer HLA to retain the effective vertical aperture.

Figures 4.8 and 4.9 show marginal PPDs and 95% credibility intervals computed for the canonical array and for sources at ranges of 1.23 km, 3.23 km (the canonical case), 6.23 km, and 10.23 km. These figures illustrate a general loss of resolution with increasing range for all parameters except ρ_1 and α_1. In some cases the degradation with range is profound; e.g., in going from 1.23 to 10.23 km range, credibility intervals increase from 0.5 to 24 m for h, 15 to 112 m/s for c_{1B}, and 23 to 283 m/s for c_2. In contrast, for ρ_1, the resolution improves significantly with range (credibility interval decreases from 0.26 to 0.15 g/cm^3), while the resolution is largely unaffected for α_1.

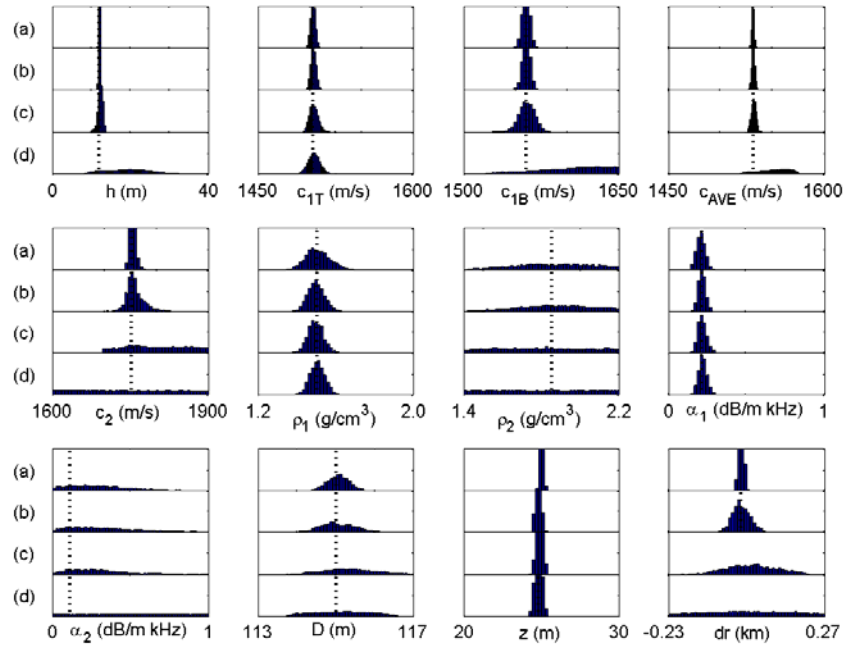

Figure 4.8: Effect of source range. Marginal PPDs for source-array ranges of: (a) 1.23 km, (b) 3.23 km, (c) 6.23 km, and (d) 10.23 km.

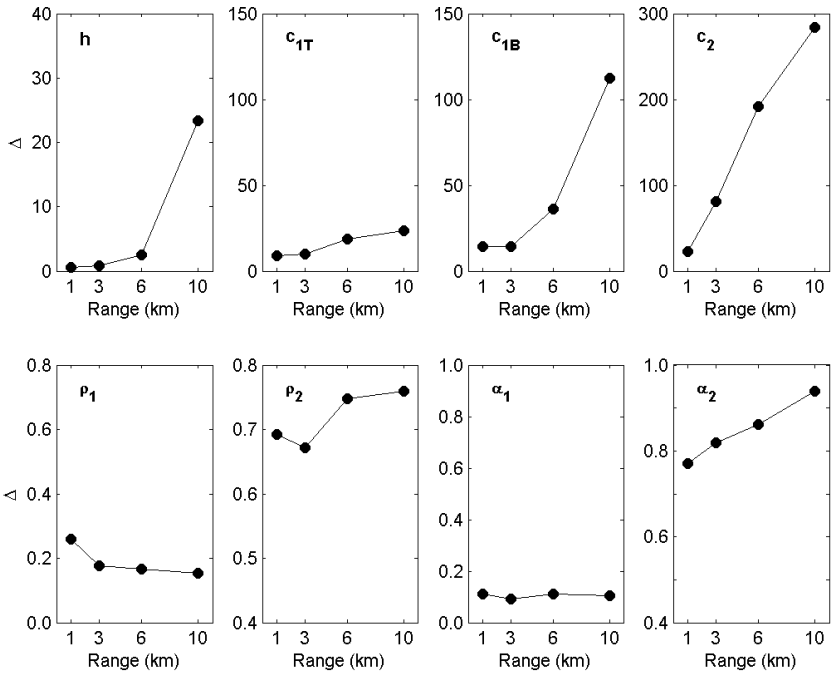

Figure 4.9: 95% HPD credibility intervals for cases described in Fig. 4.8.

4.3.5. Source bearing

The previous examples all considered sources located at endfire relative to the HLA. However, it could often be of interest to process data from other bearings; this section investigates the effect on geoacoustic information content of source bearing. One might intuitively anticipate a loss of geoacoustic resolution as a source moves away from endfire since, according to Eq. 4.4, the longitudinal aperture and thus effective vertical aperture of the array diminishes. However, this may in part be balanced by the fact that the effective inter-sensor spacing is reduced, and the combined effect is not necessarily obvious. Two cases are considered here consisting of the 256-m canonical array and a 1024-m array, both with 33 elements. In these simulations, source bearing was included as an unknown parameter, with a prior search interval of ±3° about the true bearing. The reference point for range and bearing for these cases is the mid-point of the array.

Results for the canonical array for sources at a series of angles from endfire to broadside are shown in Figs. 4.10 and 4.11. There is relatively little effect on geoacoustic resolution as the source is moved from endfire to 75°; e.g., credibility intervals for c_{1T} increases from 8.3 m/s to 10.5 m/s only. However, when the source is moved to broadside the geoacoustic information content decreases dramatically, with essentially flat marginal PPDs for all geoacoustic parameters in Fig. 4.10.

Figures 4.12 and 4.13 show inversion results for the 1024-m array, which is relatively sparsely populated with 33 sensors spaced at 32 m. Fig. 4.13 shows that the credibility intervals decrease (geoacoustic information content increases) for several parameters as the source is moved from endfire to 75° bearing. This may be attributed to the effect of

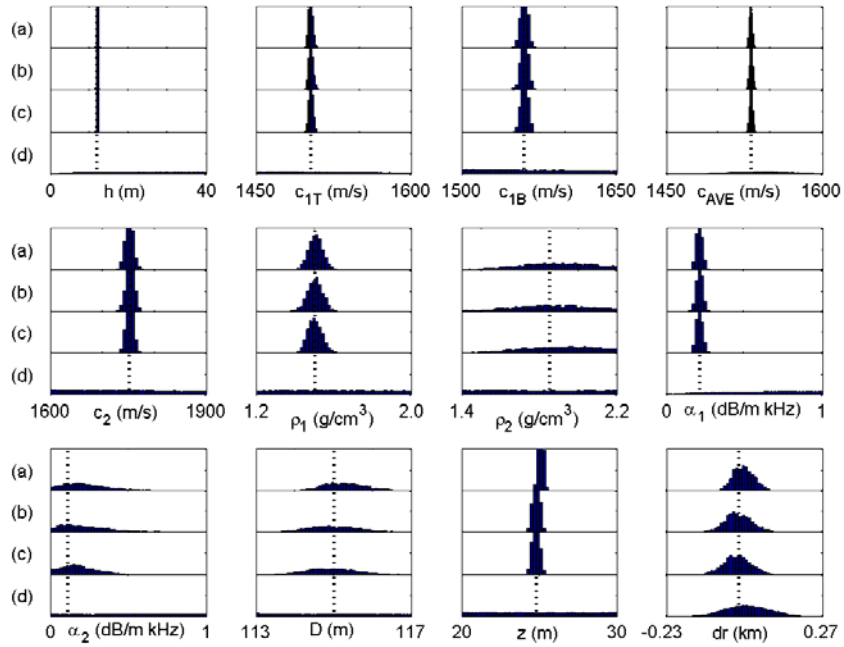

Figure 4.10: Effect of source azimuth (canonical array). Marginal PPDs for sources at bearings of: (a) 0°, (b) 30°, (c) 60°, and (d) 90°. Array is 256 m long with 33 sensors.

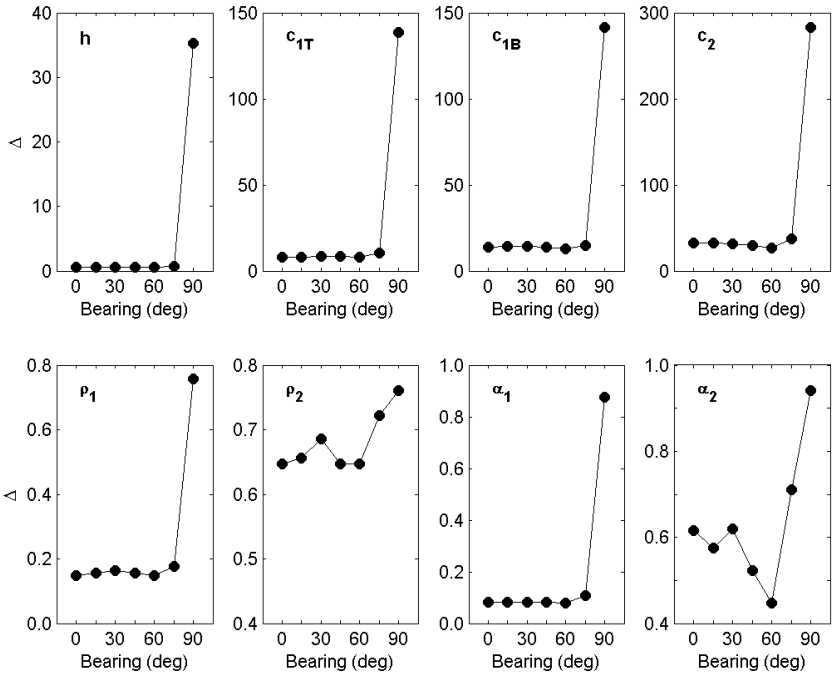

Figure 4.11: 95% HPD credibility intervals versus source bearing for canonical array.

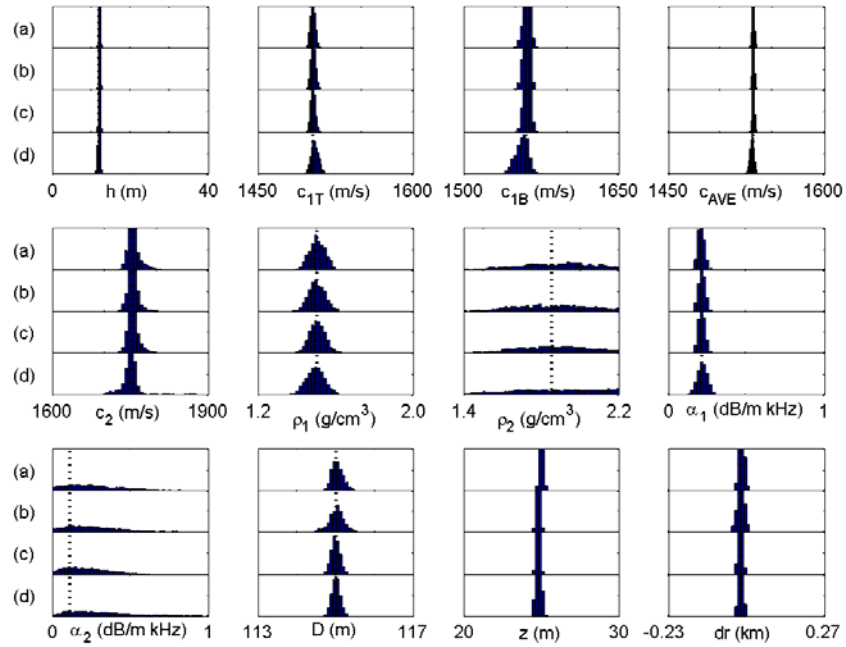

Figure 4.12: Effect of source azimuth (long array). Marginal PPDs for sources at bearings of: (a) 0°, (b) 30°, (c) 60°, and (d) 90°. Array is 1024 m long with 33 sensors.

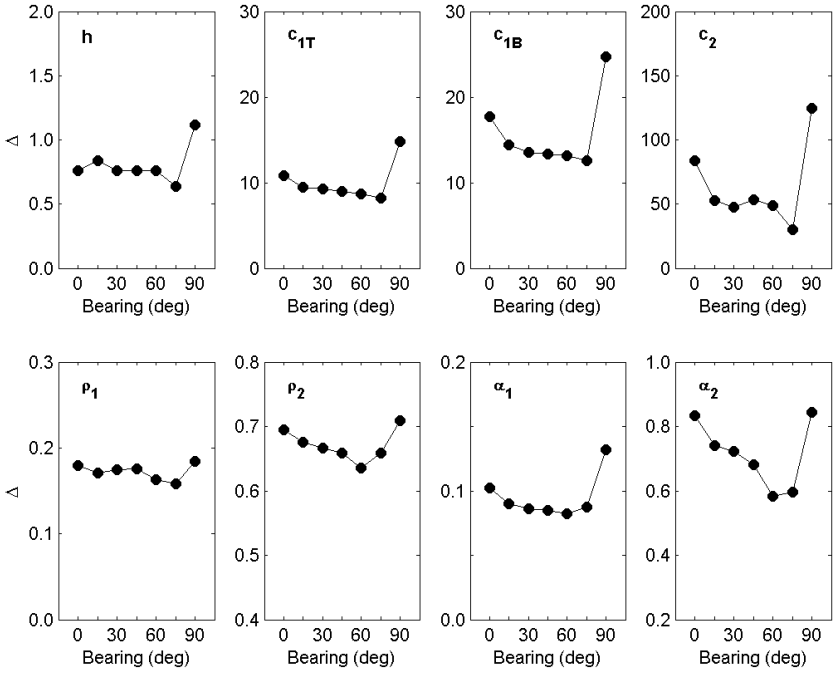

Figure 4.13: 95% HPD credibility intervals versus source bearing for long array.

reduced effective element spacing. The credibility intervals increase at broadside; however, there is still useful geoacoustic information content for parameters of the sediment layer. The sensitivity to geoacoustic parameters for a broadside source is due to the difference in source-receiver range between sensors at the mid-point and ends of the array, this difference is approximately 40 m for the long array (and source range) considered here.

4.3.6. Ship-noise data

Ship noise has been used for inversion of VLA (Chapman, Dizaji, and Kirlin, 2000) and HLA data (Koch and Knobles, 2005). Ship noise is typically prominent at frequencies below 200 Hz and at lower source levels than those of a controlled-source experiment. In this section, three changes are introduced to simulate inversion of ship-noise data: the frequency band is shifted down to 50–150 Hz, the source is at 5-m depth, and the ESNR is lowered to 2 dB at all frequencies. The canonical array is considered with a source at endfire.

Figure 4.14 displays inversion results for broadband and narrowband ship-noise data (21 and 3 frequencies, respectively). The results indicate that broadband ship-noise data provide reasonable resolution of the sediment sound speed (c_{1T}, c_{1B} and h), although the resolution is notably poorer than for the canonical case, Fig. 4.2(c). In contrast, ρ_1 and basement parameters are better resolved than for the canonical case. This is likely due to the greater penetration depth of the low-frequency ship noise. With narrowband ship-

noise data, the sediment sound speed parameters (c_{1T}, c_{1B}) are poorly resolved, while the overall sound-speed structure of the seabed (c_{AVE}, h, and c_2) is reasonably well resolved.

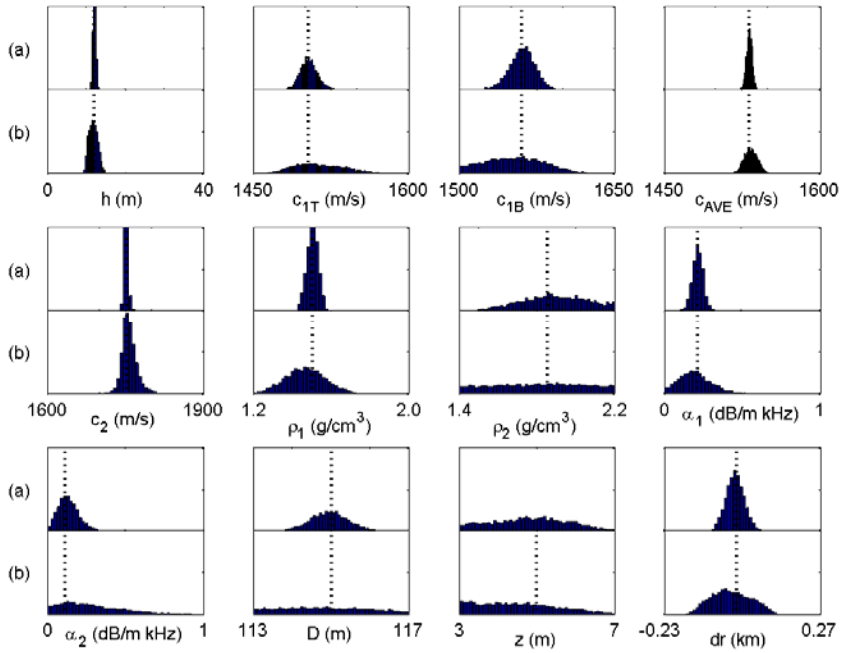

Figure 4.14: Ship-noise source. Marginal PPDs for (a) broadband ship noise (21 frequencies over 50–150 Hz at 2-dB ESNR); and (b) narrowband ship noise (3 frequencies over 50–150 Hz at 2-dB ESNR).

4.3.7. Towed-array data

The use of towed-array data for geoacoustic inversion is a topic of recent research interest, with applications to the use of controlled-source data (Jesus and Caiti, 1996; Siderius, Nielsen, and Gerstoft, 2002) and ship self-noise (Battle et al., 2003, 2004; Fialkowski et al., 2006). Towed arrays of practical interest are limited to relatively short length and source-receiver separations. A typical configuration is here adapted from the MAPEX2000 experiments (Siderius, Nielsen, and Gerstoft, 2002) consisting of a 65-

sensor, 256-m long array towed at 60-m depth with a source-array separation of 300 m (measured to the first element of the array). Three sources are considered: a controlled source at 55-m depth comprising 7 frequencies over 200–500 Hz at 6–4.5-dB ESNR; and narrowband and broadband ship-noise sources at 5-m depth comprising 3 and 21 frequencies, respectively, over 50–150 Hz at 2-dB ESNR. The results, displayed in Fig. 4.15, are in accordance with previous simulations: geoacoustic information resolution is highest for the controlled source, poorer for broadband ship-noise data (except for c_2 and ρ_2), and poorest for narrowband ship-noise data. The use of controlled-source data and a towed array provides results comparable to the canonical case, Fig. 4.2(c), for sediment parameters, and slightly better results for substrate parameters (c_2, ρ_2 and α_2).

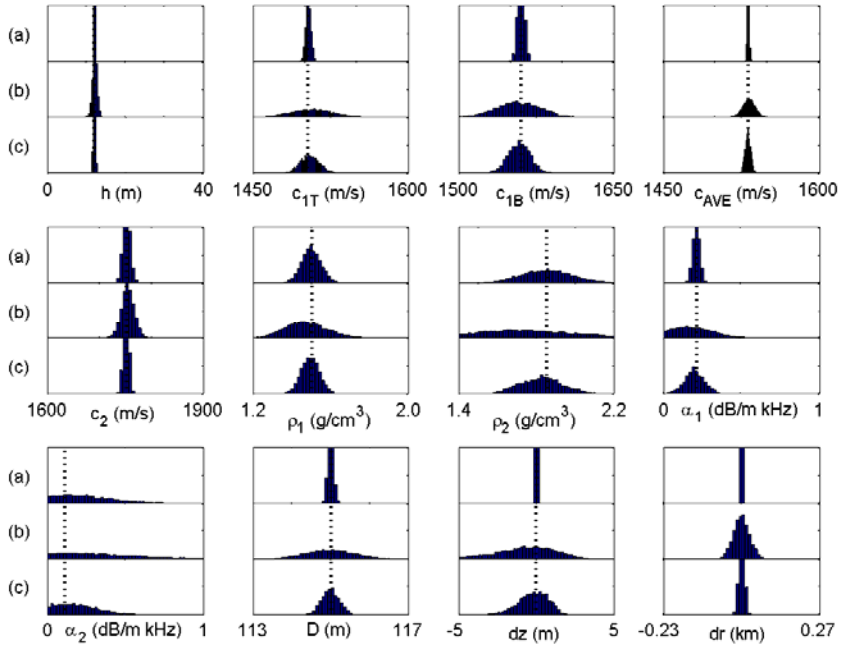

Figure 4.15: Towed array. Marginal PPDs for: (a) controlled source at 55-m depth (7 frequencies over 200–500 Hz at 6–4.5-dB ESNR); (b) narrowband ship noise at 5-m depth (3 frequencies over 50–150 Hz at 2-dB ESNR); and (c) broadband ship noise at 5-m depth (21 frequencies over 50–150 Hz at 2-dB ESNR). Array is 256 m long with 65 sensors.

4.3.8. Comparison with VLA

As discussed in the introduction, the traditional experimental tool for MFI has been a VLA, typically spanning the water column. Results from inversions of VLA and HLA data were compared in Siderius, Nielsen, and Gerstoft (2003), and Tollefsen, Wilmut, and Chapman (2005). In this section, geoacoustic information content of similarly configured vertical and horizontal arrays is compared. Figure 4.16 compares marginal PPDs for a 108-m length, 28-element, bottom-moored HLA with a VLA of 28 elements spaced at 4-m intervals from 4–112 m in depth, both arrays at 3.23 km range. In each case, the data consist of 7 frequencies from 200–500 Hz at 6–4.5-dB ESNR. The figure shows that while the geometric parameters (source location and water depth) are resolved better with the VLA, the seabed geoacoustic parameters are equally well

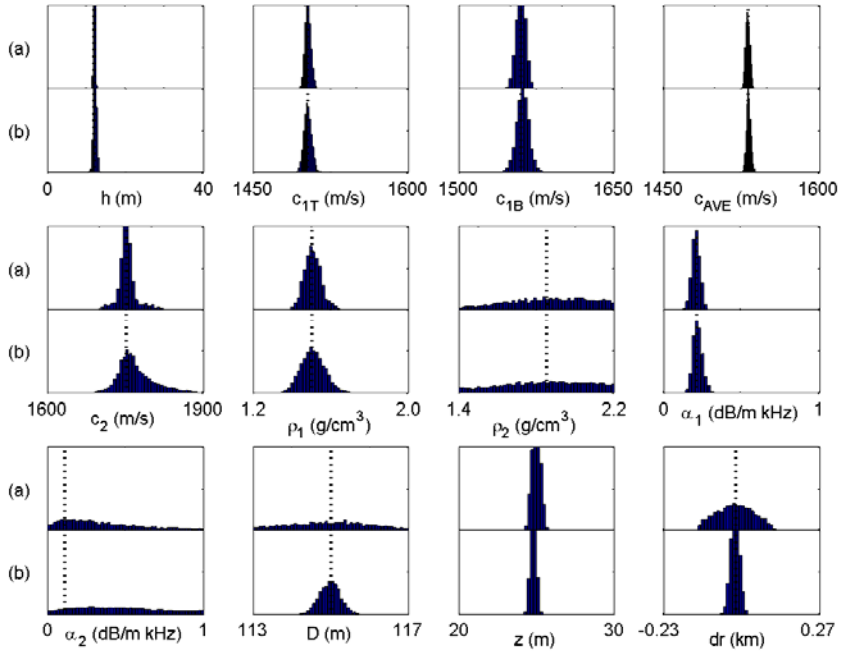

Figure 4.16: HLA/VLA comparison. Marginal PPDs for: (a) 108-m long HLA with 28 sensors and (b) 108-m long VLA with 28 sensors. Source-array range 3.23 km.

resolved by the HLA and the VLA. Other choices of array and experiment factors such as shorter source-array range may yield improved performance for a VLA (Dosso and Wilmut, 2002); the example provided here should not be generalized to every array configuration and experiment setting.

4.4. Summary

This chapter examined the effectiveness of HLAs for MFI by quantifying geoacoustic information content in terms of marginal posterior probability distributions for seabed parameters. Several HLA types were considered, including bottom-moored arrays of a variety of configurations and a towed array, and comparison was made to a VLA. Source factors considered included frequency content, noise level, and depth, so as to simulate both controlled sources and ship noise. The effect of source bearing (relative to the array) was also considered. HLA factors included array length, number of sensors and sensor separation, and source-array range. While the general behaviour of some cases could be predicted from a basic understanding of ocean acoustic propagation, the Bayesian approach applied here provides a quantitative measure of the effect of specific array and source factors on the accuracy achievable in geoacoustic inversion.

The intention has not been to present an exhaustive study of HLA performance in all settings. In particular, results may differ somewhat for different seabed types (e.g., sediments with sound speed less than that of water). However, several observations can be made. Data from a bottom-moored HLA yielded similar geoacoustic information content to data from a VLA of equal length that spanned the water column. For the HLAs

investigated, the array length and the number of sensors/inter-sensor spacing are important system factors that strongly effect geoacoustic information content. In particular, HLAs that are too short can preclude useful geoacoustic information. Reasonably good geoacoustic resolution was achieved for arrays of length of the order of the water depth and with a sufficient number of sensors. Geoacoustic information content in general degrades with increasing source-array range (except for sediment density). However, information content does not necessarily degrade as the source bearing increases from endfire until the source is close to broadside. Further, for a sufficiently long array, data from sources at broadside can yield useful information content on seabed properties.

Simulations designed to emulate data for ship noise sources indicated a degradation of the resolution of geoacoustic parameters when compared to controlled-source data; however, reasonable results were obtained both for broadband and narrowband ship-noise data, with best results for broadband ship-noise data. Towed-array data (for a controlled source) provided results comparable to those obtained with a bottom-moored HLA of similar length.

Chapter 5 Geoacoustic inversion of controlled-source data

5.1. Introduction

This chapter considers matched-field geoacoustic inversion of acoustic data recorded on a bottom-moored HLA due to a continuous-wave source in the context of the Barents Sea 03 shallow water experiment. The towed acoustic source transmitted low-frequency (30–160 Hz) CW tones at sound levels comparable to those of a merchant ship, with resulting SNR at the array of 9–15 dB. Thus, the experiment emulated conditions (apart from source depth) closer to those of using noise from ships of opportunity for MFI rather than those of more-traditional inversion experiments using high-level broadband sources. The HLA measurements also differ from previous reported experiments in that the array is longer (900 m) but sparser (18 elements), and in that the experimental site was located in a continental shelf environment characterized by relatively compact (glacigenic) sedimentation. In addition to the acoustic data, a number of types of geophysical data (seismic reflection and refraction, bottom-penetrating sonar, gravity core, described in Chapter 2) were collected at the experiment site to provide independent information on bottom properties for comparison with the MFI results.

Bayesian MFI is applied to estimate parameter values, mean deviation uncertainties, one-and two-dimensional marginal probability distributions, and inter-parameter correlations for a layered seabed model using the nonlinear numerical approach based on Metropolis-Hastings sampling (described in Chapter 3). Inversion is applied to cross-

spectral density matrices formed by averaging spectra from a sequence of time-series subsegments (data snapshots). Defining the data uncertainties, including both measurement and theory errors, is an important component of Bayesian analysis. To date, data error estimation for MFI of snapshot-averaged acoustic data has been based on one of two assumptions: either that the averaging procedure reduces the errors as if they are fully independent from snapshot to snapshot (an optimistic assumption; Mecklenbräuker and Gerstoft, 2000), or that the averaging procedure does not reduce the error at all (a pessimistic assumption; Battle et al., 2004). This chapter develops a new approach to quantifying errors for snapshot-averaged data based on the assumption that the averaging procedure reduces measurement error, dominated by ambient noise which may reasonably be assumed independent from snapshot to snapshot, but does not significantly reduce theory error, dominated by modelling errors which are generally not independent. This approach provides a physically-reasonable intermediate result between the optimistic and pessimistic assumptions. The work in this chapter has been published as Tollefsen, Dosso, and Wilmut (2006).

5.2. Data processing

The recorded acoustic pressure-time series at the array were fast Fourier transformed and, from resulting spectra, the frequency bin of maximum power at or near each nominal source frequency was selected for analysis. CSDM estimates $\hat{\mathbf{C}}_f$ were formed by averaging over the complex pressures corresponding to K time-series subsegments (data snapshots):

$$\hat{\mathrm{C}}_f = \frac{1}{K}\sum_{k=1}^{K} \mathrm{d}_{fk}\mathrm{d}_{fk}^{\dagger} = \left\langle \mathrm{d}_f \mathrm{d}_f^{\dagger} \right\rangle. \tag{5.1}$$

In Eq. 5.1, $\mathbf{d}_{fk}$ represents the vector of complex-pressure data along the array at the fth frequency corresponding to the kth snapshot and $\langle\cdot\rangle$ represents snapshot averaging. The processing sequence for towed-source data consisted of averaging K =5 snapshots each of length 6.6 s, with a Hamming windowing function applied and 50% snapshot overlap. The total averaging time was 19.8 s, over which the source moved approximately 50 m. Ambient noise levels were estimated using the Order-Truncate-Average algorithm (Nielsen, 1991) in small frequency bands surrounding each processing frequency. The estimated average SNR at each frequency is defined by

$$\mathrm{SNR}_f = 10\log_{10}\frac{\left\langle \left|\mathbf{d}_f\right|^2 \right\rangle - \left\langle \left|\mathbf{n}_f\right|^2 \right\rangle}{\left\langle \left|\mathbf{n}_f\right|^2 \right\rangle}, \tag{5.2}$$

where $\mathbf{n}_f$ and $\mathbf{d}_f$ represent noise and data vectors, respectively. The estimated SNR values vary from 9 to 15 dB for the data considered in this chapter.

5.3. Likelihood function and snapshot averaging

Chapter 3 defined the likelihood function for the case of a single data snapshot and known data error variance. This chapter describes three approaches for treating variances that incorporate multiple-snapshot data, one of which is new.

Consider the case of K>1 data snapshots, $\mathbf{d}_{fk}$, k =1,K with the variance of all snapshots at the fth frequency given by ν_f. Two approaches appear to have been applied to date to

incorporate multiple data snapshots in Bayesian MFI. In one approach (Battle et al., 2004) an estimate of the CSDM given by Eq. 5.1 is used in place of the single snapshot CSDM in the likelihood function, error function, and Bartlett mismatch given by Eqs. 3.16–3.18. That is, single snapshot data are replaced by snapshot-averaged data without otherwise altering the likelihood function L_1 (Eq. 3.16) or error function E_1 (Eq. 3.17). The second approach (Mecklenbräuker and Gerstoft, 2000) is based on assuming that the errors on the K data snapshots are independent, so that the multiple snapshots are incorporated by multiplying the corresponding single snapshot probabilities, leading to

$$L(\mathbf{m}) = \prod_{k=1}^{K} \prod_{f=1}^{F} \frac{1}{(\pi \nu_f)^N} \exp[-|\mathbf{d}_{fk} - A_{fk} e^{i\theta_{fk}} \mathbf{d}_f(\mathbf{m})|^2 / \nu_f], \tag{5.3}$$

where $\mathbf{d}_f(\mathbf{m})$ represents modelled (replica) data predicted for model $\mathbf{m}$, and A_{fk} and θ_{fk} represent unknown source amplitude and phase. Employing ML estimates for source terms leads to

$$L_3(\mathbf{m}) = \prod_{f=1}^{F} \frac{1}{(\pi \nu_f)^{NK}} \exp[-B_f(\mathbf{m})/(\nu_f / K)], \tag{5.4}$$

$$E_3(\mathbf{m}) = \sum_{f=1}^{F} B_f(\mathbf{m})/(\nu_f / K), \tag{5.5}$$

where the Bartlett mismatch (Eq. 3.18) is defined with the snapshot-averaged CSDM given by Eq. 5.1.

The two approaches to incorporating multiple snapshot data described above differ in the variance applied to the Bartlett mismatch. In the first approach, the variance applied in L_1 and E_1 is equal to the single snapshot variance ν_f, while in the second approach the variance applied in L_3 and E_3 is ν_f / K. The two approaches represent end-case interpretations: the first approach assumes that snapshot averaging results in no reduction

in the effective data variance (i.e., that errors on multiple snapshots are not random), while the second approach assumes the maximum reduction in variance (i.e., the reduction for fully independent random snapshot errors). In general, applying the first approach will lead to model parameter uncertainties that are overly pessimistic, while the second approach leads to parameter uncertainties that are overly optimistic.

This chapter proposes an *effective variance* estimate for snapshot-averaged data based on (approximately) apportioning the single snapshot data variance ν_f as the sum of a measurement-error component ν_f^{ME} and a theory-error component ν_f^{TE}:

$$\nu_f = \nu_f^{ME} + \nu_f^{TE}. \tag{5.6}$$

Measurement error is often dominated by ocean ambient noise, and may reasonably be assumed to be independent from snapshot to snapshot. On the other hand, theory error is generally dominated by modelling errors due to the simplified model parameterization and approximate physics of the forward problem. These errors are generally not independent from snapshot to snapshot (e.g., identical modelling errors over snapshots are expected for fixed source/receiver geometry and stable environment). Hence, in deriving the effective variance estimate for snapshot averaged data, $\bar{\nu}_f$, it is reasonable to assume that the measurement-error variance component is reduced by a factor of $1/K$, while the theory-error component is not reduced at all:

$$\bar{\nu}_f = \nu_f^{ME} / K + \nu_f^{TE}. \tag{5.7}$$

To see this, consider *K* realizations of an error (noise) process $n_k, k = 1, K$ consisting of measurement error n_k^{ME} and theory error n^{TE} (assumed constant over *k*)

$$n_k = n_k^{ME} + n^{TE}, \tag{5.8}$$

where n_k^{ME} and n^{TE} are zero-mean independent random processes with variances ν^{ME} and ν^{TE}, respectively. The variance of the mean of these realizations is given by

$$\begin{aligned}\bar{\nu} &= \left\langle \left[\frac{1}{K} \sum_{k=1}^{K} n_k^{ME} + n^{TE} \right]^2 \right\rangle \\ &= \frac{1}{K^2} \sum_{k=1}^{K} \sum_{j=1}^{K} \left\langle n_k^{ME} n_j^{ME} \right\rangle + \left\langle n^{TE} n^{TE} \right\rangle + \left\langle n_k^{ME} n^{TE} \right\rangle + \left\langle n_j^{ME} n^{TE} \right\rangle \\ &= \frac{1}{K^2} \left[K \nu^{ME} + K^2 \nu^{TE} \right] = \nu^{ME} / K + \nu^{TE}, \end{aligned} \tag{5.9}$$

as assumed in Eq. 5.7 (here, $\langle \cdot \rangle$ defines the expectation operator). Taking into account snapshot averaging effects in this manner, the likelihood and error functions become

$$L_4(\mathbf{m}) = \prod_{f=1}^{F} \frac{1}{(\pi \bar{\nu}_f)^N} \exp[-B_f(\mathbf{m}) / \bar{\nu}_f], \tag{5.10}$$

$$E_4(\mathbf{m}) = \sum_{f=1}^{F} B_f(\mathbf{m}) / \bar{\nu}_f, \tag{5.11}$$

where $B_f(\mathbf{m})$ is based on the cross-spectral data average, Eq. 5.1.

To estimate the single snapshot measurement and theory variance components, consider the definition of the SNR as the ratio of the average received signal level to the average ambient noise level given by Eq. 5.2. Assuming the ambient noise $\mathbf{n}_f$ is due to an independent, complex Gaussian-distributed random process with variance ν_f^{ME} leads to

$$\mathrm{SNR}_f = 10 \log_{10} \frac{\left\langle \left| \mathbf{d}_f \right|^2 \right\rangle - \nu_f^{ME} N}{\nu_f^{ME} N}. \tag{5.12}$$

Equation 5.12 can be solved for the measurement variance component in terms of the SNR:

$$\nu_f^{ME} = \frac{\left\langle \left| \mathbf{d}_f \right|^2 \right\rangle}{N\left(10^{\mathrm{SNR}_f/10} + 1\right)}, \tag{5.13}$$

and the theory variance component ν_f^{TE} can then be estimated from Eq. 5.6 (assuming that ν_f is known).

The development so far has assumed that the data variances ν_f are known *a priori*, which is often not the case. Under the assumption of Gaussian-distributed errors, variances can be estimated from the data (see Chapter 3.7). Explicit variance estimates $\hat{\nu}_f$ are here obtained by evaluating Eq. 3.30 at the ML model estimate obtained by minimizing the error function Eq. 3.31, with $B_f(\mathbf{m})$ based on the cross-spectral data average, Eq. 5.1. Once $\hat{\nu}_f$ is estimated, $\hat{\nu}^{TE}$ is calculated using Eq. 5.6 with $\hat{\nu}_f$ replacing ν_f. These variances can be used as fixed estimates in Bayesian MFI by Metropolis-Hastings sampling E_4, as given by Eqs. 5.11 and 5.7, with $\hat{\nu}_f^{TE}$ replacing ν_f^{TE}.

It is interesting to consider the reduction in variance over the pessimistic case achieved by the effective variance estimate, Eq. 5.7, which can be quantified as

$$A_f = \frac{\bar{\nu}_f}{\hat{\nu}_f} = \frac{\hat{\nu}_f^{ME}/K + \hat{\nu}_f^{TE}}{\hat{\nu}_f}. \tag{5.14}$$

The variance-reduction factor A_f can also be formulated in terms of the SNR and the effective signal-to-noise ratio ESNR (defined in Eq. 4.3) which provides a measure of the signal level compared to all sources of error (measurement and theory). The variance reduction can be written

$$A_f = 1 - \left(1 - \frac{1}{K}\right)\frac{10^{\mathrm{ESNR}_f/10}+1}{10^{\mathrm{SNR}_f/10}+1}. \tag{5.15}$$

The two extremes are SNR = ESNR (i.e., negligible theory error) where $A_f = 1/K$ and SNR≫ESNR (negligible measurement error) where $A_f \to 1$. Figure 5.1 shows the variance reduction factor A as a function of the number of snapshots K and the SNR–ESNR difference (assuming ESNR = 5 dB, representative of the data considered in this chapter). The reduction is most pronounced for low SNR and large K, and hence is important in this chapter as well as in low-SNR applications such as ship-noise inversion.

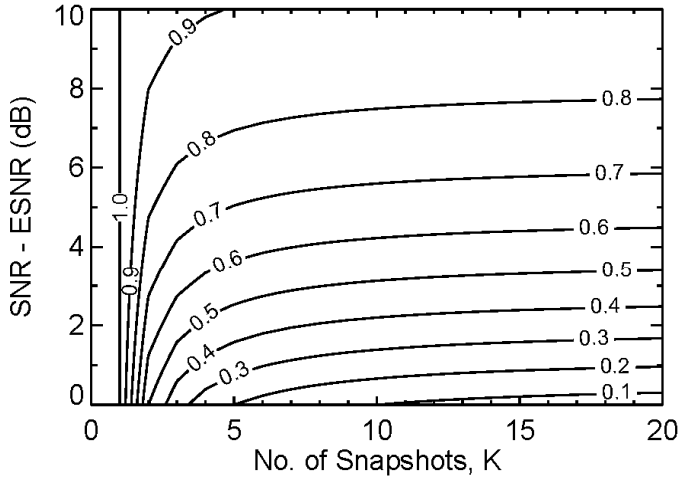

Figure 5.1: Variance reduction factor A as a function of number of snapshots K and the SNR–ESNR difference (assuming ESNR=5 dB).

5.4. Inversion results

5.4.1. Variance estimation

This section examines the effect of the different variance estimates described in Chapter 5.3 for experimental HLA data as a prelude to considering inversion results in detail in the following section. (The acoustic experiment is described in Chapter 2). HLA data for the source at a range of 1.58 km (east track, Fig. 2.1) were selected for this analysis. Variances were estimated at each of the five source frequencies using Eqs. 3.30 and 3.31, with ASSA applied to compute the ML model estimate. The ESNR, which compares the signal level to the total error, was computed using Eq. 4.3. The SNR was estimated using Eq. 5.2, and the measurement-error and theory-error variances were computed using Eqs. 5.13 and 5.6. SNR and ESNR estimates at the five processed frequencies are shown in Fig. 5.2 (middle panel).

For the inversions, Metropolis-Hastings sampling was applied to error function E_4 of Eq. 5.11. The environmental model used in the inversions is discussed in Chapter 2.3 (Fig. 2.3). In addition to the seabed geoacoustic parameters, the model also includes several geometric parameters of the experiment which are not otherwise known to sufficient accuracy. These parameters include the water depth, D, source depth and bearing, z and b, and a correction to source-receiver range, dr. The inversion search bounds applied for the geoacoustic and geometric parameters are given in Table 5.1. Replica acoustic fields were generated using the normal-mode propagation model ORCA (Westwood, Tindle, and Chapman, 1996) using a complex-plane mode search to accurately model near-field effects due to leaky (continuous) modes. Numerical

parameters of the ORCA model were set to values recommended in Westwood and Koch (1999).

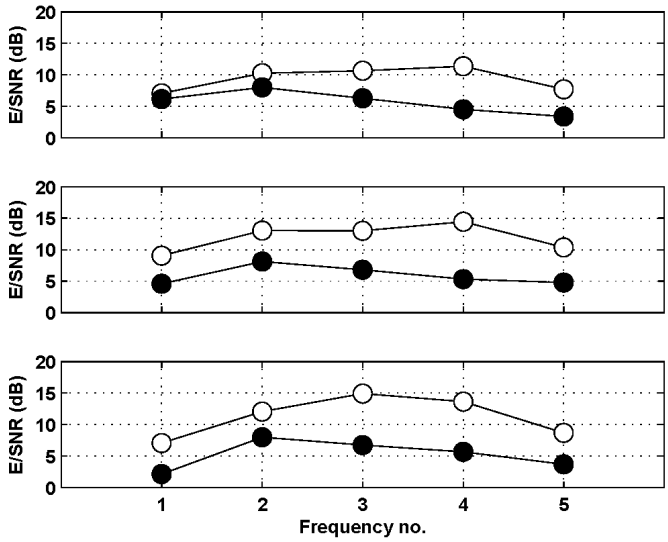

Figure 5.2: Estimated SNR (open circles) and ESNR (filled circles) for various source frequencies for the experimental data. Upper: short-range west track data (1.51 km); middle: short-range east-track data (1.58 km); lower: long-range east-track data (5.17 km).

Parameter and units	Lower Bound	Upper Bound
Geoacoustic		
h (m)	1.0	40
c_1 (m/s)	1450	1900
c_2 (m/s)	c_1	c_1+30h
ρ_1 (g/cm^3)	1.40	3.00
ρ_2 (g/cm^3)	1.40	3.00
α_1 (dB/m kHz)	0.01	1.00
α_2 (dB/m kHz)	0.01	1.00
Geometric		
D (m)	278	288
dr (km)	-0.10	+0.15
z (m)	50	58
b (°)	27	30

Table 5.1: Model parameters and search bounds used in Barents Sea data inversions.

Before presenting inversion results for different data variance estimates, it is worth considering the underlying assumptions on the data errors. The assumptions that the errors are Gaussian distributed and spatially uncorrelated were examined by applying statistical tests to the standardized data residuals (Eq. 3.38) at each frequency and data snapshot. The KS test indicated no significant evidence against Gaussianity at a 0.05 level of significance for any of the data snapshots considered in this chapter, while the runs test provided no evidence against spatial randomness at a 0.05 level of significance for approximately 95% of the snapshots. (Tests for residual correlation over frequency are not meaningful in this context due to the small number of samples available for testing.) Hence, there is no significant evidence against the error assumptions underlying the Bayesian analysis.

Geoacoustic inversion results for the HLA data are presented in Fig. 5.3 for the three approaches to variance estimation for snapshot-averaged data using K=5 snapshots. The variance reduction factor (Eq. 5.15) for the effective variance estimate, averaged over frequency, is A=0.75. Marginal PPDs are presented for the seven geoacoustic model parameters described in Table 5.1 and for an additional geoacoustic parameter consisting of the average sound speed in the upper layer defined by Eq. 4.5 (with c_1 and c_2 replacing c_{1T} and c_{1B}, respectively). Note that for some parameters the plot limits in Fig. 5.3 are narrower than the prior bounds used in the inversions (Table 5.1).

The width of the marginal PPDs for all parameters decrease systematically in going from the pessimistic variance estimate to the effective variance estimate to the optimistic variance estimate. This can be quantified in terms of parameter mean deviations (Eq. 3.9), a robust measure of uncertainty that is not as sensitive to a small number of sample

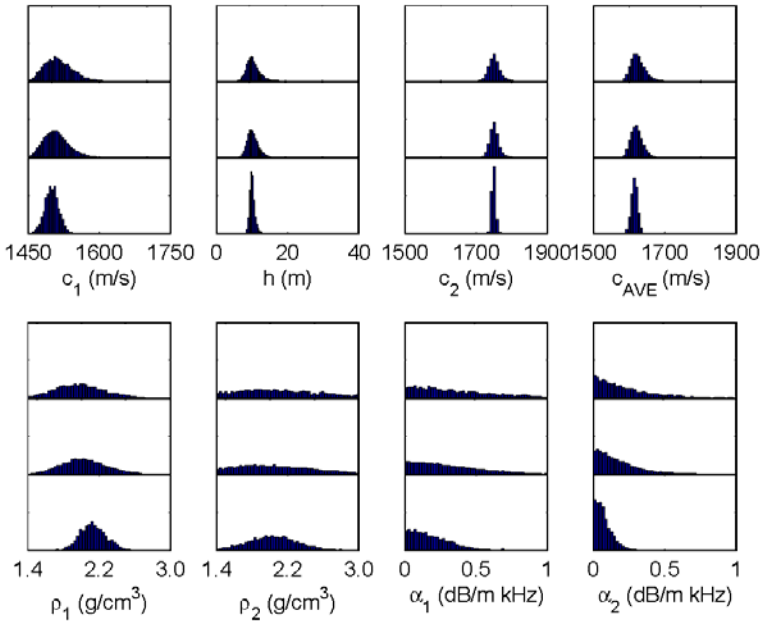

Figure 5.3: Marginal PPDs for different approaches to data variance estimation. Upper distributions correspond to pessimistic variance estimates, middle distributions to effective variance estimates, and lower distributions to optimistic variance estimates.

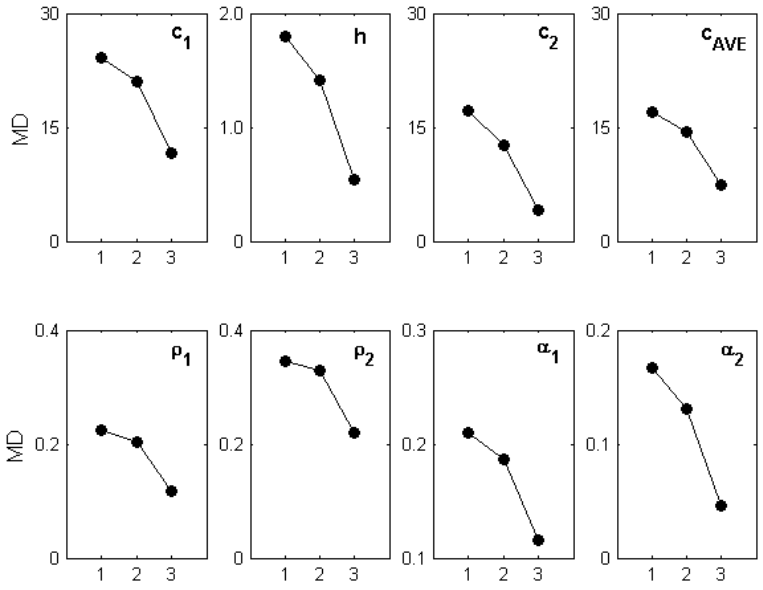

Figure 5.4: Geoacoustic posterior uncertainty estimates quantified in terms of mean absolute deviations for: 1–Pessimistic variance estimates, 2–Effective variance estimates, and 3–Optimistic variance estimates. Parameter units vary between plots and are given in Table 5.1.

outliers as the standard deviation. The MDs for the three variance estimates are compared in Fig. 5.4. The MDs for the effective variance estimates are reduced by 5–30% over those for the pessimistic estimates, while the optimistic MDs are reduced a further 30–50% over the effective-variance MDs. It is worth emphasizing here that the goal of Bayesian inversion is not to compute the smallest parameter uncertainties, but rather the most meaningful parameter uncertainties (i.e., uncertainties that correctly quantify the geoacoustic information content of the data). As discussed in Chapter 5.3, the effective variance estimates represent a physically-reasonable compromise between the optimistic and pessimistic variance estimates.

5.4.2. Source range and bearing effects

This section considers geoacoustic inversion results for experimental data collected for three different source positions at the Barents Sea site, including short-range (1.58-km) and long-range (5.17-km) data along the east track and short-range (1.51-km) data along the west track (Fig. 2.1). Data processing involved averaging over K=5 snapshots and inversions were carried out using effective variance estimates. SNR and ESNR values at the five source frequencies are shown in Fig. 5.2 for the three source positions (note that the source level was 6 dB higher for the long-range data than for the short-range data). Frequency-averaged variance reduction factors were approximately 0.75 for all three data sets. Geoacoustic inversion results for the three data sets are shown in Fig. 5.5 in terms of marginal PPDs and summarized in Table 5.2 in terms of mean parameter estimates with one mean-deviation uncertainties.

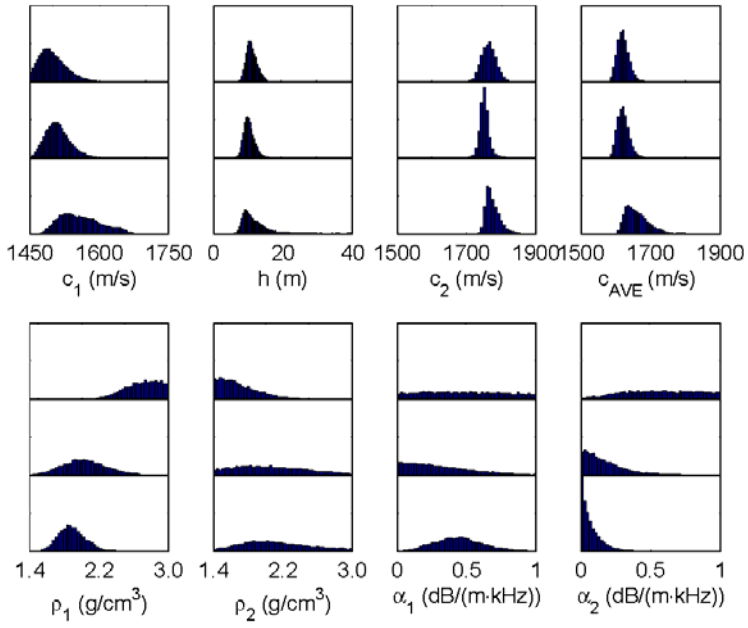

Figure 5.5: Marginal PPDs for data at 1.51 km along west track (upper distributions), 1.58 km along east track (middle distributions), and at 5.17 km along east track (lower distributions).

Parameter and units	r=1.58 km east	r=1.51 km west	r=5.17 km east	Geophysical data
h (m)	11.2±1.4	11.7±1.2	14.0±4.4	10-20
c_1 (m/s)	1510±21	1501±24	1559±37	1500-1520
c_2 (m/s)	1753±13	1763±17	1783±26	1745
c_{AVE} (m/s)	1623±14	1621±13	1663±29	
ρ_1 (g/cm^3)	2.03±0.20	2.7±0.16	1.89±0.13	2.0-2.1
ρ_2 (g/cm^3)	2.06±0.33	1.71±0.21	2.12±0.31	
α_1 (dB/m kHz)	0.32±0.18	0.50±0.23	0.45±0.14	
α_2 (dB/m kHz)	0.21±0.13	0.57±0.21	0.10±0.06	

Table 5.2: Geoacoustic parameter estimates (mean with mean-deviation uncertainties) from inversion of controlled-source data at indicated ranges r and source track. Also included are approximate values from the supporting geophysical measurements.

The parameters defining the sound-speed profile in the seabed, h, c_1, c_2, and c_{AVE}, are reasonably well determined, particularly for the short-range data sets. Considering these parameters first, Table 5.2 indicates that the posterior-mean parameter estimates are consistent between the three data sets (within estimated uncertainties). There is particularly close agreement between the parameter estimates and the uncertainties for the two short-range data sets. The differences between the parameter estimates for the long-and short-range data are significantly larger than the differences between the two short-range data sets. In addition, the parameter uncertainties are substantially larger for the long-range data set, indicating these data are less informative for seabed sound speed. In particular, the uncertainty estimates for the halfspace sound speed c_2 and layer thickness h are approximately two and three times larger than for the short-range data sets, respectively. This is likely because the higher-order modes of the acoustic field are more strongly attenuated with range, leaving the lower-order modes which propagate at smaller grazing angles with shallower bottom penetration, and hence are less sensitive to deeper structure. The surficial sound speed c_1 is also not as well determined for the long-range data (mean deviation almost twice as large as for short-range data). This may also be due to the attenuation of higher-order modes and the consequential loss of resolution of surficial structure provided by the short vertical wavelengths of these modes. For all data sets, the uncertainty of the halfspace sound speed c_2 is significantly smaller than that for the surficial sound speed c_1 or the average layer sound speed c_{AVE}.

Figure 5.5 and Table 5.2 indicate that the seabed density and attenuation parameters are generally not well determined, as is commonly the case in MFI studies. While the density estimates for the two east-track data sets are reasonable, the combination of a

relatively high ρ_1 estimate and low ρ_2 estimate for the west-track data is unlikely to be correct. It is also worth noting that attenuation estimates from geoacoustic inversion typically account for a variety of loss mechanisms, including the effects of bottom roughness and inhomogeneity, and are often higher than the intrinsic attenuation of the seabed. The density and attenuation parameters are generally better determined for the long-range data than for the short-range data. This is in agreement with other reported inversions of long-range acoustic data (e.g., Dosso and Wilmut, 2002; Koch and Knobles, 2005), and appears to be due to the accumulated effect of bottom interaction with range.

To further investigate parameter uncertainties, it is useful to consider inter-parameter correlations and joint marginal distributions. Figure 5.6 shows the correlation matrix for the short-range east-track data (correlation matrices for the other data sets are similar). Significant positive correlations are evident between h and both c_1 and c_2, indicating, in that case, the acoustic data have limited ability to discern between a thinner, slower layer and a thicker, faster layer. In terms of the geometric parameters, strong positive correlations exist between the water depth D, source depth z, and range correction dr (particularly between D and z). Since correlations between geoacoustic and geometric parameters are small, the uncertainties in the experiment geometry likely do not significantly affect geoacoustic uncertainties in this case. This is in contrast to inversion results of VLA data for a low sound-speed seabed in the Mediterranean Sea (Dosso and Nielsen, 2002) which exhibited a strong negative correlation between water depth and sediment thickness, indicating that in that case uncertainty in water depth degraded geoacoustic knowledge. Figures 5.7 and 5.8 show joint marginal PPDs for the short and

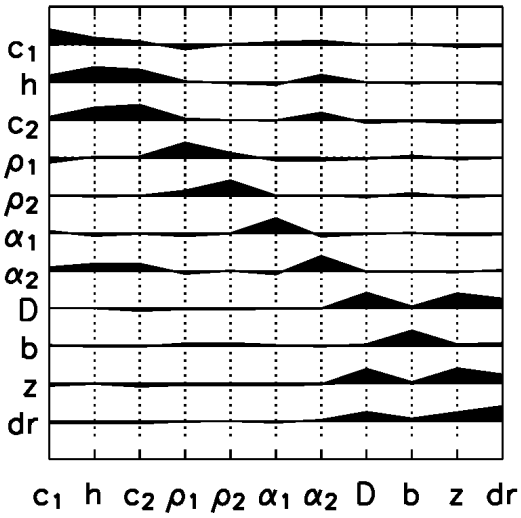

Figure 5.6: Parameter correlation matrix for short-range east-track data.

long-range data, respectively, for selected pairs of parameters (both correlated and uncorrelated). The joint marginal distributions for h and c_1, h and c_2, and D and r illustrate how the above correlations increase parameter uncertainties. The larger uncertainties for most parameters for the long-range data are evident in comparing Figs. 5.7 and 5.8.

5.4.3. Comparison to geophysical measurements

It is important to compare the geoacoustic inversion results to the geophysical measurements (described in Chapter 2), which are summarized in Table 5.2. The surficial sound-speed estimates of c_1= 1510 ± 21, 1501 ± 24, and 1559 ± 37 m/s for the short-and long-range data are in good agreement with the gravity core (Fig. 2.2), which indicated an average sound speed of 1500–1520 m/s over the top 1.7 m of sediments.

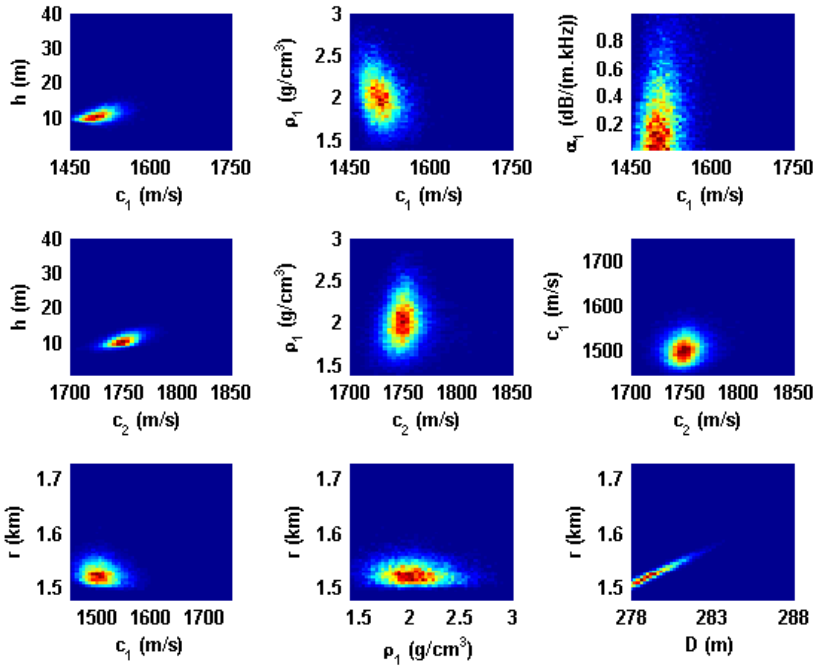

Figure 5.7: Selected joint marginal PPDs for short-range east-track data.

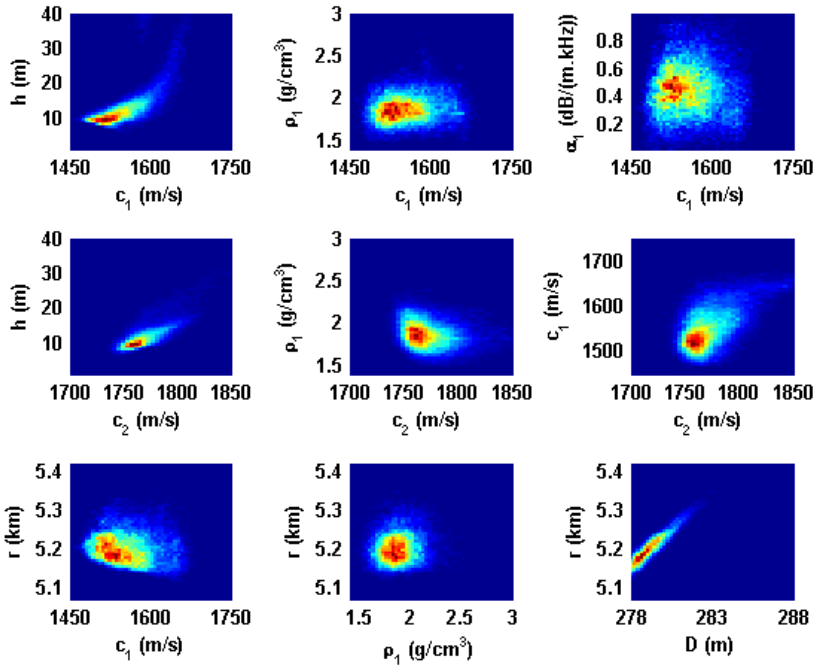

Figure 5.8: Selected joint marginal PPDs for long-range data.

Further, the halfspace sound-speed estimates of c_2=1753 ± 13, 1763 ± 17, and 1783 ± 26 m/s are in reasonable agreement with the seismic-refraction survey, which indicated an overall sound speed of the Quaternary sediments (120–140-m thick) of 1745 m/s. It is also interesting to note that the upper layer thickness estimates of h=11.2 ± 1.4, 11.7 ± 1.2, and 14.0 ± 4.4 m are in general agreement with evidence from the bottom-penetrating sonar of a possible weak reflector at 10–20 m (however, this may be fortuitous as the geoacoustic model was designed to represent continuous gradients and not discontinuous structures). Although poorly determined, the upper-layer density estimates of ρ_1=2.03 ± 0.20 and 1.89 ± 0.13 g/cm^3 along the east track are in reasonable agreement with the gravity core which indicated a density of 2.0–2.1 g/cm^3 over the top 1.7 m of the sediments. Finally, it is noteworthy that the geoacoustic inversion results obtained here are in good general agreement with historic geophysical survey results published for glacigenic seabed sediments of the south-western Barents Sea (Sættem, Rise, and Westgaard, 1991), which indicated an average sound speed of 1550 m/s for depths < 4 m (based on data from 11 cores) and 1780 m/s for depths > 10 m (based on 33 boreholes).

5.5. Summary

This chapter presented results of Bayesian MFI applied to acoustic data collected on a bottom-moored HLA due to a towed source that transmitted low-frequency tones at levels comparable to a merchant ship. Inversions were based on matching cross-spectral density matrices computed by averaging data snapshots. An approach was developed for

estimating the effective variance of snapshot-averaged data based on the assumption that measurement errors (dominated by ambient noise) are independent and are therefore reduced by averaging, while theory (modelling) errors are not independent and not reduced. This approach provides a physically reasonable intermediate result between optimistic and pessimistic variance estimates based on assumptions of fully independent and fully dependent errors, respectively. The variance reduction factor for the effective variance estimate over pessimistic estimates reduces with increasing number of snapshots and with decreasing SNR. For the data considered here, the use of effective variance estimates provided significantly smaller geoacoustic uncertainties than pessimistic variance estimates; for inversion applications with low SNR and/or stationary sources that allow large snapshot averages, the effect could be even more pronounced.

Geoacoustic inversions were carried out for three source positions, including short-range (1.58-km) and long-range (5.17-km) data along a source track at 30º bearing east of HLA endfire and short-range (1.51-km) data along a track at 30º west of endfire. The sound-speed profile in the seabed was reasonably well determined by inversion, particularly for the short-range data sets. Recovered sound speeds and layer thicknesses were consistent within uncertainties for all three data sets, with close correspondence in estimates and uncertainties for the short-range data. The estimated surficial sediment sound speed was in good agreement with gravity core measurements and the halfspace sound speed agreed with results from a wide-angle seismic refraction survey carried out at the experiment site. The surficial and halfspace sound speeds also agreed with published results for the south-western Barents Sea based on a survey of core and borehole measurements. Density and attenuation parameters were not as well determined

via geoacoustic inversion; however, there was general agreement between inversion results and local core measurements of density for two source positions. While the upper and lower sound speeds of the geoacoustic model agree well with the geophysical measurements and historical data, the sound-speed gradient over the upper sediments is relatively high and could include the effects of a discontinuous change at a layer boundary. However, including a discontinuity in the model parameterization did not substantially change the geoacoustic inversion results, indicating that if a discontinuity exists, the acoustic data cannot resolve its presence.

The overall consistency of the recovered parameters for the sediment sound-speed profile and the good agreement with independent geophysical measurements indicates that the use of data from a bottom-moored HLA and the inversion methodology developed here produce reliable and repeatable results for the Barents Sea site.

Chapter 6 Geoacoustic inversion of ship noise

6.1. Introduction

This chapter considers geoacoustic inversion of ship-noise data from a relatively quiet surface ship collected at a bottom-moored HLA in the context of the Barents Sea 03 experiment. A Bayesian MFI method is employed to estimate model parameters and to quantify their uncertainty distributions. This allows for meaningful comparisons of the geoacoustic information content of different data sets. We demonstrate that including multiple, independent data segments in the inversion can significantly reduce uncertainties in the geoacoustic parameter estimates. The effects of ship orientation and ship range on inversion results are also quantified and discussed. Finally, results from inversion of ship noise are compared with results from inversion of controlled-source data as well as supporting geophysical data from the experiment region. The work in this chapter has been published as Tollefsen and Dosso (2008a).

6.2. Likelihood function for multiple data segments

Bayesian MFI is described in Chapter 3. The ship-noise data considered in this chapter consist of complex acoustic pressure fields measured at an N-sensor array and F frequencies corresponding to J distinct segments of the recorded acoustic pressure time series, with each time segment divided into K subsegments, i.e., $\mathbf{d} = \{\mathbf{d}_{fjk}, f=1,F; j=1,J;$

k=1,K}. The source-receiver range is considered to be fixed over the K subsegments comprising each time segment, but range varies between segments (the K subsegments, in Chapter 5 referred to as snapshots, allow for data averaging to improve SNR; the J time segments will in the following also be referred to as *data segments*). The source spectrum (amplitude and phase) is considered unknown over frequency and time. The data errors are assumed to be complex, circularly symmetric Gaussian-distributed random variables, uncorrelated in space, frequency, and time, with unknown variances which depend on frequency and time segment but are considered constant over snapshots, i.e., ν_{fj}, f=1,F; j=1,J. In this case, the likelihood function is given by

$$L(\mathbf{m}) = \prod_{f=1}^{F} \prod_{j=1}^{J} \prod_{k=1}^{K} \frac{1}{(\pi \nu_{fj})^{N}} \exp[-|\mathbf{d}_{fjk} - A_{fjk} e^{i\theta_{fjk}} \mathbf{d}_{fj}(\mathbf{m})|^2 / \nu_{fj}], \tag{6.1}$$

where $\mathbf{d}(\mathbf{m})$ represents modelled (replica) data predicted for model $\mathbf{m}$, and A and θ represent source amplitude and phase. Maximizing the likelihood over unknown variance and source spectrum by setting $\partial L(\mathbf{m}) / \partial \nu_{fj} = \partial L(\mathbf{m}) / \partial A_{fjk} = \partial L(\mathbf{m}) / \partial \theta_{fjk} = 0$ leads to the data misfit function

$$E(\mathbf{m}) = N \sum_{f=1}^{F} \sum_{j=1}^{J} \log_e B_{fj}(\mathbf{m}), \tag{6.2}$$

where $B_{fj}(\mathbf{m})$ is the Bartlett mismatch defined by

$$B_{fj}(\mathbf{m}) = \mathrm{Tr}\{\hat{\mathbf{C}}_{fj}\} - \frac{\mathbf{d}_{fj}^{\dagger}(\mathbf{m}) \hat{\mathbf{C}}_{fj} \mathbf{d}_{fj}(\mathbf{m})}{|\mathbf{d}_{fj}(\mathbf{m})|^2}. \tag{6.3}$$

In Eq. 6.3, $\hat{\mathbf{C}}_{fj}$ is the data cross-spectral density matrix for the f-th frequency and j-th time segment defined by the ensemble average over the K snapshots:

$$\hat{\mathbf{C}}_{jj} = \frac{1}{K}\sum_{k=1}^{K} \mathbf{d}_{jjk}\mathbf{d}_{jjk}^{\dagger}. \tag{6.4}$$

It is important to note the distinction between including more data in the form of more snapshots in Eq. 6.4 or more time segments in Eq. 6.2. Averaging over more snapshots generally increases the SNR; however, for a moving source, there is a limit on the number of snapshots that can be considered to correspond to a fixed range. Including more time segments adds data at different ranges which increases information content, but also increases computational effort.

6.3. Data processing

The acoustic data and supporting environmental measurements considered here were collected in the Barents Sea 03 experiment, which is described in detail in Chapter 2. The experiment region and ship tracks selected for analysis are illustrated in Fig. 2.1. The tracks were radial and oriented at angles of approximately 30° with respect to the array length axis (endfire). The ship was outbound with the stern oriented towards the array during the east (outbound) track, and inbound with the bow oriented towards the array during the west (inbound) track. The ship-to-array ranges for the ship-noise data considered here are 1.49–1.70 km and 5.09–5.30 km along the outbound track and 1.46–1.67 km along the inbound track.

Previous work (Chapter 5) considered inversion of data from a towed controlled source at five frequency components within 30–160 Hz at relatively high SNR of 9–15 dB. Considered here are selected narrowband frequency components emanating from the tow-ship recorded concurrently with the controlled-source data. The R/V H U SVERDRUP

II, a relatively quiet research ship, was moving at a constant speed of 5.2 kn (~2.7 m/s) along both tracks.

The processing sequence for the ship-noise data consisted of forming CSDM estimates from K=10 consecutive 50% overlapping data snapshots of length 3.3 s, converted to the frequency domain using a fast Fourier transform with a frequency bin width of 0.3 Hz, with a Hamming time windowing function applied. The total averaging time is 18.2 s, over which the ship moved approximately 50 m. (This processing scheme differs slightly from that used for the controlled-source data; however, the same total averaging time was used for both data types.) A simple frequency tracker was applied to follow shifts in the frequency lines of the ship between data segments. A plot of the normalized power spectral density from one hydrophone of the array (for data from the short-range outbound track) is provided in Fig. 6.1. The arrows indicate the three frequency components of the ship noise selected for inversion (the first frequency component is relatively weak in this plot). These frequency components were chosen because they are within the frequency band used for the controlled-source inversions, are known to emanate from the research ship (identified using near-field acoustic data from ship passages close to the array), and were found to be relatively stable (i.e., not of transient nature) over the period of data collection. The five highest-level frequency components in Fig. 6.1 are tones or overtones from the controlled source; additional relatively strong frequency components are either less prominent or unstable tones of the tow-ship, or could possibly originate from distant ships.

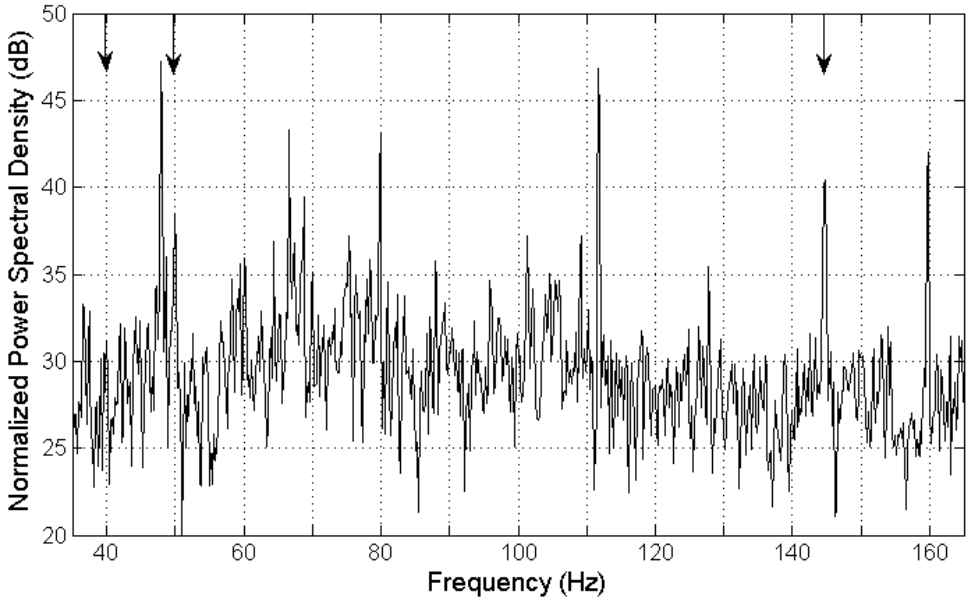

Figure 6.1: Normalized power spectral density from one hydrophone of the HLA (short-range outbound track data). Arrows indicate the three ship-noise frequency lines used for inversion.

The estimated average SNR of the ship-noise data is given in Fig. 6.2. The SNR estimates, defined in Eq. 5.2, are based on an average of power spectral densities, after snapshot averaging, over the elements of the array and over five data segments. For the outbound track, the SNR varies from –1 dB to +5 dB for the three processed frequencies for the short-range data, while at long-range the SNR varies from –8 dB to 0 dB. For the short-range inbound-track data, the SNR varies from –3 dB to 0 dB. The lower SNR for these data compared to the outbound track data at similar range, and the fact that the frequency-to-frequency variation in SNR differs from that of the two outbound tracks, is assumed related to directionality of these ship-noise frequency components, with generally higher noise levels in the direction of the stern. Measurements for a larger merchant ship reported by Arveson and Vendittis (2000), and for a small research vessel

by Trevorrow, Vasiliev, and Vagle (2008) indicate similar directionality of ship noise at low frequencies.

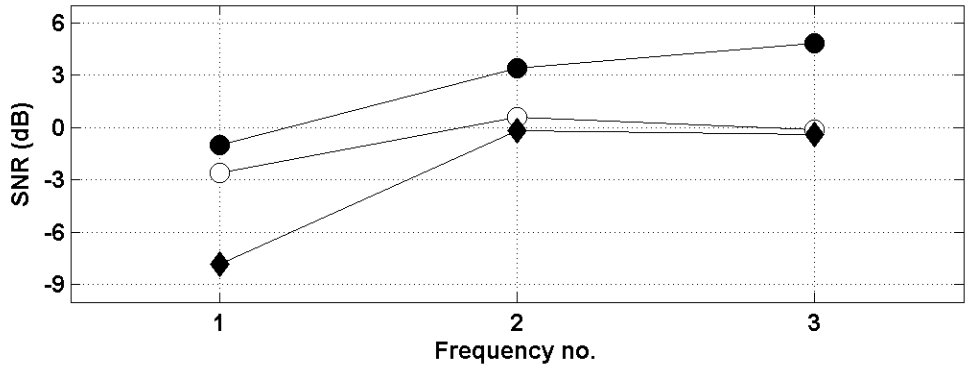

Figure 6.2: Average SNR for ship noise at three frequencies. The short-range outbound track, long-range outbound track, and short-range inbound track are indicated by closed circles, closed diamonds, and open circles, respectively.

The simple geoacoustic model (Chapter 2.3) consistent with the geophysical data was used in the inversions. The model (Fig. 2.3) consists of a water column of depth D with a known SSP over a two-layer seabed. The seabed model consists of an upper layer with depth-dependent properties over a homogeneous basement halfspace. In addition to the seven geoacoustic model parameters, small corrections to the nominal values of water depth (D), source range (r), source depth (z), and source bearing (b) were also included in the inversions (the latter three parameters are repeated for each data segment). The model parameters and the prior search bounds applied in the inversions are as given in Table 5.1, except for search bounds for dr and z, which were -0.1–0.1 km and 3–6 m, respectively.

The assumptions on the data error statistics (Chapter 3.9) were checked by performing *a posteriori* tests on data residuals (for each snapshot and data segment, given by the

difference between measured data and modelled data for the ML-model computed by minimizing Eq. 6.2). The KS test was applied to test for Gaussianity, with no evidence against the hypothesis of Gaussian-distributed errors at a 0.05 level of significance in 96% of test cases. The runs test provided no evidence against spatial randomness (i.e., between elements of the HLA) at a 0.05 level of significance in 98% of test cases. Tests for residual correlation over frequency and over time (i.e., between data segments) are not meaningful in this context due to the small number of samples (three and five, respectively) available for testing. However, with these small numbers of samples, the effect of potential error correlations is substantially reduced.

6.4. Inversion results

6.4.1. Multiple data segments

This section presents results from inversion of ship-noise data from the outbound track at ranges of 1.49–1.70 km and considers the effect of increasing data content, in the form of multiple data segments, in the inversion. Each data segment is represented by the CSDM from data averaged over a time interval of 18.2 s. Data segments are combined under the assumption of a range-independent environment. Replica acoustic fields were generated using the normal-mode propagation model ORCA, using a complex-plane mode search to account for possible near-field effects due to continuous modes. The normalized Bartlett mismatch was within 0.34–0.81 for these data. (These estimates were obtained by evaluating Eq. 6.3 for each data segment and frequency at the ML

model obtained by minimizing the data misfit function defined in Eq. 6.2. Note that this misfit function implicitly weights the data at each frequency according to its estimated uncertainty.)

Geoacoustic inversion results for the cases of one, two, and five data segments are shown in Fig. 6.3 in terms of marginal PPDs for the seven geoacoustic model parameters (Table 5.1), and the average sound speed in the upper sediment layer, c_{AVE}. In addition to the seven geoacoustic parameters and water depth, each inversion included three geometric parameters (source range, depth, and bearing) for each data segment (e.g., a total of 23 parameters for inversions with five data segments). First consider the results for a single data segment in the upper distributions of Fig. 6.3. The most sensitive parameters are those determining the sound speed profile in the seabed (defined by c_1, c_2, h). Densities and attenuations are relatively insensitive parameters with essentially flat distributions. However, even for the sensitive parameters, the marginal distributions are relatively wide, indicating limited ability to resolve the seabed sound-speed profile. By including two and five data segments in the inversions (middle and lower distributions in Fig. 6.3), the uncertainty distributions for the parameters defining the seabed sound-speed profile narrow significantly. This is further quantified in Fig. 6.4, where MDs for the three inversions are compared for each geoacoustic parameter. Reductions in MD by a factor of approximately two from one data segment to five data segments are observed for the sensitive parameters. For example, the mean deviation for the top sound speed c_1 is reduced from 50 m/s for one data segment to 40 m/s for two data segments, and to 23 m/s for five data segments. For sound speed c_2 in the lower layer, the MD is reduced from 111 m/s for one data segment to 43 m/s for five segments. The uncertainty of

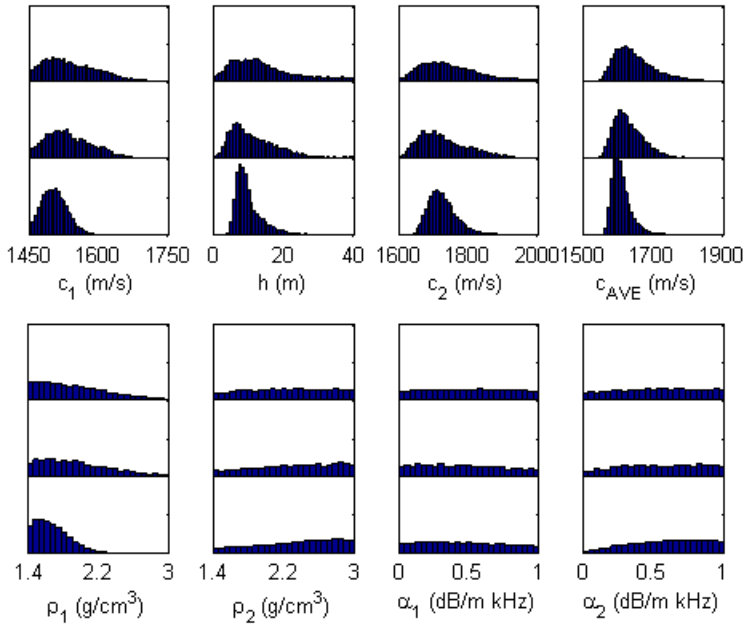

Figure 6.3: Marginal PPDs for different number of data segments included in inversion of ship-noise data: One segment (upper distributions), two segments (middle distributions), and five segments (lower distributions).

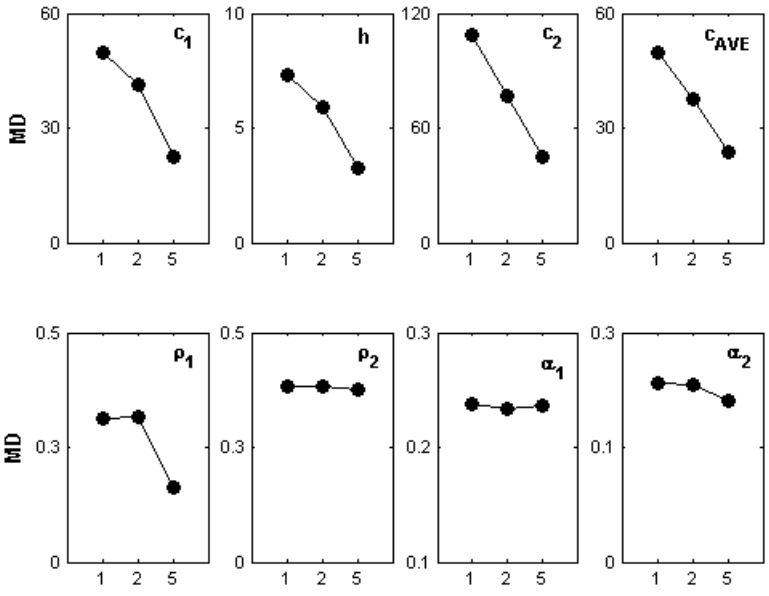

Figure 6.4: Posterior uncertainty estimates of geoacoustic parameters quantified in terms of mean absolute deviations for: 1, 2, and 5 data segments included in the inversions. Parameter units vary between plots and are given in Table 5.1.

upper-layer density ρ_1 is also reduced; however, for the five-segment case the marginal distribution for this parameter is significantly constrained by the lower *a priori* bound (Fig. 6.3), and hence the MD can underestimate the uncertainty. There is no significant reduction in MDs for the insensitive parameters α_1, α_2, and ρ_2.

6.4.2. Ship range and orientation

This section examines the effects of range and ship orientation on ship-noise geoacoustic inversion by considering additional data from the outbound track at 5.09–5.30 km range and from the inbound track at 1.46–1.67 km range. The normalized Bartlett mismatch was within 0.54–0.95 and 0.56–0.89 for these data, respectively. Geoacoustic inversion results for the two additional data sets are shown in Fig. 6.5 in terms of marginal PPDs for geoacoustic parameters, with results for the short-range outbound data included for reference (middle distributions). Five data segments are included in all inversions. Figure 6.5 shows that there is general consistency between the three results (i.e., the distributions have considerable overlap). The upper sound speed c_1 is reasonably well determined for the short-range inbound and long-range outbound data, although at lower resolution than for the short-range outbound data. However, distributions for h and c_2 (and c_{AVE}) are considerably wider; thus, the detailed structure of the sound-speed profile in the seabed is not well resolved by the long-range outbound and short-range inbound data. The distribution widths for c_1 and h are slightly narrower for the short-range inbound data than for the long-range outbound data. The mean and MD of c_1 from the short-range inbound and long-range outbound data are 1573±39 m/s and

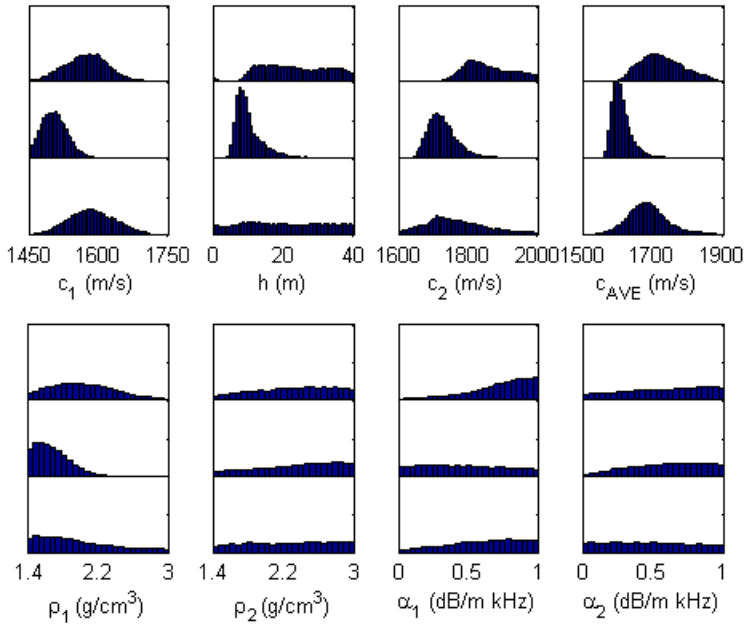

Figure 6.5: Marginal PPDs for short-range inbound (upper distributions), short-range outbound (middle distributions), and long-range outbound (lower distributions) ship-noise data.

1586±43 m/s, respectively, while the values for the short-range outbound data are 1507±23 m/s. The apparent shift to higher c_1 values can be interpreted as a consequence of a loss of resolution of the structure of the seabed sound speed profile (i.e., the distinction between upper and lower sound speeds becomes smeared).

The average SNR for the short-range inbound data is 2–5 dB lower than the short-range outbound data as shown in Fig. 6.2, likely due to directional effects (Chapter 6.3). This lower SNR could explain the poorer results for the inbound data when compared with the outbound data from similar range. The estimated SNR for the long-range outbound data is 4–7 dB lower than the short-range outbound data due to the loss of signal strength with range, since the ship orientation with respect to the HLA is unchanged. This decrease in SNR degrades the long-range inversion results, although modal attenuation likely also contributes to degraded results for this case (discussed in the following section).

6.4.3. Ship noise versus controlled-source inversions

This section compares results of inversion of ship-noise data from the outbound track with previous results from inversion of controlled-source data, and also with reference geophysical measurements. The SNR of the controlled-source data used in the inversions (five frequency components) varied from 9–15 dB (for both short-range and long-range data, since the source level was changed with range). Figures 6.6(a) and (b) show marginal PPDs for the parameters defining the seabed sound-speed profile for short-range controlled-source and ship-noise data, respectively. There is excellent agreement between the results obtained from the two data sets, but with wider distributions (increased uncertainty) for the ship-noise data. For both data sets, the detailed structure of the seabed sound-speed profile is well resolved.

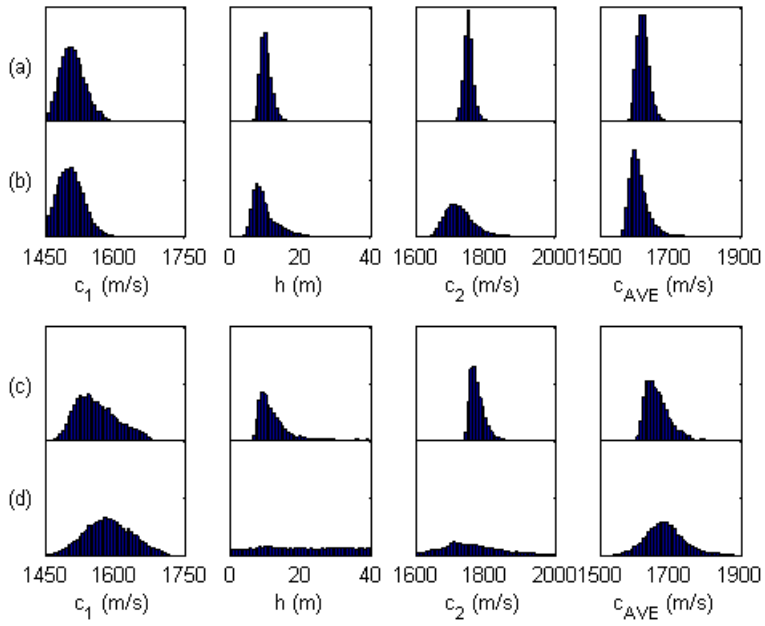

Figure 6.6: Marginal PPDs for: (a) Short-range outbound controlled-source data, (b) short-range outbound ship-noise data, (c) long-range outbound controlled-source data, and (d) long-range outbound ship-noise data.

Results are quantified in terms of parameter mean estimates with MD uncertainties in Table 6.1. Values for controlled-source and ship-noise data are, respectively, 11.2±1.4 and 11.2±3.1 m for h, 1510±21 and 1507±23 m/s for c_1, and 1753±13 and 1737±43 m/s for c_2. Table 6.1 also lists approximate values for these parameters obtained from reference geophysical measurements (h=10–20 m, c_1=1500–1520 m/s, and c_2=1745 m/s), which agree well with the geoacoustic inversion results.

Parameter and units	Ship Noise	Controlled source	Geophysical data
h (m)	11.2±3.1	11.2±1.4	10-20
c_1 (m/s)	1507±23	1510±21	1500-1520
c_2 (m/s)	1737±43	1753±13	1745
ρ_1 (g/cm^3)	1.69±0.16	2.03±0.20	2.0-2.1
ρ_2 (g/cm^3)	2.31±0.38	2.06±0.33	
α_1 (dB/m kHz)	0.49±0.23	0.32±0.18	
α_2 (dB/m kHz)	0.60±0.21	0.21±0.13	

Table 6.1: Geoacoustic parameter estimates (mean with mean-deviation uncertainties) from inversion of ship-noise and controlled-source data (Chapter 5) at range of 1.5 km (outbound track). Also included are approximate values from supporting geophysical measurements.

Figures 6.6(c) and (d) show geoacoustic inversion results for long-range controlled-source and ship-noise data, respectively. The seabed sound-speed profile parameters are reasonably well determined by the higher-SNR controlled-source data, while ship-noise data determine only c_1. Estimates for c_1 are 1559±37 m/s for controlled-source data and 1586±43 m/s for ship-noise data; in both cases these values are higher than for the corresponding short-range inversions.

The degradation in seabed resolution from the short- to long-range ship-noise data (Figs. 6.6(b) and (d)) is likely not due solely to decreased SNR. Some degradation is also

observed between the short- and long-range controlled-source data, Figs. 6.6(a) and (c), even thought the SNRs are almost identical for these data. In Chapter 5 the degradation for the controlled-source data was attributed to attenuation of higher-order modes. This has two possible effects: loss of resolution of deeper seabed structure (due to loss of information from modes propagating at higher grazing angles, hence with deeper bottom penetration), and loss of resolution of shallower structure (due to loss of information from the short vertical wavelengths of higher-order modes).

To further investigate the effects of SNR and range on seabed resolution, we consider inversions of synthetic ship-noise data. These data were generated for the model environment described in Chapter 2.3, with geoacoustic parameters taken to be the mean values for the controlled-source inversion (Table 6.1). Noise was represented by an error variance added to the main diagonal of the CSDM (Eq. 4.1) with variances (Eq. 4.2) representative of the misfit of the outbound ship-noise data. The results from inversion of short- and long-range synthetic data in Figs. 6.7(a) and (b) closely resemble those obtained from inversion of experimental ship-noise data in Figs. 6.6(b) and (d), although parameter distributions are slightly narrower for the synthetic data. Of note is the fact that the marginal distributions for c_1 for synthetic data appear shifted to higher values relative to the true value, and that the shift increases with range. To isolate the effect of range on inversion results, inversion of long-range synthetic data was repeated with the SNR equal to that of short-range (ship-noise) data. Results are presented in Fig. 6.7(c): the wider distributions for c_1, h and c_2, and the shift in c_1 to higher values when compared with Fig. 6.7(a) are due to the range effect; the further widening of distributions in Fig. 6.7(b) can be interpreted as an additional effect of lower SNR.

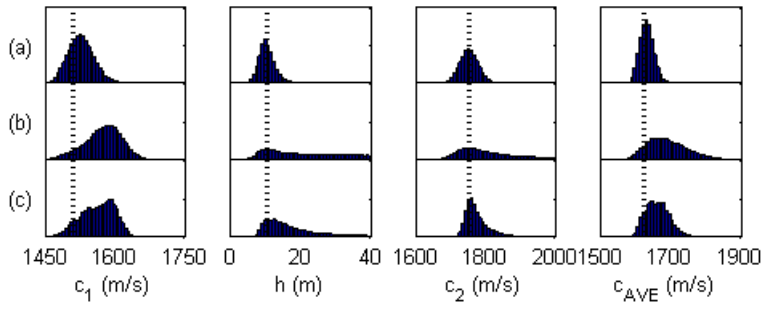

Figure 6.7: Marginal PPDs for: (a) Short-range synthetic ship-noise data, (b) long-range synthetic ship-noise data, and (c) long-range synthetic high-SNR ship-noise data. Vertical dashed lines indicate true parameter values.

6.4.4. Parameter interrelationships

Finally, it is of interest to examine inter-parameter correlations in ship-noise inversion. Figure 6.8 shows the correlation matrix for the short-range outbound ship-noise data. Since five data segments are included in the inversion, the model included 15 source parameters (five sets of b, z, and r). The positive correlations between layer thickness h and layer sound speeds c_1 and c_2 indicate that the data have limited ability to distinguish between models with thicker, faster layers and thinner, slower layers (since both can produce similar acoustic transit times through the layer). Correlations between geometric and geoacoustic parameters are in general small, with weak negative correlations between each range parameter r_j and sound speeds c_1 and c_2. Within the geometric parameters, there are positive correlations between range parameters and water depth D; this corresponds to a known environmental mismatch effect in MFP (Del Balzo, Feuillade, and Rowe, 1988), and was also obtained from inversion of controlled-source

data (Chapter 5). Finally, there are strong positive correlations between each of the range parameters r_j. This indicates that the range corrections in these inversions could likely be treated by a single offset parameter that applies to all source ranges, thus reducing the dimensionality of the inversion problem.

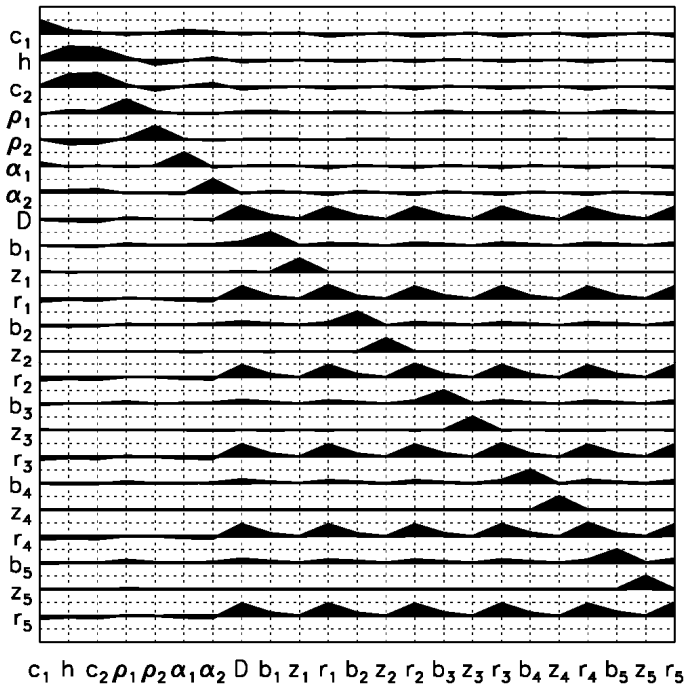

Figure 6.8: Parameter correlation matrix for short-range outbound ship-noise data.

Figure 6.9 shows joint marginal PPDs for selected combinations of parameters. The joint marginal distributions for the correlated parameters, specifically for h and c_1, h and c_2, and r_1 and D (similar results for each r_j and D) illustrate how the correlations increase parameter uncertainties. In the joint marginal distribution for h and c_1, two distinct modes of higher probability indicate strongly nonlinear behaviour: one indicating a weak negative correlation between the two parameters, while the other (weaker mode) indicates

a positive correlation between the two parameters. The net result is the weak positive correlation indicated in Fig. 6.8.

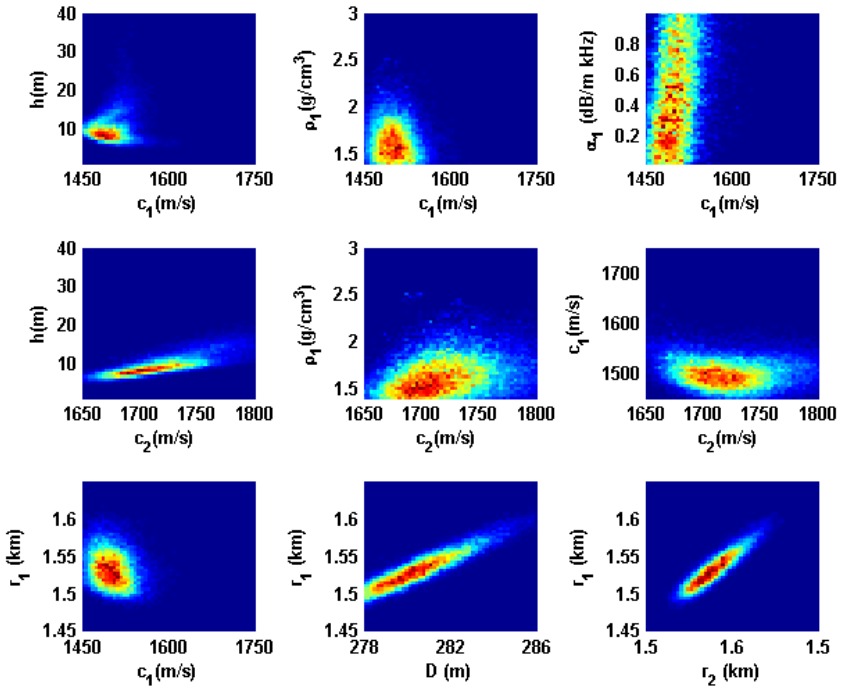

Figure 6.9: Selected joint marginal PPDs for short-range outbound ship-noise data.

6.5. Summary

This chapter examined geoacoustic inversion of narrowband ship-noise data collected at a bottom-moored HLA in shallow water. A Bayesian formulation was applied to quantify the information content of ship noise to resolve seabed parameters in terms of rigorous uncertainty distributions. A general problem with ship-noise data can be low SNR and relatively few suitable frequency components for processing. This problem was partially mitigated by combining multiple data segments in the inversions, leading to significantly reduced uncertainties of geoacoustic parameter estimates. Inversions using

multiple-segment ship-noise data were compared for three cases: inbound and outbound ship at short range, and outbound ship at long range. The SNR was highest for the short-range outbound data, and decreased with range and with change in the ship orientation presumably due to directional effects (i.e., higher SNR with ship stern and propeller toward the array). The short-range outbound ship noise provided the most informative inversion results, and resolved the seabed sound-speed profile (parameterized by an upper layer with a gradient over a homogeneous lower layer). The long-range outbound and short-range inbound data were unable to resolve the seabed sound-speed profile, likely due to the lower SNR, and, for the long-range data, attenuation of higher-order modes. The geoacoustic parameters estimated from the inversion of short-range outbound ship noise agree well with results from inversion of controlled-source data, and with reference geophysical measurements. The results presented in this chapter are for inversion of noise from a relatively quiet ship; results could differ for a different ship or environment, although the methods developed here should be applicable to other experiment situations.

Chapter 7 Three-dimensional source tracking in an uncertain environment via focalization

7.1. Introduction

This chapter develops an approach for 3D tracking of a moving acoustic source in an uncertain shallow-water environment with application to HLA data. The method makes use of data from multiple observations (source positions) along the track, the ASSA hybrid optimization algorithm (Dosso, Wilmut, and Lapinski, 2001), and the Viterbi algorithm (Viterbi, 1967) to determine the most probable source track within applied limits on source horizontal and vertical velocities. The approach is similar to the 2D focalization-tracking algorithm recently developed by Dosso and Wilmut (2009), but is extended here to 3D tracking with a HLA. The approach is applied to noisy synthetic data in a series of test cases that include different track geometries, varying SNRs, and varying levels of prior information on seabed and water-column parameters. The results are evaluated in terms of the probability of estimating a track that is acceptably close to the true track. The focalization-tracking algorithm is found to substantially outperform tracking with poor environmental estimates and in general obtains results close to those obtained with exact environmental knowledge. The method is also applied to data collected with a bottom-moored HLA (from the Barents Sea 03 experiment), including data due to a continuous-wave towed source and ship noise at several ranges. The work in this chapter has been published as Tollefsen and Dosso (2009).

7.2. Tracking algorithm

In this section, the 3D focalization-tracking algorithm is described. Several modifications to the original focalization algorithm of Collins and Kuperman (1991) have been implemented. First, focalization is extended to use of multiple data observations for a moving source. This increases the data information applied but also leads to a more challenging optimization problem since more unknowns (i.e., multiple source positions) are introduced. Second, following the approach of Fialkowski et al. (1997), source range and depth coordinates are not treated as explicit parameters, but are computed from the mismatch ambiguity surfaces generated for the environmental and bearing parameters of each model in the optimization. Third, an efficient tracking algorithm is applied to find the optimal source track through the set of ambiguity surfaces.

Consider acoustic data $\mathbf{d} = \{\mathbf{d}_{fj}, f=1,F; j=1,J\}$ at N sensors, F frequencies and J observations (data segments) for a moving source. The data mismatch is taken to be the negative log-likelihood function under the assumption of uncorrelated, complex Gaussian-distributed errors with unknown source amplitude and phase and unknown error variance at each frequency. This leads to mismatch E_j for the jth data segment given by

$$E_j(\mathbf{m}) = N\sum_{f=1}^{F} \log_e B_{fj}(\mathbf{m}), \tag{7.1}$$

and a total track mismatch of

$$E(\mathbf{m}) = \sum_{j=1}^{J} E_j(\mathbf{m}), \tag{7.2}$$

where $B_{ff}(\mathbf{m})$ is the Bartlett mismatch (defined in Eq. 6.3), and **m** is the model comprising unknown environmental and track parameters.

The search for a lowest-mismatch model is driven by the ASSA hybrid search algorithm, described in Chapter 3. The variation of source bearing (θ) with time is included in the inversion and is modelled by a second-order polynomial

$$\theta_j = b_0 + b_1 t_j + b_2 t_j^2, \tag{7.3}$$

where $t_j=(j\text{-}1)\Delta t$ is the observation time (Δt is a constant time increment), and (b_0, b_1, b_2) are unknown polynomial coefficients. The coefficients are included as parameters in the model **m**, with b_2 constrained to have the same sign as b_1 to avoid looping tracks. The use of higher-order polynomials could allow for closer fit to a larger number of track types; however, each polynomial coefficient introduces an additional parameter in the optimization and may complicate the search for simple-shaped (e.g., linear) tracks.

A key aspect of the tracking algorithm is that source range and depth along the track are not included as explicit parameters in the ASSA optimization, but are treated implicitly. For each model **m** considered in the optimization, the mismatch function (Eq. 7.1) is evaluated for each data segment at the range-depth grid of possible source positions (i.e., the ambiguity surface). The Viterbi algorithm is then applied to determine the lowest-mismatch range-depth track through this series of ambiguity surfaces, subject to constraints on maximum horizontal and vertical source velocities (of v_H and v_z, respectively). The Viterbi algorithm progresses as follows: for each grid point on the second surface, the sum of the mismatch at that point and the point of minimum mismatch on the first surface within a region limited to $\pm\sqrt{(v_H\Delta t)^2-(r\Delta\theta)^2}$ in range and $\pm v_z\Delta t$ in depth of the current position is computed and stored (where $\Delta\theta$ is the

difference in bearing and r is the grid-point range). The point on the first surface that produces the smallest mismatch sum is taken to be the antecedent to the grid point on the second surface; this is also stored. For each grid point of the third surface, the sum of the mismatch at that point and the point of minimum mismatch on the stored mismatch-sum surface within source velocity constraints is computed and stored. The point on the second surface that produces the smallest mismatch sum is taken to be the antecedent to the grid point on the third surface. This procedure is continued until the Jth surface has been examined. The minimum of the final mismatch-sum surface then defines the endpoint of the most probable track and the most probable track through all surfaces (satisfying source velocity constraints) is determined, since antecedents on all previous surfaces have been stored.

7.3. Numerical simulations

7.3.1. Test cases

An environmental model representative of the shallow continental shelf (Fig. 4.1) was chosen for the simulation study. The model consists of a water column of depth D and a seabed with a sediment layer of thickness h over a semi-infinite basement. Seabed geoacoustic parameters include sound speed at the top and bottom of the sediment layer (c_{1T} and c_{1B}), density (ρ_1) and attenuation (α_1) in the sediment, and sound speed (c_2), density (ρ_2), and attenuation (α_2) in the basement. The water-column SSP is described by two parameters (c_{w1} and c_{w2}) at depths of 0 and D m. Table 7.1 lists the true values for all

environmental parameters together with both wide and narrow search bounds applied in this study. The narrow bounds represent relatively small uncertainties as would typically result from carrying out a geoacoustic inversion survey and SSP measurements before tracking. The wide bounds represent an unknown environment with no such information available. In the first part of this study, wide search bounds are applied for the eight seabed geoacoustic parameters and water depth, and narrow search bounds for the SSP parameters.

Parameter and Units	True value	Wide bounds	Narrow bounds
Geoacoustic			
h (m)	12	[0, 40]	[11, 13]
c_{1T} (m/s)	1503	[1450, 1600]	[1494, 1512]
c_{1B} (m/s)	1560	[1500, 1650]	[1547, 1573]
c_2 (m/s)	1750	[1600, 1900]	[1670, 1830]
ρ_1 (g/cm^3)	1.50	[1.20, 2.00]	[1.36, 1.64]
ρ_2 (g/cm^3)	1.85	[1.40, 2.20]	[1.48, 1.82]
α_1 (dB/λ)	0.22	[0.01, 1.00]	[0.14 ,0.30]
α_2 (dB/λ)	0.12	[0.01, 1.00]	[0.01, 1.00]
D (m)	115	[113, 117]	[114.5, 115.5]
SSP			
c_{w1} (m/s) at 0 m	1472	[1465, 1480]	[1469, 1475]
c_{w2} (m/s) at D	1468	[1465, 1480]	[1465, 1471]
Bearing			
b_0 (º)		[-180, 180]	
b_1 (º/min)		[-9, 9]	
b_2 (º/min^2)		[0, 0.5]	

Table 7.1: Model parameters and search bounds used in tracking simulation study.

The test cases involve acoustic data at frequencies of 200 and 300 Hz received at a 256-m long HLA on the seafloor (oriented north-south). The array is comprised of 33

sensors equidistant spaced at 8-m intervals. This relatively sparse array (element spacing greater than one acoustic wavelength) was chosen to keep computational efforts reasonable given the large number of inversions considered in this study. Simulated data were generated for a source moving at 24-m depth at constant speed and course for three tracks, each consisting of nine data segments separated by 60 s in time. The tracks are plotted in Fig. 7.1 and include a source moving outbound at a speed of 3 m/s near array endfire at range 3.23–4.63 km (Track 1), a source moving at 4 m/s parallel to and towards the array broadside at range 3.23–1.84 km (Track 2), and a source moving across array endfire at 6 m/s at range 3.23–2.8 km (Track 3).

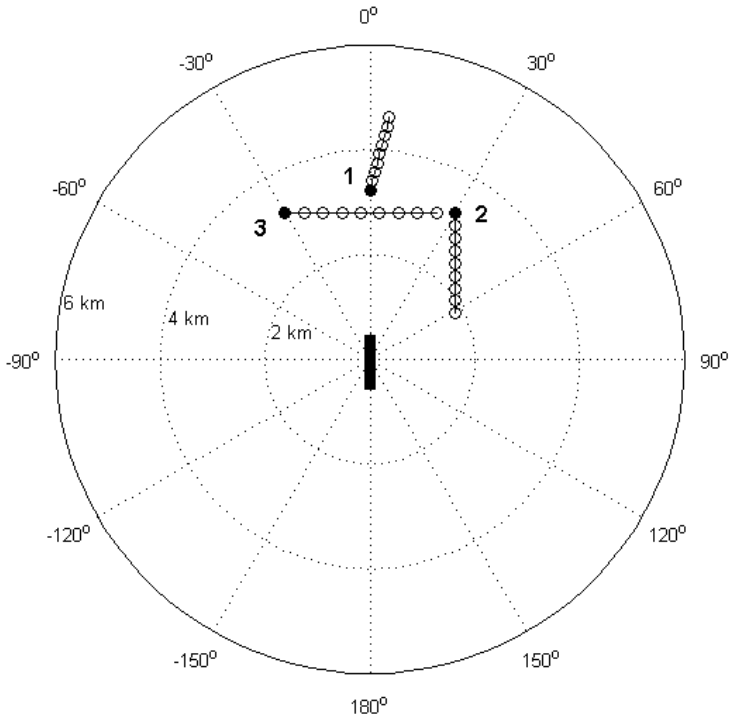

Figure 7.1: Tracks (1-3) used in simulation study. Start positions indicated with filled circles. Array (not to scale) is centered at the origin of the coordinate system.

The range-depth search grid defining the 2D ambiguity surfaces cover 0.3–6.0 km in range (grid spacing 50 m) and 4–112 m in depth (grid spacing 2 m). (Note that the grid points do not coincide exactly with track points in range.) Table 7.1 lists search limits for the bearing model parameters. Track constraints are imposed on the source horizontal and vertical velocities of 9 and 0.067 m/s, respectively.

To simulate noisy data, the data CSDM is here computed using synthetic acoustic fields (for the true environment) with noise added to the acoustic pressure vectors, i.e.,

$$\mathbf{C}_{fj} = (\mathbf{d}_{fj} + \sigma_f \mathbf{n}_{fj})(\mathbf{d}_{fj} + \sigma_f \mathbf{n}_{fj})^\dagger , \tag{7.4}$$

where $\mathbf{n}_{fj}$ is a random noise vector with elements drawn from a standard complex Gaussian distribution and σ_f^2 is the noise variance (a single data snapshot is used). Under the assumption of independent Gaussian errors, the noise variance corresponding to a specific SNR can be computed as

$$\sigma_f{}^2 = \left|\mathbf{d}_f\right|^2 10^{-\mathrm{SNR}_f/10} / N. \tag{7.5}$$

The SNR was set to a fixed value at the start of the track and adjusted with range to yield constant noise variance. The resulting variations of SNR over the tracks are displayed in Fig. 7.2.

The normal-mode numerical propagation model ORCA was used to compute synthetic data and replica acoustic pressure fields. The number of acoustic field computations required for each model $\mathbf{m}$ is $M \cdot N \cdot J$, where M is the number of range-depth grid points, and the factor J is required due to variation in grid to array element ranges with bearing (computed using the law of cosines). For the 33-element HLA, given ambiguity surface grid size, and nine data observations, 1.87×10^6 field computations are required per frequency.

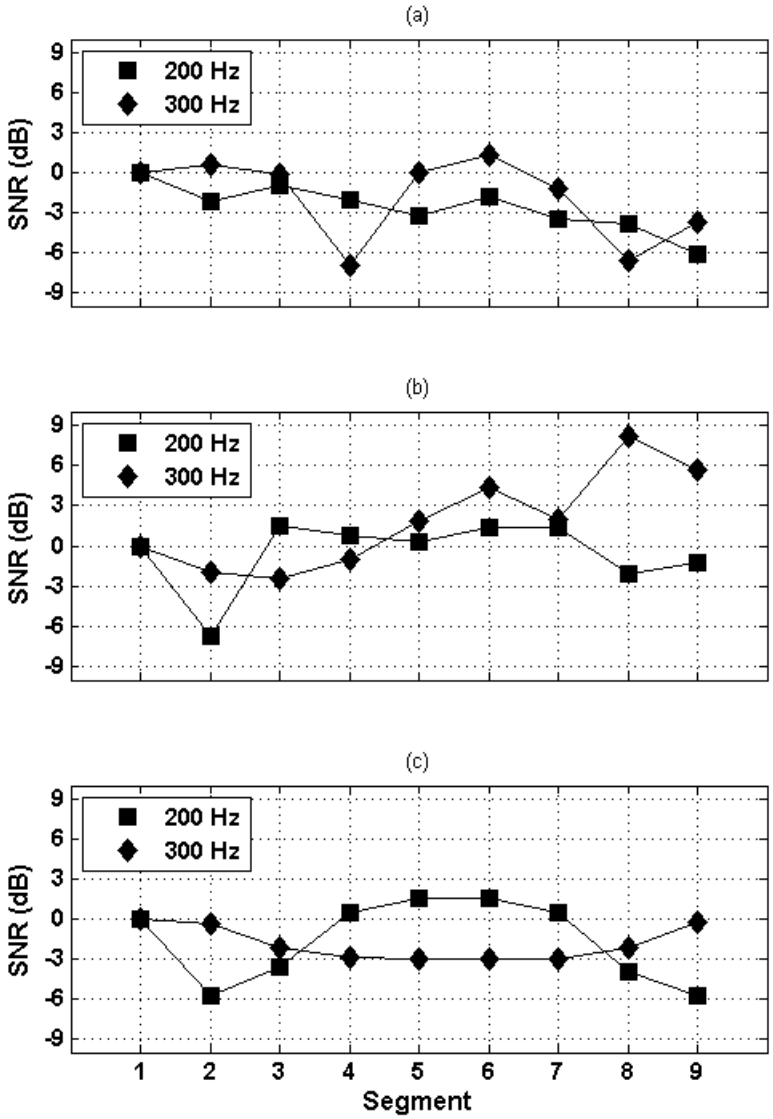

Figure 7.2: SNR versus track segment, relative to 0 dB at start of track, at 200 Hz (boxes) and 300 Hz (diamonds) for (a) Track 1, (b) Track 2, and (c) Track 3.

A preliminary study indicated that suitable ASSA control parameters for efficient track estimation consist of a temperature reduction factor β=0.95 with nine accepted perturbations required per temperature step, and a convergence threshold of 0.001.

Furthermore, the algorithm is terminated after six consecutive reductions in mismatch with unchanged track range and depth parameters.

A track estimate is considered to be acceptable if the mean position error is less than 600 m and the mean absolute depth error is less than 6 m. An error in track orientation with respect to the array length axis is not considered unacceptable since this results from the inherent inability of a HLA for left-right discrimination (i.e., if the track estimate reflected about the array axis satisfies the mean position and depth-error criteria, the result is considered acceptable).

7.3.2. Tracking results

To examine the ability to track sources in an uncertain environment with different levels of noise, the focalization-tracking algorithm was applied to 20 realizations of noisy data at SNR values from –6 dB to +6 dB (at the start of track). The results are compared with those obtained using the same 20 realizations of noisy data and either the *exact* environment or a *random* environment. For the exact case, the environmental parameters were fixed to their exact values and the bearing model parameters to the least-squares fit to the exact bearings (this represents the closest approximation to the true bearing for the given bearing parameterization). For the random case, the environmental parameters were fixed to random values drawn uniformly from within their search bounds. Results for the three tracks are summarised in Figs. 7.3–7.5 in terms of the probability of an acceptable track (PAT) vs average SNR (averaged in decibels over track segments and

frequencies), with one standard deviation error estimates computed for a binomial distribution according to (Bhattacharyya and Johnson, 1977)

$$\sigma_{\hat{p}} = \sqrt{\frac{\hat{p}(1-\hat{p})}{n}}, \tag{7.6}$$

where $\hat{p}$ is the fraction of acceptable track estimates in n trials.

Figures 7.3–7.5 show that PAT generally increases with increasing SNR for all tracking approaches. The PAT values obtained by focalization-tracking are generally much higher than those obtained for a random environment (except at the lowest SNRs) and in some cases approach the PAT for the exact model.

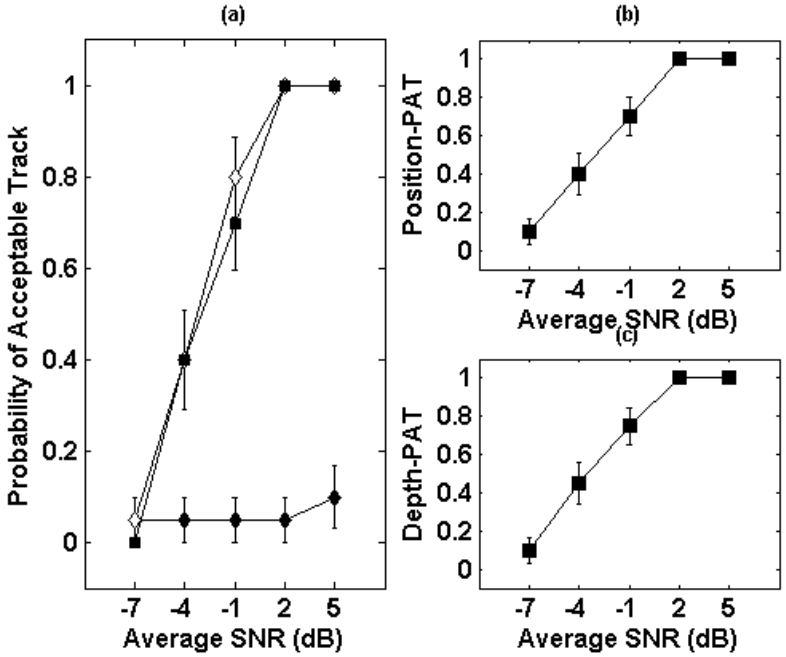

Figure 7.3: (a) PAT vs average SNR for Track 1 for: focalization in uncertain environment (squares), random environment (closed diamonds), and exact environment (open diamonds). Vertical lines indicate one standard deviation error bars. (b) PAT for position-error and (c) PAT for depth-error only for focalization in uncertain environment.

Figure 7.3 shows that for Track 1, the PAT for focalization is close to the exact-model PAT at all SNRs, and reaches 1.0 at +2-dB SNR. The good performance for this track can be understood since the ability of a HLA for estimation of environmental parameters and range-depth localization is highest for a source at endfire, where the effective vertical aperture of the array is maximized (Tolstoy, 1993). (Bearing resolution for a HLA is poorest at endfire; this can contribute to an increase in position error, but appears to be a less important effect in this case.) To further investigate the results, Figs. 7.3(b) and 7.3(c) show the PAT for position error only and for depth error only, which are quite similar for this track. Note that a track can be acceptable in position but not depth (or vice versa); for example, at –7-dB SNR the position-error and depth-error PAT values are both 0.1 while the position-and-depth PAT value is 0.

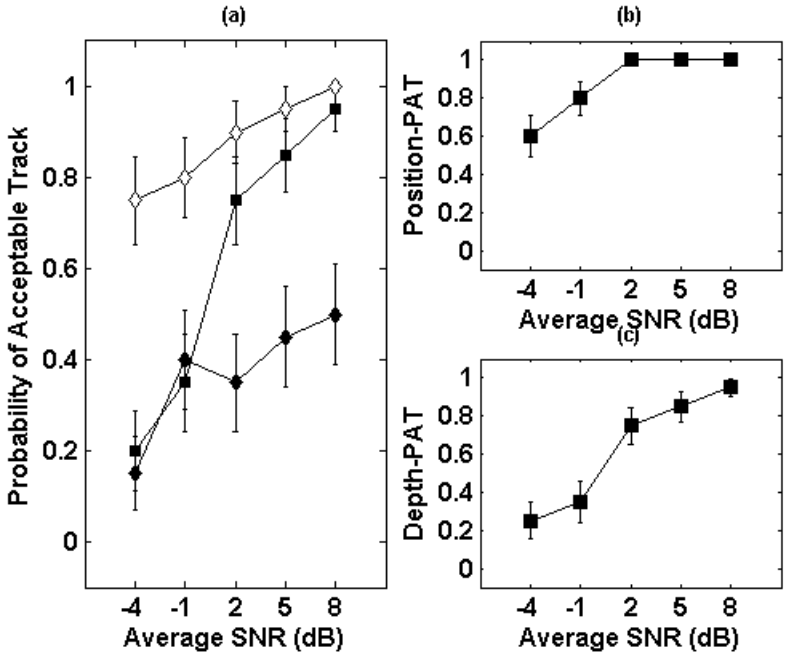

Figure 7.4: (a) PAT vs average SNR for Track 2 for: focalization in uncertain environment (squares), random environment (closed diamonds), and exact environment (open diamonds). Vertical lines indicate one standard deviation error bars. (b) PAT for position-error and (c) PAT for depth-error only for focalization in uncertain environment.

Figure 7.4 shows that for Track 2, the PAT for focalization at +2-dB SNR and above is close to that obtained for the exact model. At –4- and –1-dB SNR, the PAT for focalization is significantly lower than for the exact model. As the source moves towards array broadside, the effective vertical aperture of the array diminishes, and matched-field range and depth localization degrades. This degradation of localization in range can in part be offset by the ability for ranging by sampling wavefront curvature; this effect is most prominent for a source close to array broadside and at close source-receiver ranges. In addition, the bearing resolution for a HLA in general improves as the source moves towards array broadside. Figures 7.4(b) and 7.4(c) show that the position-error PAT is higher than the depth-error PAT at all SNRs, indicating that depth error is a more important cause of degraded track estimation for this track.

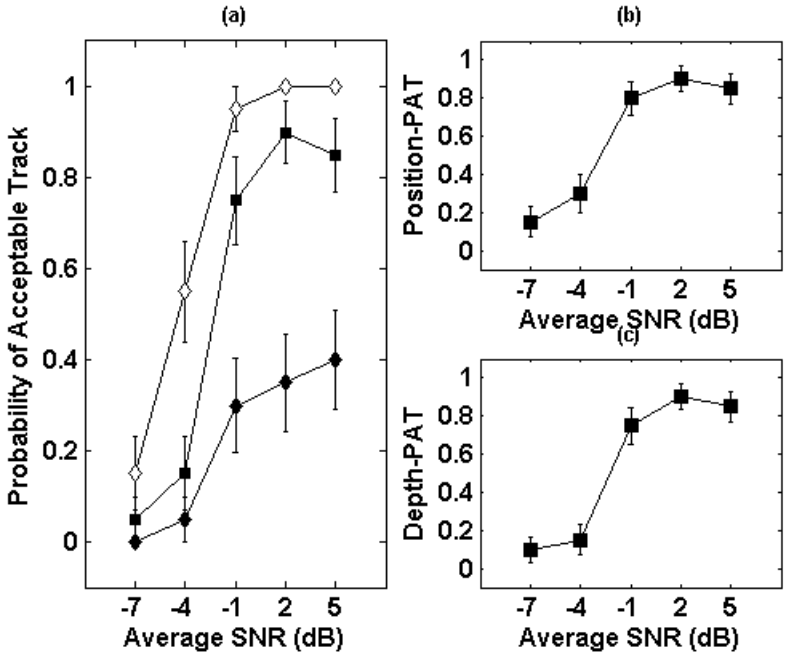

Figure 7.5: (a) PAT vs average SNR for Track 3 for: focalization in uncertain environment (squares), random environment (closed diamonds), and exact environment (open diamonds). Vertical lines indicate one standard deviation error bars. (b) PAT for position-error and (c) PAT for depth-error only for focalization in uncertain environment.

Figure 7.5 shows that for Track 3, the PAT for focalization increases with SNR but does not reach that obtained for the exact model. Overall, Figs. 7.3–7.5 show that the best tracking results are obtained for the two tracks near array endfire, with better results for Track 1 than for Track 3. Results are overall slightly poorer for Track 2 which approaches the array broadside.

To further illustrate results of the focalization-tracking algorithm, typical examples of acceptable and unacceptable tracks obtained via focalization are presented in Figs. 7.6–7.8. In Fig. 7.6 (Track 1 at –1-dB average SNR), the acceptable track has excellent depth estimates and is roughly linear except for the track end point, but is headed in a north-west (rather than north-east) direction; this is an example of the left-right ambiguity about the HLA. The deviation at the end of the track is related to the fact that endpoints are subject to one-sided track constraints only. The unacceptable track is at wrong depth and does not predict outward motion; however, the bearings are approximately correct.

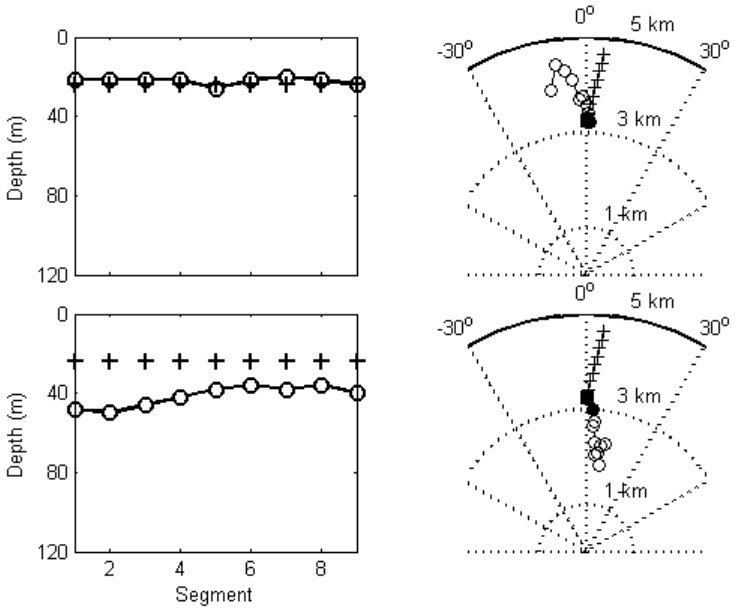

Figure 7.6: Examples of acceptable (upper panels) and unacceptable (lower panels) track estimates for Track 1 at –1-dB average SNR. Symbols indicate true (+) and estimated (○) coordinates. Start points indicated with filled symbols**.**

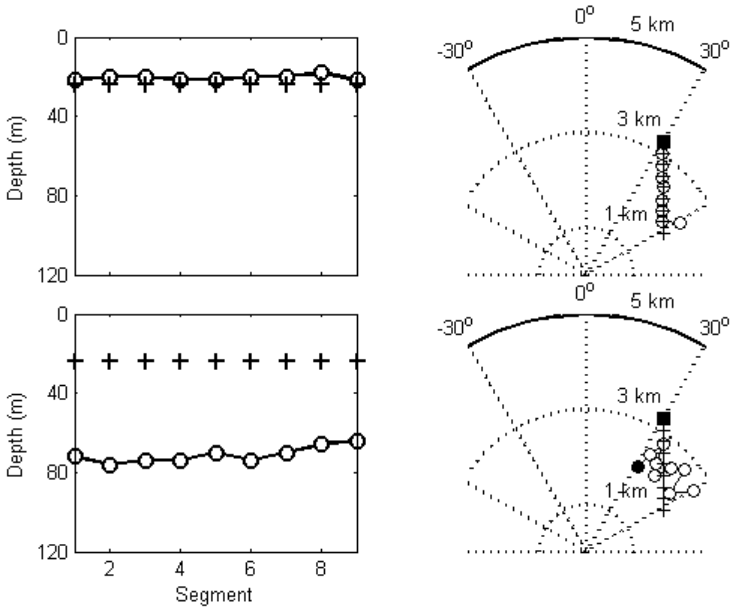

Figure 7.7: Examples of acceptable (upper panels) and unacceptable (lower panels) track estimates for Track 2 at +2-dB average SNR. Symbols indicate true (+) and estimated (○) coordinates. Start points indicated with filled symbols.

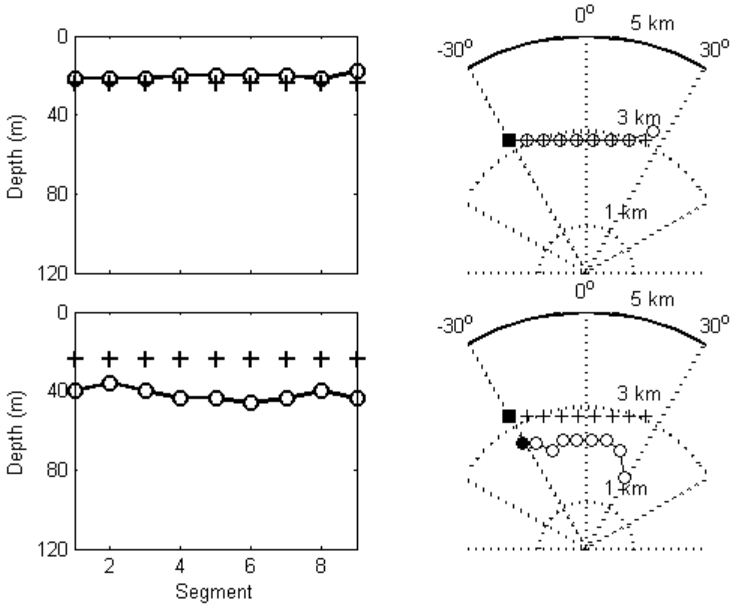

Figure 7.8: Examples of acceptable (upper panels) and unacceptable (lower panels) track estimates for Track 3 at –1-dB average SNR. Symbols indicate true (+) and estimated (○) coordinates. Start points indicated with filled symbols.

In Fig. 7.7 (Track 2 at +2-dB SNR), the acceptable track closely matches the true track except for an end point deviation, and is representative of all of the acceptable cases for this track. The unacceptable track has large depth errors and is unacceptable in position, although range and bearing errors are small. In Fig. 7.8 (Track 3 at +2-dB SNR), the acceptable track closely matches the true track. The unacceptable track is approximately 20 m deeper and at approximately 600 m shorter range than the true track (both position and depth errors above the threshold), but the bearing estimates are good and the track direction is correct.

7.3.3. Environmental model parameter estimates

The primary goal of focalization is localization/tracking, not recovery of environmental parameters. However, it is interesting to investigate to what extent the true environmental parameters can be determined given data information from multiple positions along a track. Figure 7.9 shows scatter plots of the parameter values of the lowest-mismatch models from each of the 20 runs of the focalization-tracking algorithm for combinations of six of the most sensitive environmental parameters for Track 1 at –1- and +5-dB average SNR (results for both acceptable and unacceptable tracks are included). In general, parameter estimates appear widely scattered within their search bounds with values that differ significantly from the true values, although some observations can be made. The spread of estimated values is larger at –1 dB than +5 dB. Estimates of sediment sound speed (c_{1T}, c_{1B}) tend to be aligned along a line with negative slope (tighter alignment at +5 dB than –1 dB), indicating weak negative correlation. This

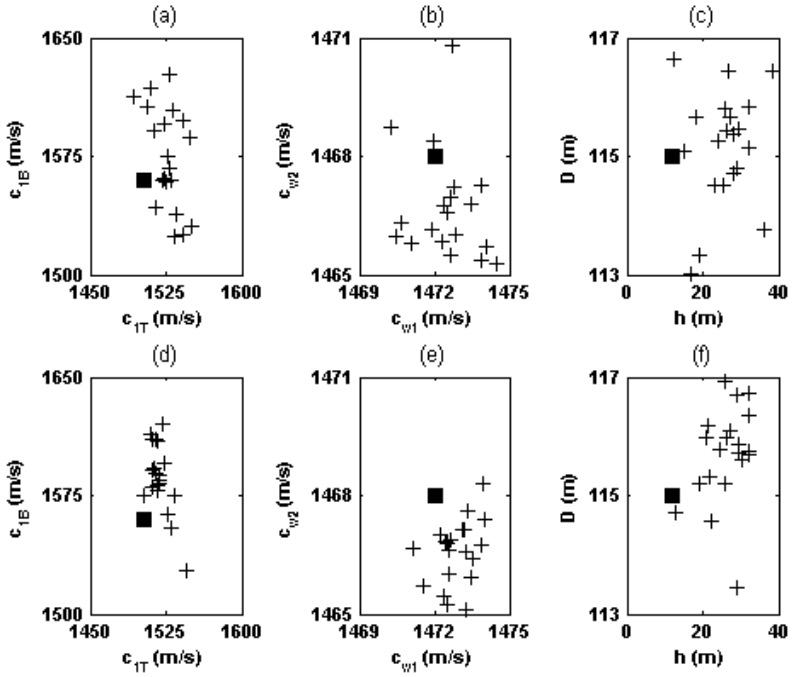

Figure 7.9: Scatter plots of lowest-mismatch model values for selected geoacoustic parameters. Track 1 at (a)–(c) –1-dB, and (d)–(f) +5-dB average SNR. True model values indicated with boxes.

correlation suggests that the data are sensitive to the average sound speed in sediment, but have limited ability to resolve these parameters individually. At +5 dB, the estimates of sound speed in water (c_{w1}, c_{w2}) tend to be aligned along a line with positive slope; this suggests that the data are more sensitive to the shape of the SSP than to the average sound speed. Similar inter-parameter correlations have been observed previously in geoacoustic inversion (e.g., Collins, Kuperman, and Schmidt, 1992; Dosso, Wilmut, and Lapinski, 2001; Dosso and Wilmut, 2008). Estimates of sediment thickness (h) and water depth (D) tend to be higher than their true values. Overall, it appears that the environmental parameters are not well determined individually but provide effective environments that allow for correct track estimation.

7.3.4. Effects of prior environmental uncertainty

This section examines and quantifies the dependence of track estimation on prior information of environmental parameters (e.g., whether the parameters are essentially completely unknown, or whether previous measurements, with uncertainties, exist). The tracking examples so far have used wide search bounds on geoacoustic parameters and water depth, and narrow search bounds on water sound speed as given in Table 7.1. This section also considers narrow or wide bounds on geoacoustic parameters and water depth in combination with narrow or wide bounds on water sound speed (Tracks 1 and 2 are considered). The narrow geoacoustic bounds correspond to the 95% HPD credibility intervals obtained in a simulated MFI experiment in this environment (Fig. 4.3(c)).

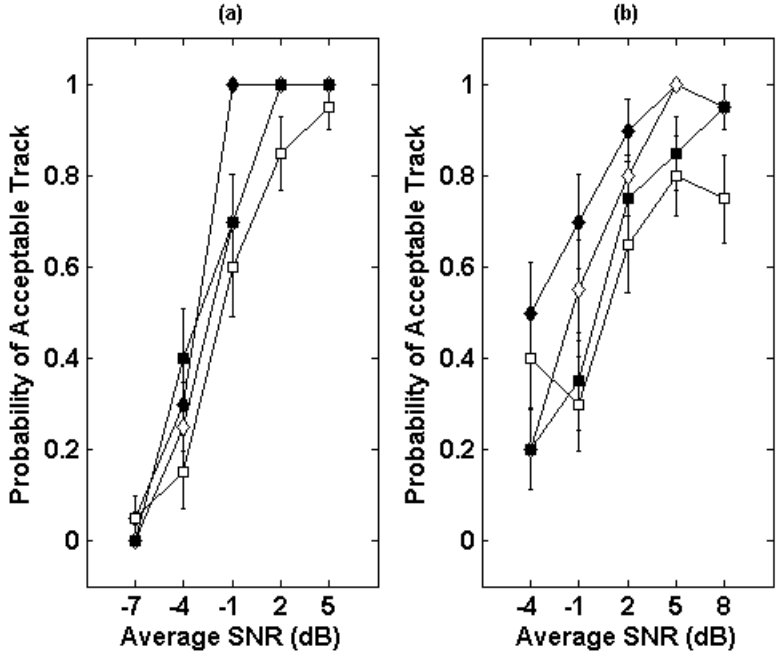

Figure 7.10: PAT vs average SNR for (a) Track 1 and (b) Track 2, for varying search bounds on geoacoustic/SSP parameters: narrow/narrow (closed diamonds), wide/narrow (closed boxes), narrow/wide (open diamonds), and wide/wide (open boxes). Vertical lines indicate one standard deviation error bars.

Figure 7.10(a) shows that for Track 1 the results obtained for wide geoacoustic/wide SSP bounds are consistently the poorest (except at the lowest SNR). Generally similar results are obtained for the other three cases (except at –1-dB SNR, where the narrow geoacoustic/narrow SSP result is significantly better). Note that narrow geoacoustic bounds allow for wide SSP bounds without significant degradation of results obtained for narrow geoacoustic/narrow SSP bounds. Figure 7.10(b) shows that for Track 2, the results obtained for narrow geoacoustic/narrow SSP bounds are significantly better than those obtained for wide geoacoustic/narrow SSP bounds. Results for narrow geoacoustic/wide SSP bounds are generally better than results for wide geoacoustic/ narrow SSP bounds. Results for wide geoacoustic/wide SSP bounds are poorest.

These results indicate that improved prior information on environmental parameters can have an important effect on tracking performance, particularly for tracks extending towards HLA broadside, where the data have reduced ability to resolve environmental parameters. The results also indicate that (for this environment) use of narrow bounds for geoacoustic parameters allows for wide bounds on SSP parameters without significant degradation of tracking performance.

7.4. Experimental source tracking results

This section presents results from application of the 3D focalization-tracking algorithm to selected experimental data from the Barents Sea 03 data set (Chapter 2). The acoustic data considered here were due to a continuous-wave tone emitted by the towed acoustic source at a frequency of 80 Hz for source-to-array (closest end) ranges of 4.0–4.7 km and

7.8–8.5 km (referred to as short-range and long-range towed-source data, respectively). In addition, ship noise at a frequency component of 144 Hz from ship-to-array ranges of 1.6–2.3 km and 5.1–5.8 km (referred to as short-range and long-range ship noise, respectively) is considered. The 3D focalization-tracking algorithm has also been applied to noise from a large merchant ship-of-opportunity in the Barents Sea, as reported in Tollefsen and Dosso (2008b).

The processing sequences for the towed source (ship-noise) data consisted of forming CSDM estimates from five (ten) consecutive 50% overlapping data snapshots of length 6.6 s (3.3 s), converted to the frequency domain using a fast Fourier transform with a frequency bin width of 0.15 Hz (0.3 Hz), with a Hamming time windowing function applied. The total averaging time for each data segment was 19.8 s (18.2 s). Nine data segments, separated by 33 s between the start of each segment, are used in tracking; these extended over a time span of 4 min 42 s over which the ship moved approximately 755 m. The average SNR for the towed-source data was estimated to be 3.3 dB (short-range) and 0.2 dB (long-range), and for the ship noise 4.5 dB (short-range) and –0.5 dB (long-range). The estimates are based on an average of (snapshot-averaged) signal and noise power spectral densities, averaged over the elements of the array and over the data segments.

The model environment (Chapter 2) consists of a water column with a known SSP over a two-layer seabed. The unknown environmental model parameters (seven seabed geoacoustic model parameters and water depth) and the search bounds employed are listed in Table 5.1. The range-depth ambiguity surfaces covered 8 km in range (1–9 km for short-range and 4–12 km for long-range data, grid spacing 50 m), and almost the

entire water column in depth (6–270 m, grid spacing 2 m). A second-order polynomial was used to model track bearing, with search bounds for bearing parameters set as listed in Table 7.1. Track constraints were imposed on source horizontal and vertical velocity of 6 and 0.067 m/s, respectively.

To assess the focalization-tracking algorithm developed in Chapter 7.2 for source tracking in an uncertain environment, four alternative (simpler) approaches to track estimation are also applied here to the measured data. In *independent focalization* (referred to as case 1pp) focalization is applied independently for each data segment, with no model applied for track bearing. The track is constructed as the sequence formed by the lowest-mismatch source range, depth, and bearing coordinates from each focalization, with no constraints applied on source velocity. In *simultaneous focalization*, data from all segments are inverted simultaneously, with the polynomial model (Eq. 7.3) applied for track bearing. For each model evaluated in the optimization, the minimum of each ambiguity surface is taken as the track segment range-depth coordinates. The final track is constructed as the sequence of range-depth minima, with no constraints applied on source velocity (case 9pp), or by application of the Viterbi algorithm to the final set of ambiguity surfaces with constraints applied on source velocity (case 9pv). These approaches are compared to results for the 3D focalization-tracking algorithm described in Chapter 7.2 (case 9vv), and for a *random environment* (case 9rv) in which the 3D focalization-tracking algorithm is applied with environmental parameters fixed to values drawn randomly from the uniform search bounds (results represent averages over 100 runs with different environment realizations).

Tracking results are summarized (Fig. 7.11) in terms of mean track position error and mean track depth error for the five approaches. Track errors are measured with respect to the measured source position for the towed-source data or ship stern position for ship noise, and with respect to the source tow depth or ship propeller depth. Uncertainty in the measured positions and depths, due to factors such as variations in ship speed, ship vertical motion, and uncertainty in estimated array position, have not been rigorously assessed, but can be assumed to on the order of 50 m and 2 m, respectively.

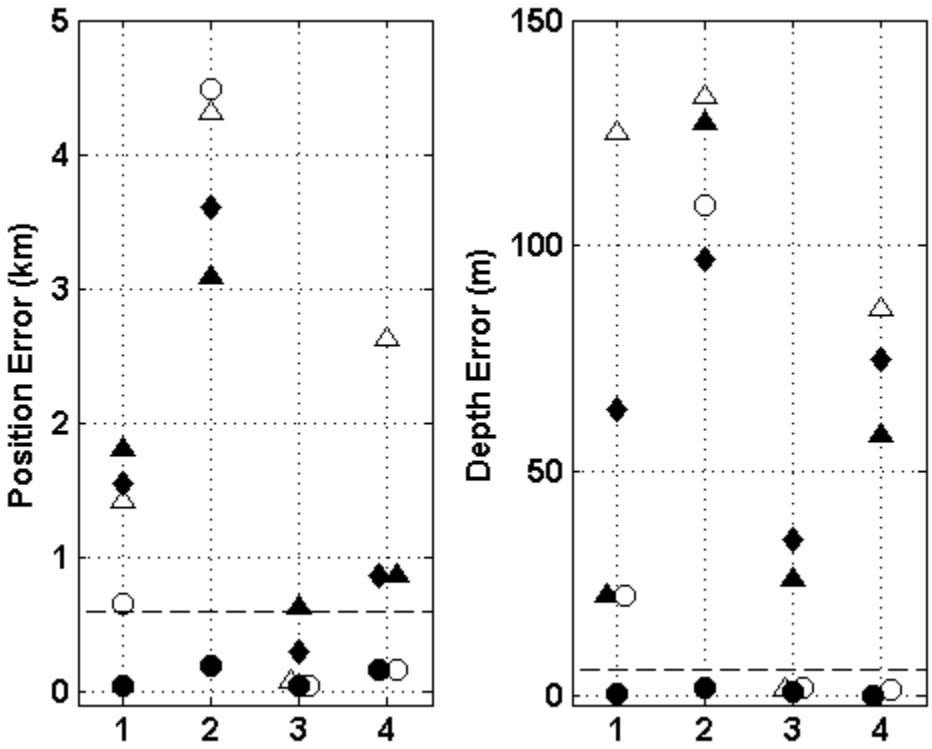

Figure 7.11: 3D tracking results for Barents Sea data. 1– towed-source data at range 4.0–4.7 km, 2– towed-source data at range 7.8–8.5 km, 3– ship noise at range 1.6–2.3 km, and 4– ship noise at range 5.1–5.8 km. Algorithms applied (described in the text) are: 1pp–open triangles, 9pp–closed triangles, 9pv–open circles, 9vv–closed circles, and 9rv–diamonds. Dashed lines indicate 600 m mean position error and 6 m mean depth error, defining an acceptable track.

Figure 7.11 shows that the focalization-tracking algorithm provides acceptable track estimates for all cases. For the towed-source data, only the 3D focalization-tracking algorithm (9vv) estimates an acceptable source track, with a mean position error of 36 m at short range and 200 m at long range (mean depth error <2 m in both cases). All other algorithms provide large range and depth errors. For ship noise, the 3D focalization-tracking algorithm estimates an acceptable track with mean position errors <100 m at short range and <200 m at long range (mean depth error <2 m in both cases). At short range, 1pp and 9pv also estimate tracks with small position and depth errors. At long range, 9pv also estimates an acceptable track, but the other algorithms do not. These results indicate that simultaneous environmental optimization and tracking with source velocity constraints are required for reliable source-track estimation for this experiment.

7.5. Summary

This chapter developed an approach to 3D source tracking with a HLA in an unknown ocean environment. The approach is based on ASSA optimization for unknown environmental and bearing model parameters and applies the Viterbi algorithm (with source velocity constraints) for range-depth track estimation. The algorithm was applied to synthetic data in a simulated environment for several linear source-track test cases. In general, the algorithm performance increased with SNR and in many cases approached the results obtained with exact environmental knowledge. The algorithm consistently outperformed tracking with an environmental model selected at random from the prior uncertainty bounds. Best tracking results were obtained for tracks near array endfire,

with some degradation for a track that approached the array broadside. Improved prior information on the environmental parameters, in the form of narrowed parameter search bounds, was shown to improve tracking performance, with largest impact for a track extending towards HLA broadside, and best results achieved with narrow bounds on both seabed geoacoustic and water sound-speed parameters. Results also indicated that, for the environment studied, use of narrow bounds for geoacoustic parameters allows for wide bounds on SSP parameters without significant degradation of tracking performance. Finally, the algorithm was applied to relatively low-SNR narrowband data from a towed submerged source and noise from a surface ship recorded on a bottom-moored HLA in a shallow water environment (Barents Sea). The 3D focalization-tracking algorithm successfully estimated the tracks of the source and ship and substantially outperformed alternative simpler algorithms that either did not make use of multiple data segments simultaneously, did not optimize over environmental parameters, or did not apply source velocity constraints via the Viterbi algorithm.

Chapter 8 Three-dimensional source tracking in an uncertain environment via marginalization

8.1. Introduction

This chapter develops a Bayesian marginalization approach for 3D source tracking in an uncertain shallow-water environment with application to HLA data. The idea is to formulate a joint inversion over unknown source locations (range, depth, and bearing) and unknown environmental properties, then integrate (marginalize) over the environmental parameters to obtain joint marginal probability distributions over source coordinates. The goal is to quantify uncertainty in source position/track estimates (due to data and model uncertainties), and to increase robustness of source tracking to environmental uncertainty. The approach developed here builds on the 2D marginalization-tracking algorithm recently developed by Dosso and Wilmut (2008).

Marginalization approaches to source localization in an uncertain environment have been based on integrating the PPD over uncertain environmental (nuisance) parameters to produce joint marginal probability distributions over source range and depth coordinates (Richardson and Nolte, 1991; Shorey, Nolte, and Krolik, 1994; Dosso, 2003; Dosso and Wilmut, 2007; Huang, Gerstoft, and Hodgkiss, 2009). The joint distributions are used to define the most probable source location and to quantify uncertainty in localization. The integration can be performed either by an average over a fixed number of samples drawn from prior distributions (e.g., Richardson and Nolte, 1991; Huang, Gerstoft, and Hodgkiss, 2009) or by sampling directly from the PPD via Markov-chain Monte Carlo

methods (Dosso and Wilmut, 2007, 2008). Richardson and Nolte (1991) used uniform prior distributions, while Huang, Gerstoft, and Hodgkiss (2009) used samples from the PPD of a preceding geoacoustic inversion experiment as priors for environmental parameters. The approach of Dosso and Wilmut (2007, 2008) samples from the PPD and inverts jointly for source locations and unknown environmental parameters. Bayesian source localization has been extended to Bayesian source tracking in an uncertain environment (Tantum and Nolte, 1998; Dosso and Wilmut, 2008), for consecutive data observations and with prior constraints on source motion applied. Applications to experimental data include source localization (Shorey and Nolte, 1998; Dosso and Wilmut, 2007) and tracking (Tantum et al., 2002) with data from a VLA in shallow water.

8.2. Method

The marginalization approach follows the Bayesian theory outlined in Chapter 3. To define the data mismatch, consider acoustic data $\mathbf{d} = \{\mathbf{d}_{fj}, f=1, F; j=1, J\}$ at N sensors, F frequencies and J observations (data segments) for a moving source. The data mismatch is taken to be the negative log-likelihood function under the assumption of uncorrelated, complex Gaussian-distributed errors with unknown source amplitude and phase and unknown error variance. This leads to mismatch given by

$$E(\mathbf{m}) = N \sum_{j=1}^{J} \sum_{f=1}^{F} \log_e B_{fj}(\mathbf{m}), \tag{8.1}$$

where $B_{fj}(\mathbf{m})$ is the Bartlett mismatch (for snapshot-averaged data) at the fth frequency and the jth data segment (Eq. 6.3), and $\mathbf{m}$ is the model comprising environmental and

source position (track) parameters. Track bearing is modelled by a second-order polynomial,

$$\theta_j = b_0 + b_1 t_j + b_2 t_j^2, \tag{8.2}$$

where $t_j=(j\text{-}1)\Delta t$ is the observation time (Δt is a constant time increment), and (b_0, b_1, b_2) are unknown polynomial coefficients. The coefficients are included as parameters in the model **m**, with b_2 constrained to have the same sign as b_1 to avoid looping tracks.

Marginalization consists of integrating the PPD over all unknown environmental (nuisance) parameters to obtain a set of joint marginal distributions for source coordinates, referred to as probability ambiguity surfaces (PASs). The PPD sampling applied here follows the development of Dosso and Wilmut (2008), and is carried out via a combination of Metropolis-Hastings sampling of environmental and bearing model parameters and 2D Gibbs (heat-bath) sampling of range and depth coordinates. Track constraints are applied as prior information on maximum horizontal and vertical source velocity. Marginal PPDs (Eqs. 3.10 and 3.11) are derived for source coordinates.

Several techniques (described in detail in Chapter 3.5–3.6) are applied for increased sampling efficiency. This includes drawing parameter perturbations from adaptively scaled Cauchy distributions in rotated coordinates (proposal distributions), with the initial proposal distribution based on the model covariance matrix for a linearized approximation to the PPD evaluated at the MAP starting model. Sampling is initiated at the MAP model obtained via the focalization-tracking algorithm developed in Chapter 7. In a *burn-in* phase, the initial estimate of the model parameter covariance matrix is periodically updated with a nonlinear estimate $\mathbf{C_m}$ (via Eq. 3.8) based on samples collected to that point; this phase continues until the maximum difference between the

correlation matrices for two samples collected in parallel is less than a threshold. The samples collected during burn-in are subsequently discarded; PPD sampling then continues (with $\mathbf{C_m}$ updated) until PAS convergence at a predefined threshold (defined below). PASs are computed for the environmental and bearing parameters of each sample at a fixed grid of source ranges and depths. Summing un-normalized PASs for each data segment over the sampling process, then normalizing yields marginal probability distributions over source range and depth.

The application of track constraints provides strong prior information but also significantly increases the difficulty in sampling the PPD. To ensure complete sampling of the parameter space, sampling at non-unity temperature is employed (Chapter 3.8). PAS convergence is evaluated by the Bhattacharyya coefficient (Bhattacharyya, 1943)

$$B_j = \sum_{k,l} \sqrt{P_{j1}(r_k, z_l) \cdot P_{j2}(r_k, z_l)} \tag{8.3}$$

with P_{j1} and P_{j2} representing the accumulated normalized PAS at coordinate (r_k,z_l) for surface j of the two samples collected in parallel, with the summation extending over the entire surfaces. A value of $B>0.85$ is required (for all surfaces) for convergence.

After convergence, the Viterbi algorithm is applied, in two steps, to determine the most probable track in range, depth, and bearing. First, the range-depth track is computed by application of the (2D) Viterbi algorithm to the range-depth PASs, with constraints on source velocity applied. Approximate bearings (required to compute horizontal velocity) are, for simplicity, taken from the MAP model. (The MAP model has, for the cases studied, yielded a reasonably good approximation to the true track bearing, but may yield inaccurate estimates of range and depth.) Second, track bearing is estimated by application of the (1D) Viterbi algorithm to the marginal distributions for

bearing for each source position (obtained for each sample via Eq. 8.2). Constraints on source velocity are applied, with ranges taken from the range-depth track estimate. Bearing is restricted to be either monotonically increasing or decreasing, to avoid looping tracks. The 3D track thus estimated is referred to as the Viterbi track in the following.

8.3. Numerical simulations

8.3.1. Test cases

The synthetic tracking examples considered here involve a HLA (33-sensor, 256-m length) at the seabed, and a source moving at 24-m depth along the endfire track (Track 1) and the towards-broadside track (Track 2) defined in Chapter 7.3. Two environments are considered: (i) a Mediterranean environment with a strong negative gradient in the water-column SSP and a seabed with sediment sound speed less than water sound speed (Dosso and Wilmut, 2008), and (ii) the continental shelf environment with a weakly negative gradient in the SSP and a seabed with sediment sound speed higher than water sound speed (Chapter 7.3). To simulate noisy data, the data CSDM is computed using synthetic acoustic fields for the true environment, with Gaussian-distributed random noise added to the acoustic pressure vectors using the procedure described in Chapter 7.3. Nominal SNR (dB-average along the array) vs. track segment is plotted in Figs. 8.1(a) and 8.1(b) for the Mediterranean environment and in Figs. 7.2(a) and 7.2(b) for the continental shelf environment. Table 8.1 lists the true values and bounds of uniform priors applied for environmental parameters of the Mediterranean environment.

Parameter and Units	True value	Search bounds
h (m)	9	[0, 30]
c_1 (m/s)	1495	[1450, 1600]
c_2 (m/s)	1530	[1500, 1650]
ρ_1 (g/cm³)	1.40	[1.00, 1.70]
ρ_2 (g/cm³)	1.60	[1.50, 2.20]
α_1 (dB/λ)	0.20	[0.01, 1.00]
α_2 (dB/λ)	0.20	[0.01, 1.00]
D (m)	130	[128, 132]
c_{w1} (m/s) at 0 m	1520	[1515, 1525]
c_{w2} (m/s) at D	1510	[1505, 1515]

Table 8.1: True values and uniform prior bounds for the environmental parameters of the simulated Mediterranean environment.

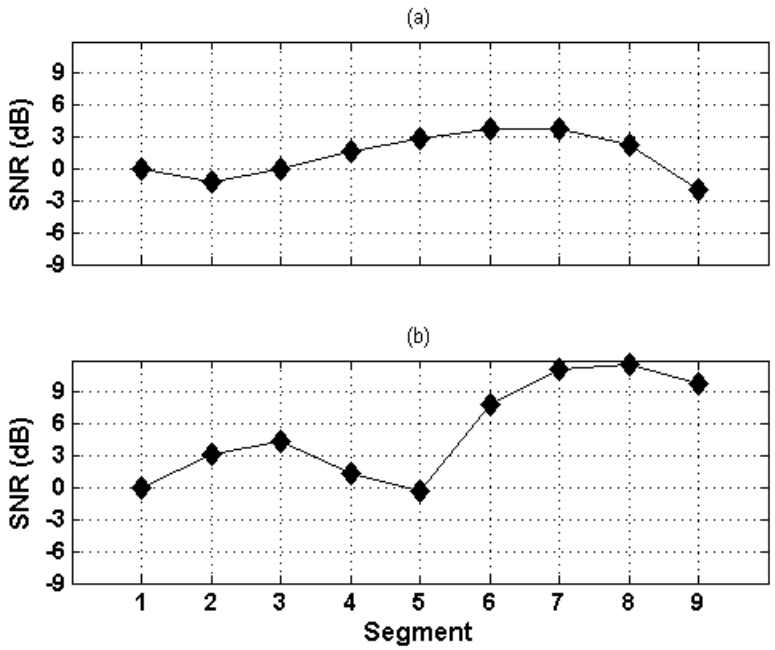

Figure 8.1: SNR versus track segment (relative to 0 dB at start of track) at frequency 300 Hz for (a) Track 1, and (b) Track 2 in the Mediterranean environment.

Table 7.1 lists the true values and bounds of uniform priors applied for environmental parameters of the continental shelf environment (wide bounds applied for geoacoustic parameters, narrow bounds for SSP parameters), and uniform prior bounds for bearing model parameters applied in all test cases. Constraints on horizontal and vertical

velocities are 9 and 0.067 m/s respectively. Numerical grids with 50 m spacing in range and 2 m spacing in depth are used for source positions. The grids extend over 0.3–6.0 km in range, and 4–122 m in depth (4–112 m for the continental shelf environment).

8.3.2. Mediterranean environment source tracking

Figure 8.2 shows range-depth PASs for Track 1 for a source at frequency 300 Hz at 1-dB average SNR. Results are for a sampling temperature of T=1; sampling at T=2 and T=3 provided PASs similar to those shown. True source ranges and depths are indicated with dotted lines. Regions of high probability extend over wide range intervals, indicating large range uncertainty. For the first track segments, the peaks of these high-probability regions are at ranges beyond the true range; for the following segments the high-probability regions are centred close to the true ranges. The high-probability regions are relatively narrow in depth, and indicate a shallow source. Figure 8.3 shows 2D marginal distributions for range and bearing (bearings to ±10º of endfire shown). The probability distributions are fairly symmetric around endfire. The bimodal structure of several of these distributions is a consequence of the inherent inability of a HLA for left-right discrimination. This structure is not seen for segments 5 to 7, for which bearing estimates are centred on 0º. Figure 8.4 shows the corresponding marginal distributions for bearing, from which the Viterbi track bearing is estimated.

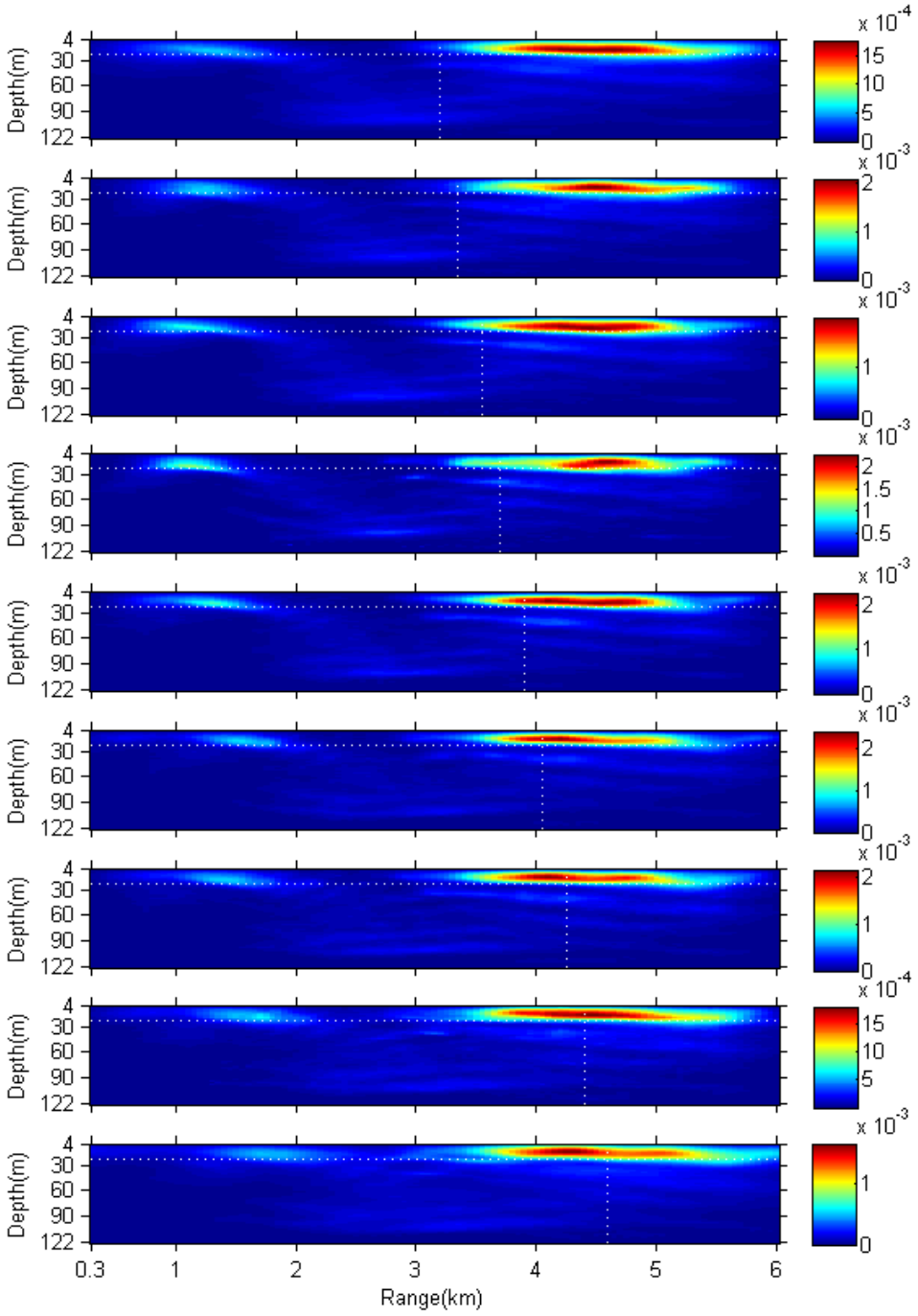

Figure 8.2: PASs computed for nine source positions along Track 1 for a 300-Hz source at +1-dB average SNR in the Mediterranean environment. True source ranges and depths are indicated by dotted lines. Note that each panel is normalized independently.

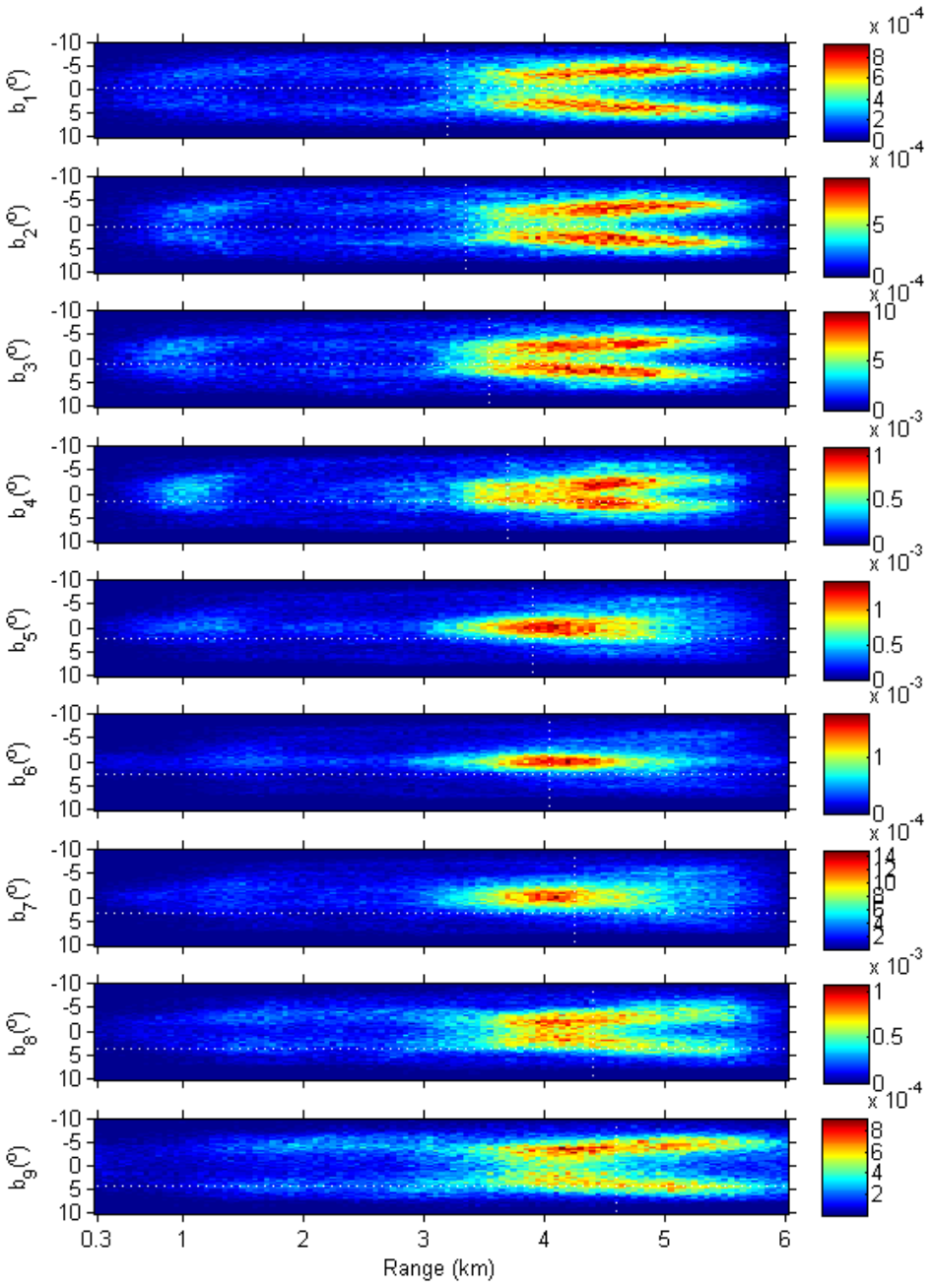

Figure 8.3: Two-dimensional marginal PPDs for range and bearing for the test case of Fig. 8.2 (bearings to ±10º of endfire shown). True source ranges and bearings are indicated by dotted lines.

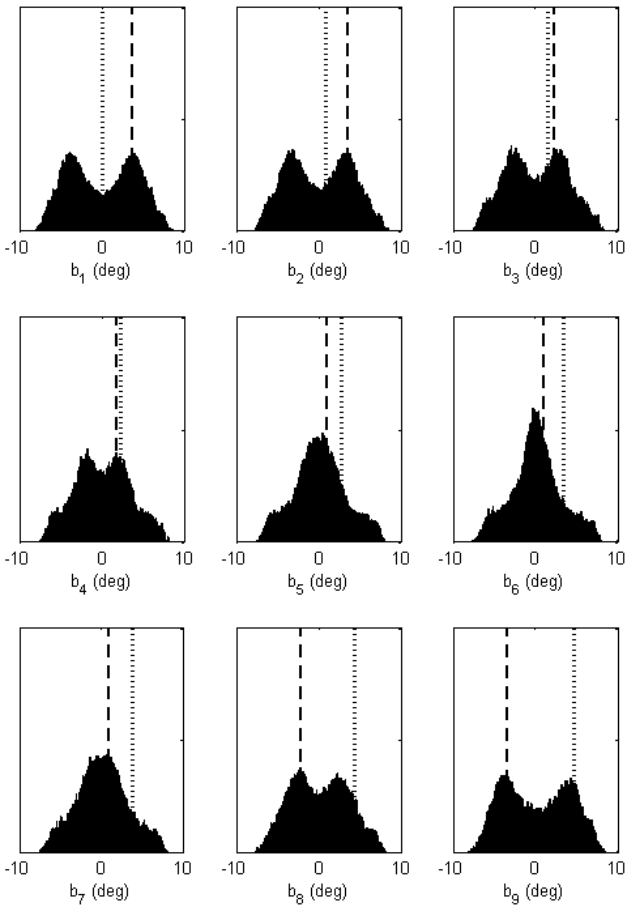

Figure 8.4: Marginal PPDs for track bearing for nine source positions for the test case of Fig. 8.2. Dotted lines indicate true track bearings, thick broken lines indicate Viterbi track bearing estimates.

Figure 8.5 shows range-depth PASs for Track 2 for a source at frequency 300 Hz at –1-dB average SNR. Sampling at temperature T=2 was here required. Regions of high probability are elongated in range, with the width decreasing as the source moves to closer range and towards array broadside, and extend in depth from approximately the true depth to the seabed. Figure 8.6 shows 2D marginal distributions for range and bearing (±10º around true bearing shown). The regions of high probability are narrow in bearing and centred approximately at the true bearings. Note that whereas the prior for

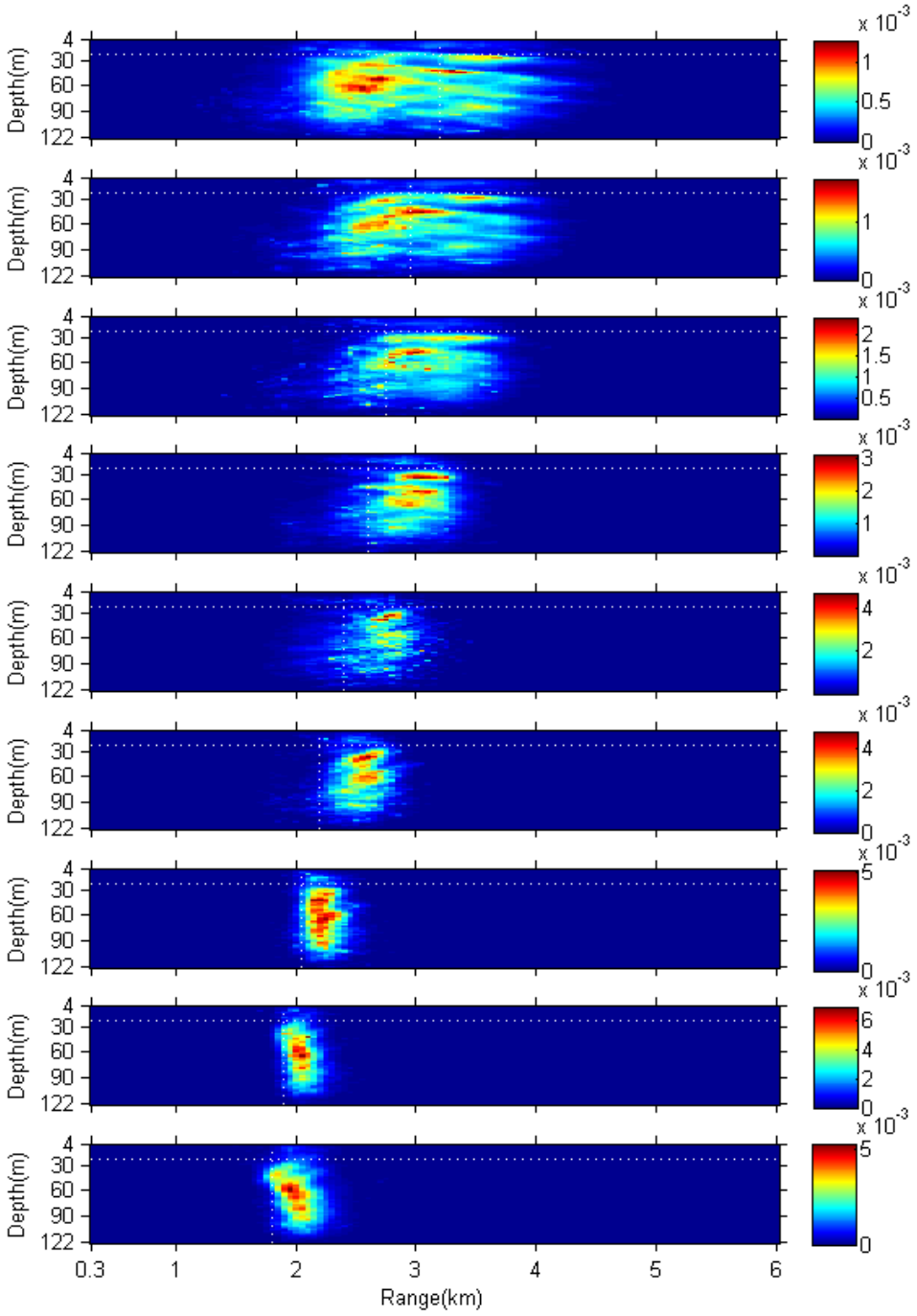

Figure 8.5: PASs computed for nine source positions along Track 2 for a 300-Hz source at –1-dB average SNR in the Mediterranean environment. True source ranges and depths are indicated by dotted lines. Note that each panel is normalized independently.

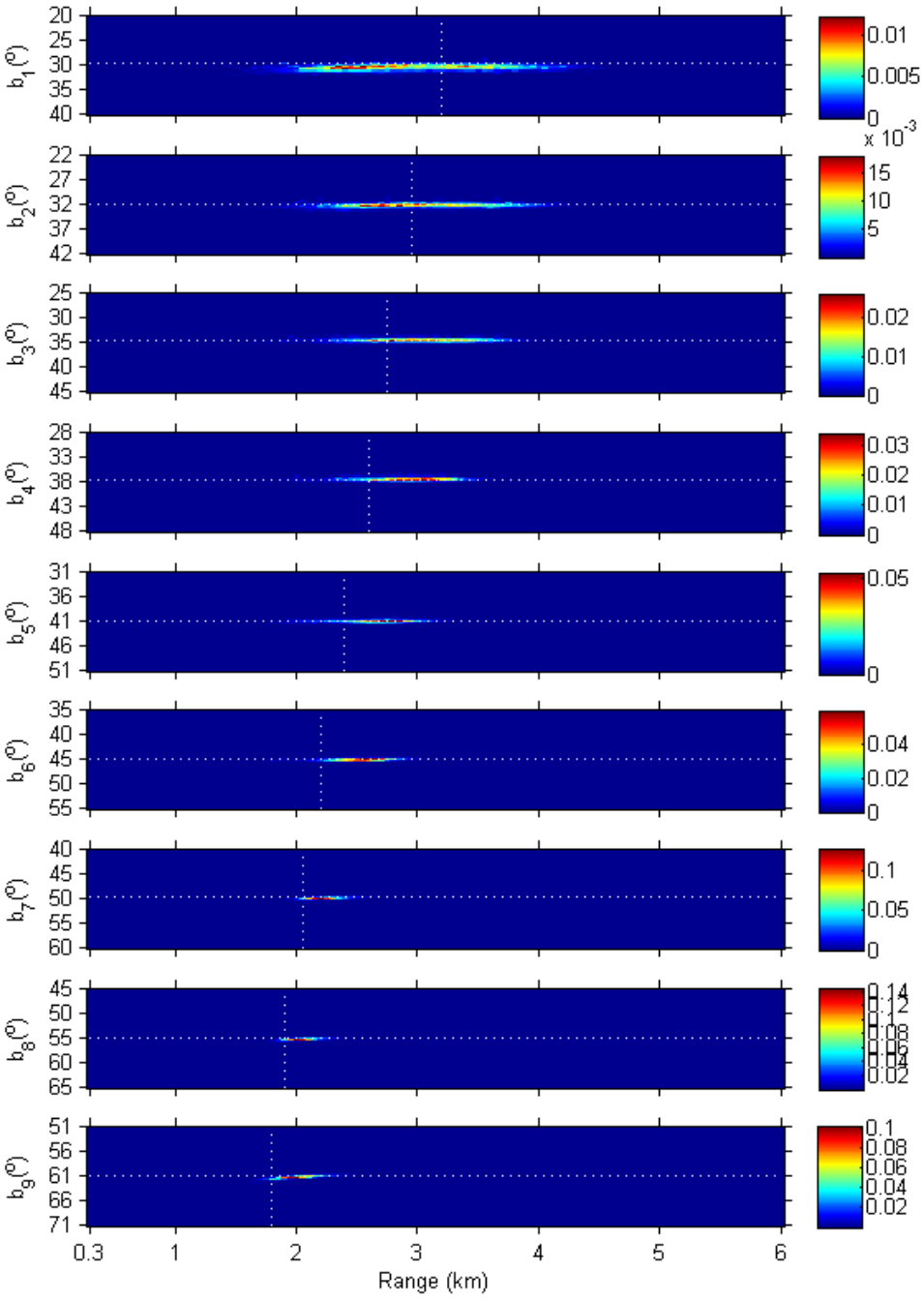

Figure 8.6: Two-dimensional marginal PPDs for range and bearing for the test case of Fig. 8.5 (bearings to ±10º of true shown). True source ranges and bearings are indicated by dotted lines.

bearing is uniform over the interval –180º to 180º, the sampling (initiated at the MAP track) did not reach negative bearings for this case.

Figures 8.7(a)-(b) and 8.7(d)-(e) show the Viterbi track estimates together with mean absolute-deviation uncertainties in range, depth, and bearing, for Tracks 1 and 2 respectively. The figures also show the MAP track estimates (via focalization-tracking), and the true tracks. For Track 1, the Viterbi track is at somewhat greater range and shallower depth than true. Mean range uncertainty is 989 m, mean depth uncertainty is 25 m; within these uncertainties, the Viterbi track encompasses the true track. The MAP track estimate has large errors in range and depth. The Viterbi track is reasonably close to the true track in bearing, but crosses endfire and predicts the wrong direction of motion. Bearing uncertainty is relatively large; within this uncertainty, however, the Viterbi track encompasses the true track in bearing. For Track 2, the Viterbi track is close to the true track in range, but has significant errors in depth. Range uncertainty decreases from approximately 590 m for the first track segment to 100 m for the last. The mean range and depth uncertainties are 270 m and 25 m, respectively; within these uncertainties, the Viterbi track encompasses the true track. The MAP track estimate is a poorer approximation to the true track in range, and has larger depth errors than the Viterbi track. The Viterbi track is close to the true track in bearing, with small uncertainty. Figures 8.7(c) and 8.7(f) show the 3D integrated probability (IP) for an acceptable position estimate, taken to be within 600 m in range, 6 m in depth, and 3º in bearing of the true source positions. The IP values are low (<0.1), but well above the reference level for a flat PAS (0.0004), representing no information on source positions.

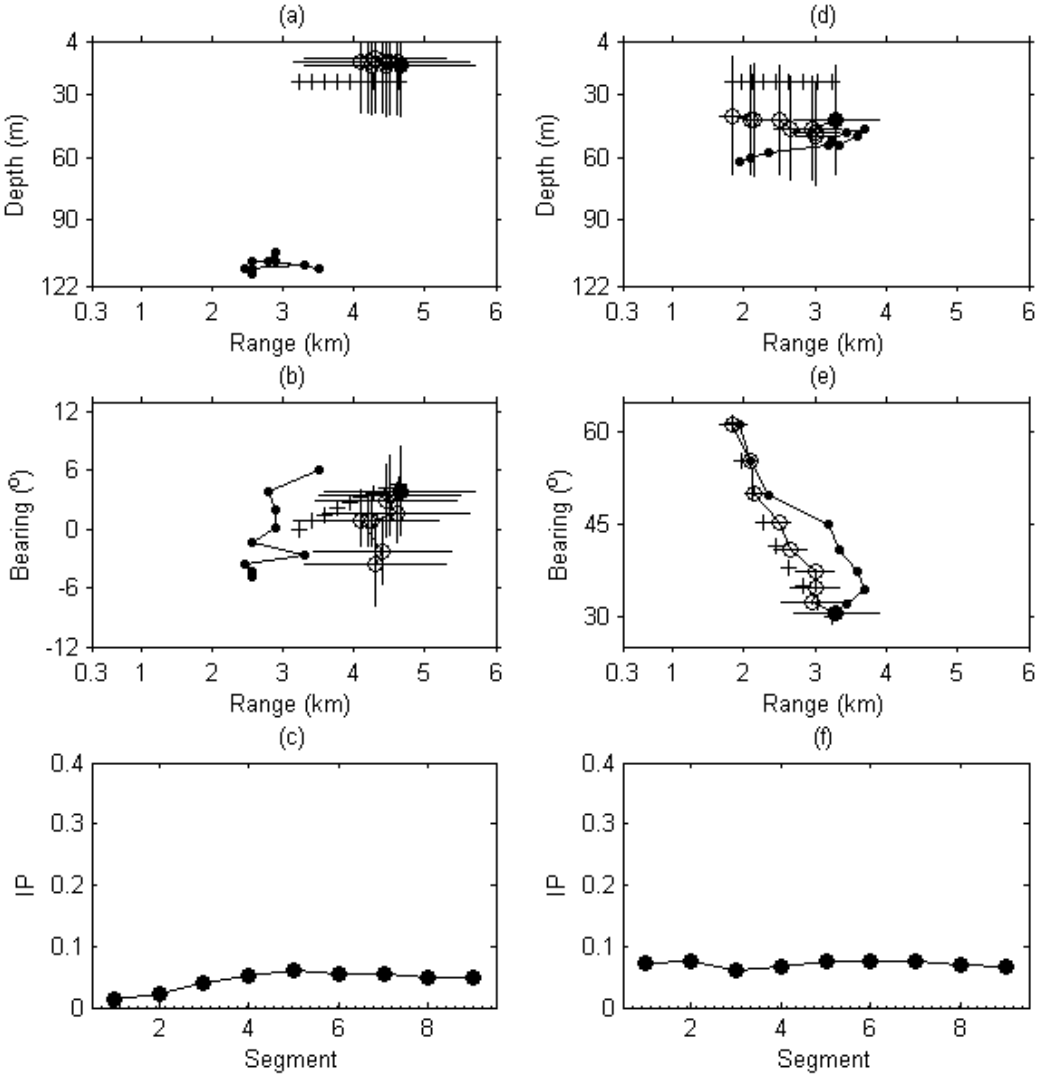

Figure 8.7: Mediterranean environment: (a)–(c) Track 1 at +1-dB average SNR, and (d)–(f) Track 2 at –1-dB average SNR. (a) and (d) range-depth plots of true track (crosses), Viterbi track (open circles, filled circle indicates track start point), and MAP track (small filled circles). Vertical and horizontal lines indicate depth and range uncertainties. (b) and (e) range-bearing plots of true track, Viterbi track, and MAP track. Vertical and horizontal lines indicate bearing and range uncertainties. (c) and (f) 3D integrated probability within 6 m in depth, 600 m in range, and 3º in bearing of true source positions. Dotted line indicates IP value for a flat distribution.

Environment	Case	MAP track r (m)	MAP track z (m)	MAP track b (º)	Viterbi track r (m)	Viterbi track z (m)	Viterbi track b (º)
Mediterranean	1	1097	87	3.4	580±989	10±25	3.4±3.4
	1-*fu*	-	-	-	635±837	8±10	-
	1-*ft*	-	-	-	177±1063	5±9	-
	2	512	30	0.3	145±270	20±25	0.2±0.2
Continental shelf	1	190	2	2.9	145±535	2±12	3.1±5.7
	2	284	30	0.3	58±179	3±7	0.3±0.3

Table 8.2: Mean track range (r), depth (z), and bearing (b) errors and uncertainties for synthetic data tracking via focalization-tracking (MAP track) and marginalization-tracking (Viterbi track). See text for explanation of test cases. (Case 1-*fu* is Track 1 for fixed bearing/unknown environment; case 1-*ft* is for fixed bearing/true environment.)

Table 8.2 summarizes track errors of MAP tracks, and track errors and uncertainties for the Viterbi tracks. Overall, marginalization-tracking gives better track estimates than focalization-tracking; within uncertainties, the Viterbi tracks encompass the true tracks.

8.3.3. Effects of prior uncertainty

Effects of prior bearing and environmental uncertainty were further investigated for Track 1. Figure 8.8 shows range-depth PASs obtained for marginalization-tracking with bearing fixed to the least-squares approximation to true and with unknown environmental parameters (left column), and PASs obtained with fixed bearing and true environmental parameters (right column). With fixed bearing/unknown environment, the regions of high probability have smaller extent in range and depth and are (for most track segments) located nearer to the true source range than with unknown bearing/unknown environment (Fig. 8.2). With fixed bearing/true environment, the regions of highest probability are

centred close to the true positions for all track segments, with additional probability at shorter ranges and deeper depths for all track segments. The regions of highest probability are more concentrated, and with higher peak probability, than with fixed bearing/unknown environment. (The additional probability at shorter ranges and deeper depths likely result from the PASs being computed for a fixed environment, whereas marginalizing over the environment tends to smooth out such features.)

Figure 8.9 shows the Viterbi tracks, uncertainties, and IPs for the two cases, and Table 8.2 summarizes track errors and uncertainties. With fixed bearing/unknown environment, range uncertainty changes little from the unknown bearing/unknown environment case (from 989 m to 837 m), while depth uncertainty decreases from 25 m to 10 m, and IP values increase from <0.1 to approximately 0.2. With fixed bearing/true environment, range uncertainty increases to 1063 m, depth uncertainty decreases to 9 m, and IP values increase to approximately 0.3. The range and depth errors reduce significantly from 580 m and 10 m, respectively, for unknown bearing/unknown environment to 177 m and 5 m, respectively, for fixed bearing/true environment. Thus, although track errors decrease and IP increases with known bearing/true environment, it appears that neither prior bearing uncertainty nor prior environmental uncertainty is the only cause of the somewhat poor range localization results for this test case.

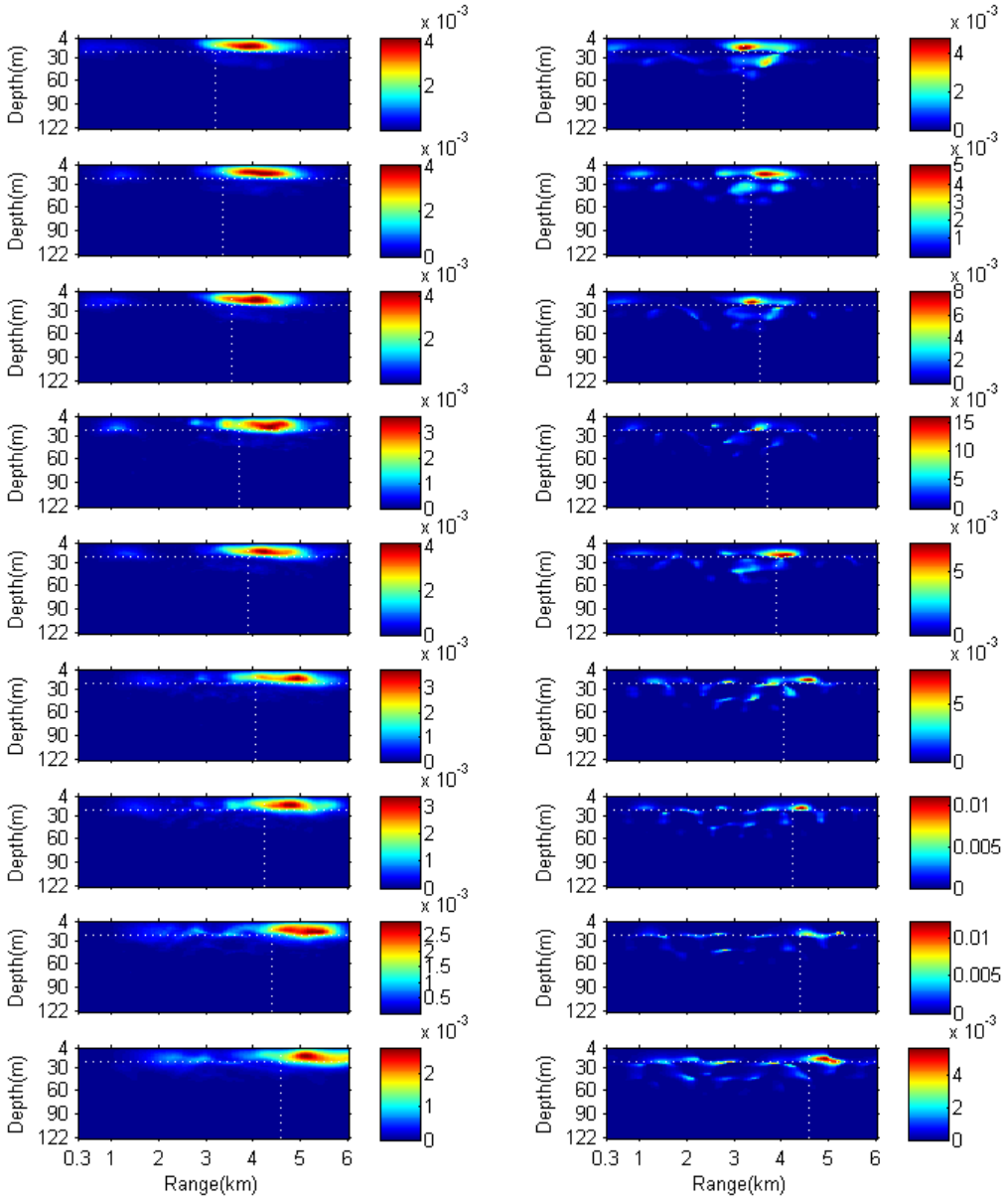

Figure 8.8: PASs computed for nine source positions along Track 1 for a 300-Hz source at +1-dB average SNR in the Mediterranean environment, with (left column) fixed bearing and unknown environment, and (right column) fixed bearing and true environment.

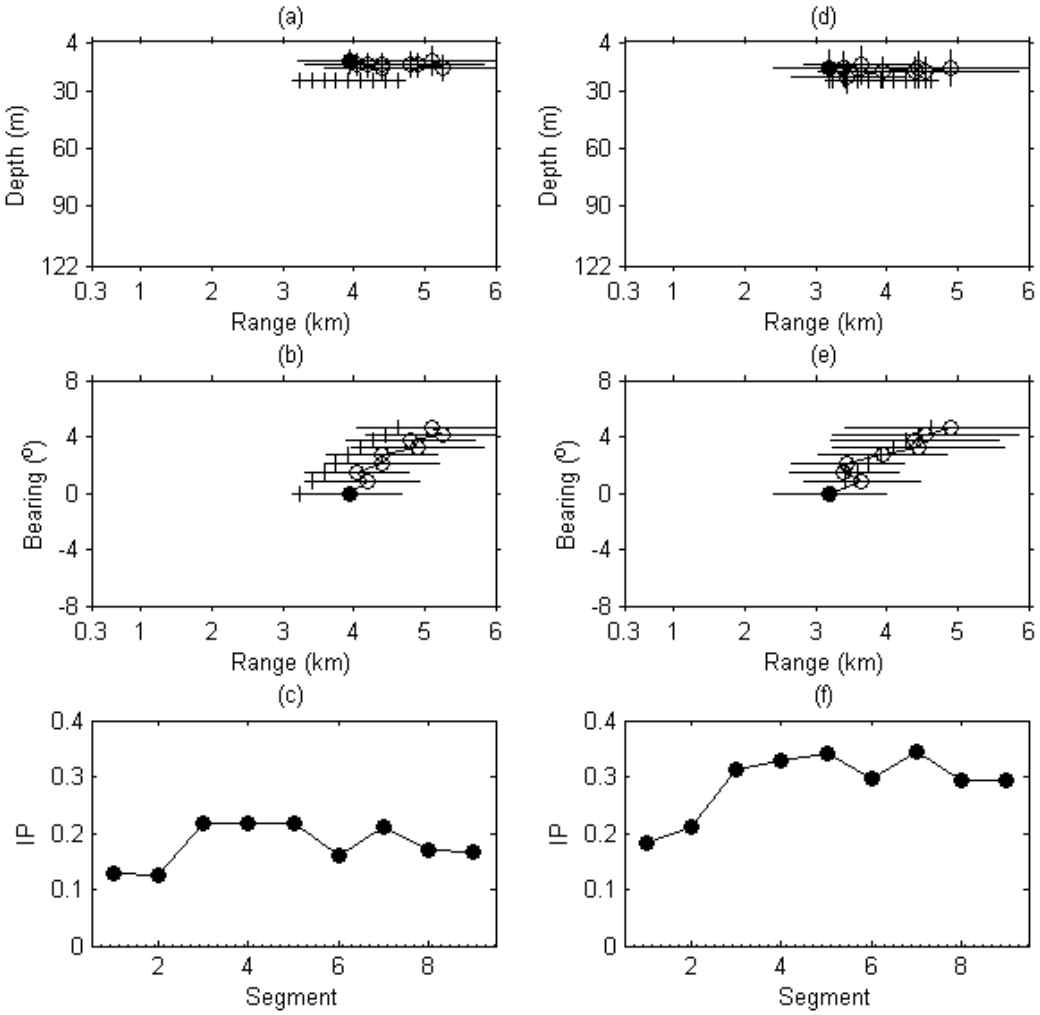

Figure 8.9: As Fig. 8.7, Track 1, but with (a)–(c) fixed bearing and unknown environment, and (d)–(f) fixed bearing and true environment.

8.3.4. Environmental parameter estimates and correlations

Although geoacoustic parameter estimates and resolution are not the primary goals of this chapter, it is of interest to see how well these parameters are defined as a by-product of the tracking algorithm. Figure 8.10 shows marginal PPDs for selected environmental model parameters (Track 1). In general, environmental parameters are not well resolved.

There is a peak in the sediment sound speed c_1 at approximately 1475 m/s, and a second peak at approximately 1530 m/s, which corresponds to the basement sound speed c_2. There is a peak in the basement sound speed at 1530 m/s. Mean values with mean absolute deviation widths for sound speeds c_1 and c_2 are 1495±24 m/s, and 1573±36 m/s, respectively. The other environmental parameters are poorly determined, as indicated by wide marginal distributions.

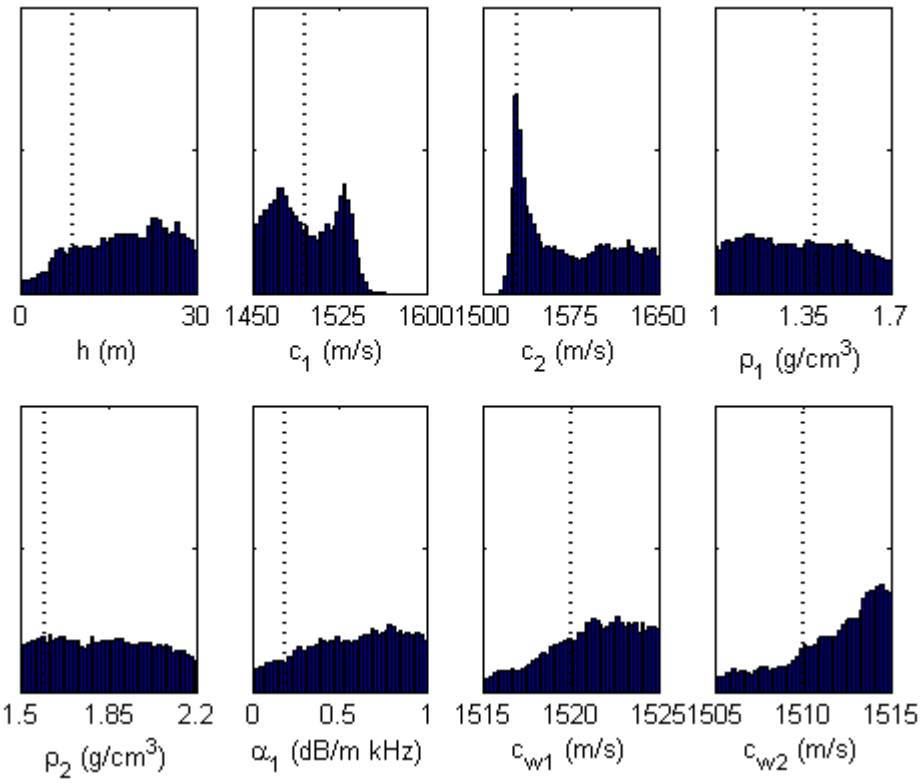

Figure 8.10: Marginal PPDs for selected environmental model parameters the test case of Fig. 8.2. Dotted vertical lines indicate true model parameter values.

Figure 8.11 shows the correlation matrix for all environmental parameters and source coordinates. There is weak positive correlation between c_2 and h, indicating that the data have difficulty in differentiating between thin-sediment/slow-basement and thick-sediment/fast-basement sound speed models. There are strong positive correlations

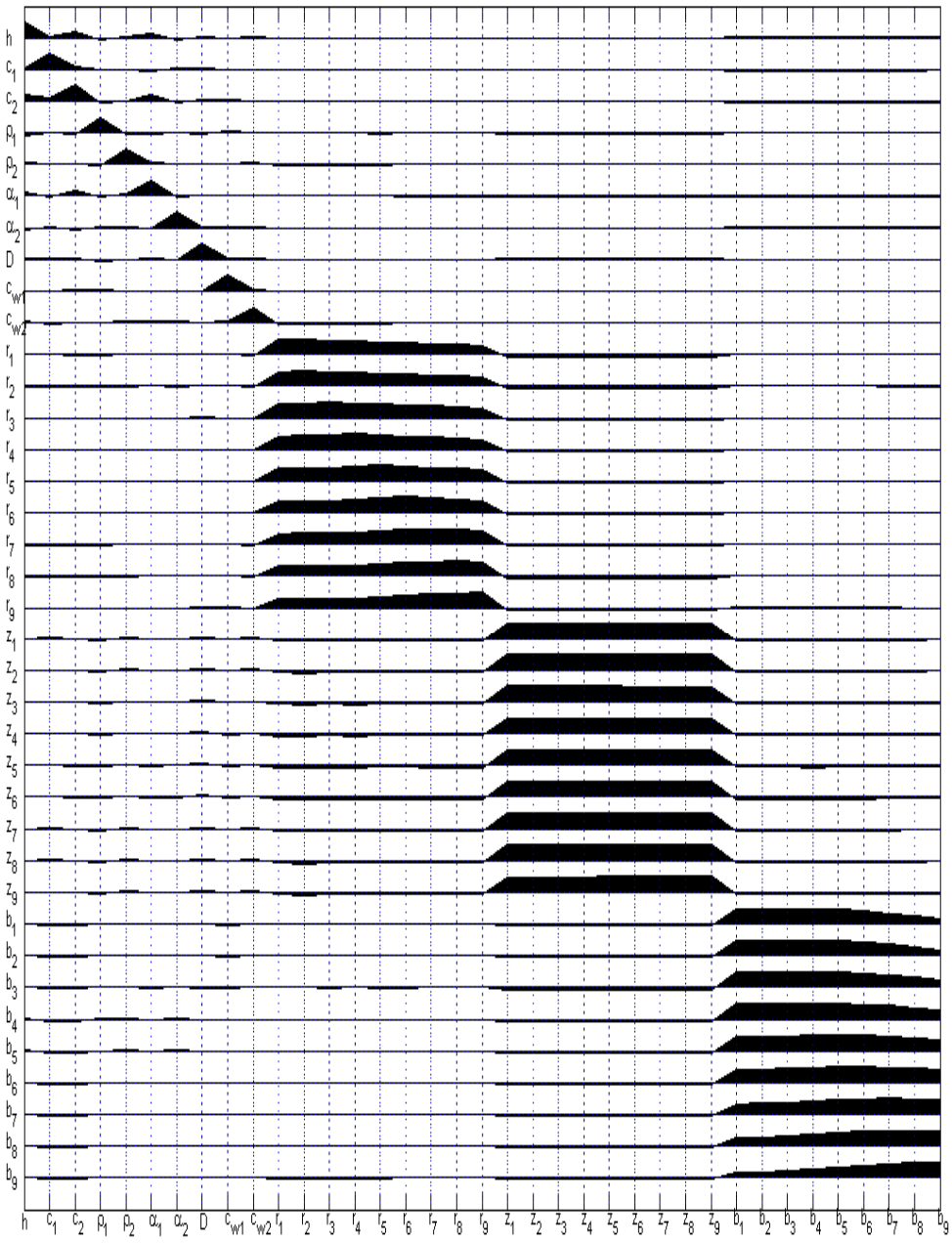

Figure 8.11: Correlation matrix for environmental parameters and source coordinates the test case of Fig. 8.2.

between all range coordinates, between all depth coordinates, and between all bearing coordinates, with correlations decreasing with track segment separation in each case. These coordinate correlations are consequences of the track constraints and the bearing model. The figure also shows that there are some important inter-coordinate correlations. For example, there is weak negative correlation between range and depth for each track segment, indicating some difficulty resolving range-depth ambiguities. This is consistent with the result of too-far range estimates and too-shallow depth estimates obtained. Finally, correlations between environmental parameters and source coordinates are small.

8.3.5. Continental Shelf environment source tracking

This section considers test cases for a source at frequencies of 200 and 300 Hz in the continental shelf environment. Track 1 at –1-dB average SNR and Track 2 at –4-dB average SNR (dB-average over frequencies and track segments) are considered. The cases were chosen for direct comparison of tracking results with those obtained for focalization-tracking in Chapter 7.

Figure 8.12 (left column) shows range-depth PASs for Track 1 for sampling temperature T=2. (Note that the panels show sub-sections of the full search grid in range and depth; there is low probability at grid points outside those shown.) The regions of highest probability are concentrated in range and depth (slightly extended in range). Except for the two last track segments, with lowest SNR, these peaks are centred close to the true track positions in range and depth. Additional lower-probability peaks are seen for all track segments. Figure 8.12 (right column) shows PASs for Track 2 (sampling

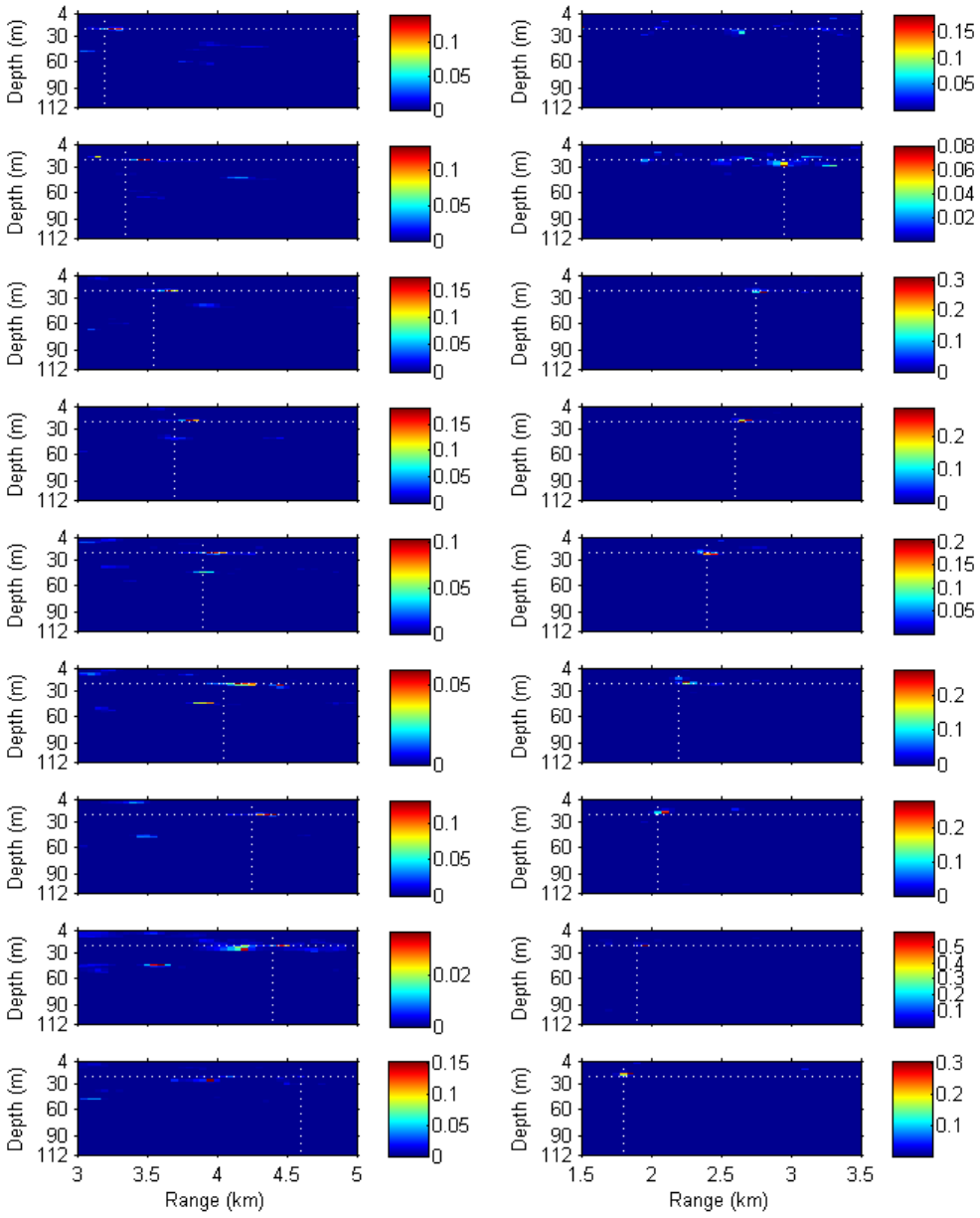

Figure 8.12: PASs computed for nine source positions for: Track 1 for a source at 200 and 300 Hz at –1-dB average SNR (left column), and Track 2 at –4-dB average SNR (right column), in the continental shelf environment. True source ranges are indicated by dotted lines. Note that each panel is normalized independently and that sub-sections of the full search grid in range are shown.

temperature T=2). The probability is highly concentrated in range and depth, close to the true ranges/depths. For the first three (lowest-SNR) track segments, there is some probability also at shorter ranges.

Despite differences in source frequencies and SNR, the distinct differences in results in terms of PASs (i.e., tight regions of high probability) from those obtained for the Mediterranean environment (i.e., wider regions of high probability) can in part be related to different characteristics of acoustic propagation in the two environments. The hard continental shelf seabed supports many propagating modes in the water column, which facilitates precise source localization. In the soft-seabed Mediterranean environment, however, the number of propagating modes is less; this contributes to reduced precision in source localization.

Figures 8.13(a)-(b) and 8.13(d)-(e) show the Viterbi tracks together with uncertainties in range, depth, and bearing. The figures also show the MAP track estimates, and the true tracks. Table 8.2 lists track errors and uncertainties. For Track 1, the Viterbi track provides a good approximation to the true track in range and depth, with mean range uncertainty of 535 m and mean depth uncertainty of 12 m. The Viterbi track also provides a good approximation to the true track in bearing, with some deviation from the true track for the farthest track segments; bearing uncertainty is relatively large. The MAP track provides a good approximation to the true track in range, depth, and bearing. For Track 2, excellent agreement is achieved between the Viterbi track and the true track in range, depth, and bearing. The range uncertainty is 179 m, depth uncertainty is 7 m, while bearing uncertainty is small. The MAP track is at incorrect depth, and provides a poorer approximation to the true track than the Viterbi track. Figures 8.13(c) and 8.13(f)

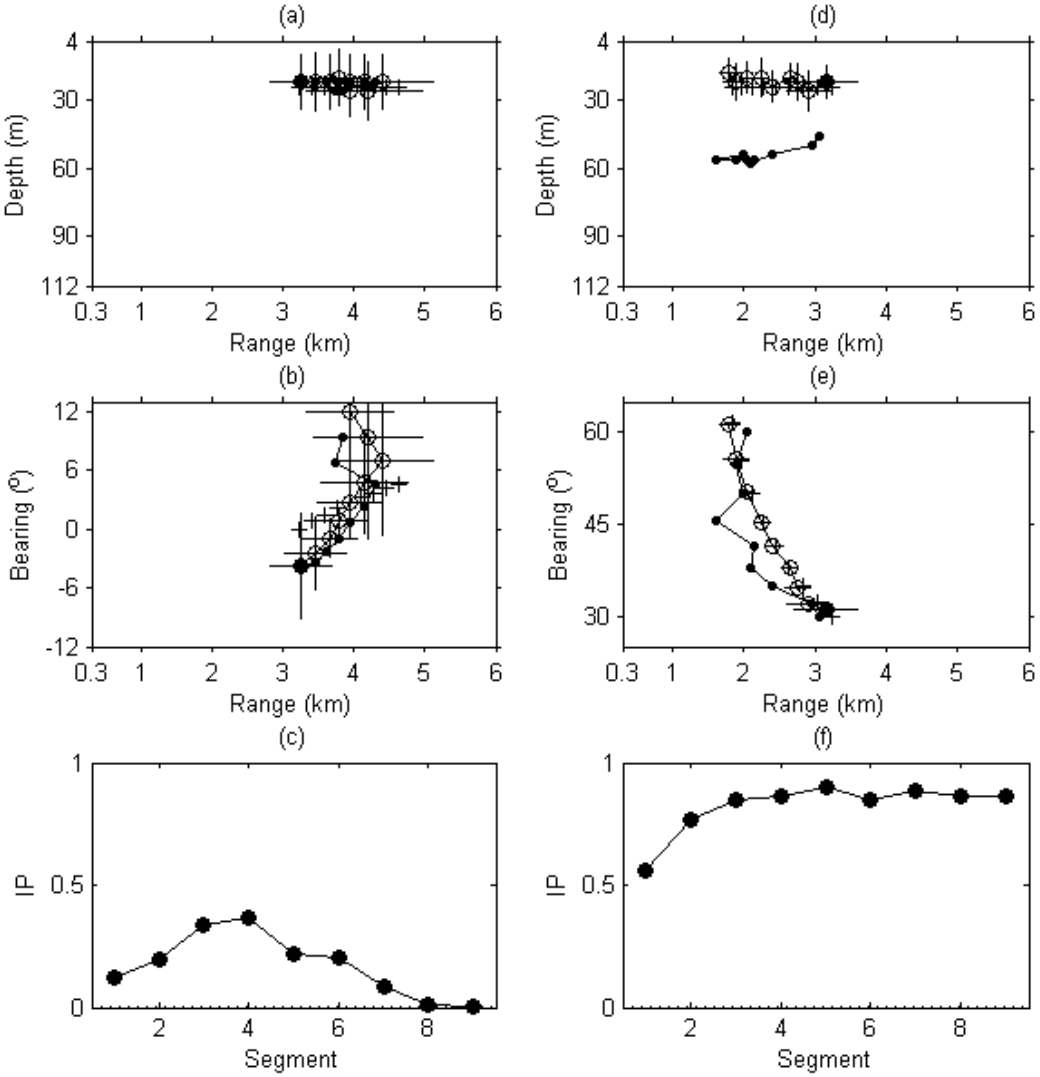

Figure 8.13: Continental Shelf environment: (a)–(c) Track 1 at –1-dB average SNR, and (d)–(f) Track 2 at –4-dB average SNR. (a) and (d) range-depth plots of true track (crosses), Viterbi track (open circles, filled circle indicates track start point), and MAP track (small filled circles). Vertical and horizontal lines indicate depth and range uncertainties. (b) and (e) range-bearing plots of true track, Viterbi track, and MAP track. Vertical and horizontal lines indicate bearing and range uncertainties. (c) and (f) 3D integrated probability within 6 m in depth, 600 m in range, and 3º in bearing of true source positions. Dotted line indicates IP value for a flat distribution.

show the 3D integrated probability. The relatively high IP values are a consequence of the PASs concentrated around the true source locations. (For Track 1, low IP values for the last track segments are due to bearing error. For Track 2, range errors at the first two segments yield lower IP values.)

The examples of this section illustrate excellent source tracking performance with the 3D marginalization-tracking algorithm for cases where the MAP track estimates (via 3D focalization-tracking) were less accurate or inaccurate. This agrees with a statistical study of Dosso and Wilmut (2009) for 2D tracking with a VLA.

8.4. Experimental source tracking results

This section presents results from application of the 3D marginalization-tracking algorithm to selected experimental data from the Barents Sea 03 data set. The primary goals are to compare tracking results with those obtained with the 3D focalization-tracking algorithm, and to quantify uncertainties in position estimates. Two data sets are considered: towed-source data at range 4.0–4.7 km at a frequency of 80 Hz, and ship noise at range 5.1–5.8 km at three frequencies (40 Hz, 50 Hz, and 144 Hz). Each data set is comprised of nine data segments extending over a time span of 4 min 42 s over which the source/ship moved approximately 755 m in range. Signal processing was done as described in Chapter 7.4. The estimated average SNR was 3.3 dB for the towed-source data and 0 dB for the ship noise.

The assumptions on the data error statistics were checked by performing *a posteriori* tests on data residuals. The KS test was applied to test for Gaussianity, with no evidence

against the hypothesis of Gaussian-distributed errors at a 0.05 level of significance in 95% of test cases for controlled-source data and 91% of test cases for ship noise. The runs test provided no evidence against spatial randomness (i.e., between elements of the HLA) at a 0.05 level of significance in approximately 95% of test cases for both data sets.

The model environment consists of a water column with a known SSP over a two-layer seabed (Fig. 2.3). Prior bounds for the eight unknown environmental parameters are listed in Table 5.1. Numerical grids with 50 m spacing from 1 to 9 km in range and 2 m spacing from 6 to 270 m in depth were used for source coordinates. Constraints on horizontal and vertical velocities were 6 and 0.067 m/s respectively. Sampling was initiated at the MAP tracks/models. Sampling temperatures of T=2 were required to sample widely over the range-depth grids; sampling at T=1 did not escape from the vicinity of the starting model tracks.

Figure 8.14 shows range-depth PASs for tracking with towed-source data. Note that the panels show sub-sections of the full search grid in range and depth; there is negligible probability at grid points outside those shown. The PASs are concentrated with unimodal peaks of high probability, somewhat elongated in range but fairly concentrated in depth. The peaks are less than 100 m in range beyond the true ranges. Figure 8.15 shows range-depth PASs for tracking with ship noise (sub-sections of the full search grid in range and depth shown). The PASs are concentrated with peaks of high probability; the peaks are less than 150 m in range beyond the true ranges.

Figures 8.16(a)-8.16(b) and 8.16(d)-8.16(e) show the Viterbi tracks with uncertainties, together with the MAP track estimates, and the true tracks. Figures 8.16(c) and 8.16(f)

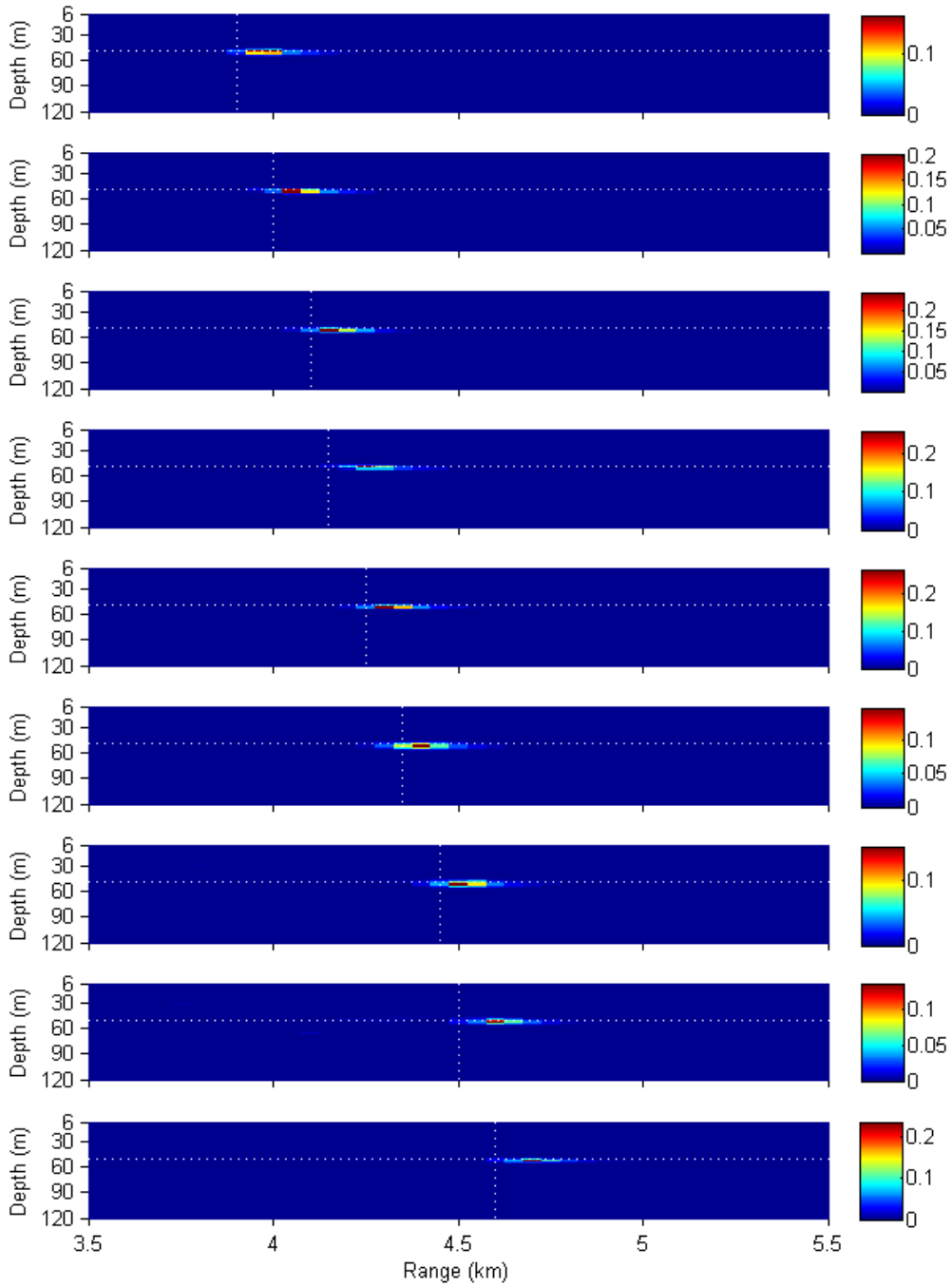

Figure 8.14: PASs computed for nine source positions for Barents Sea towed-source data. True source ranges and depths are indicated by dotted lines. Note that each panel is normalized independently, and that a sub-section of the full search grid in range and depth is shown.

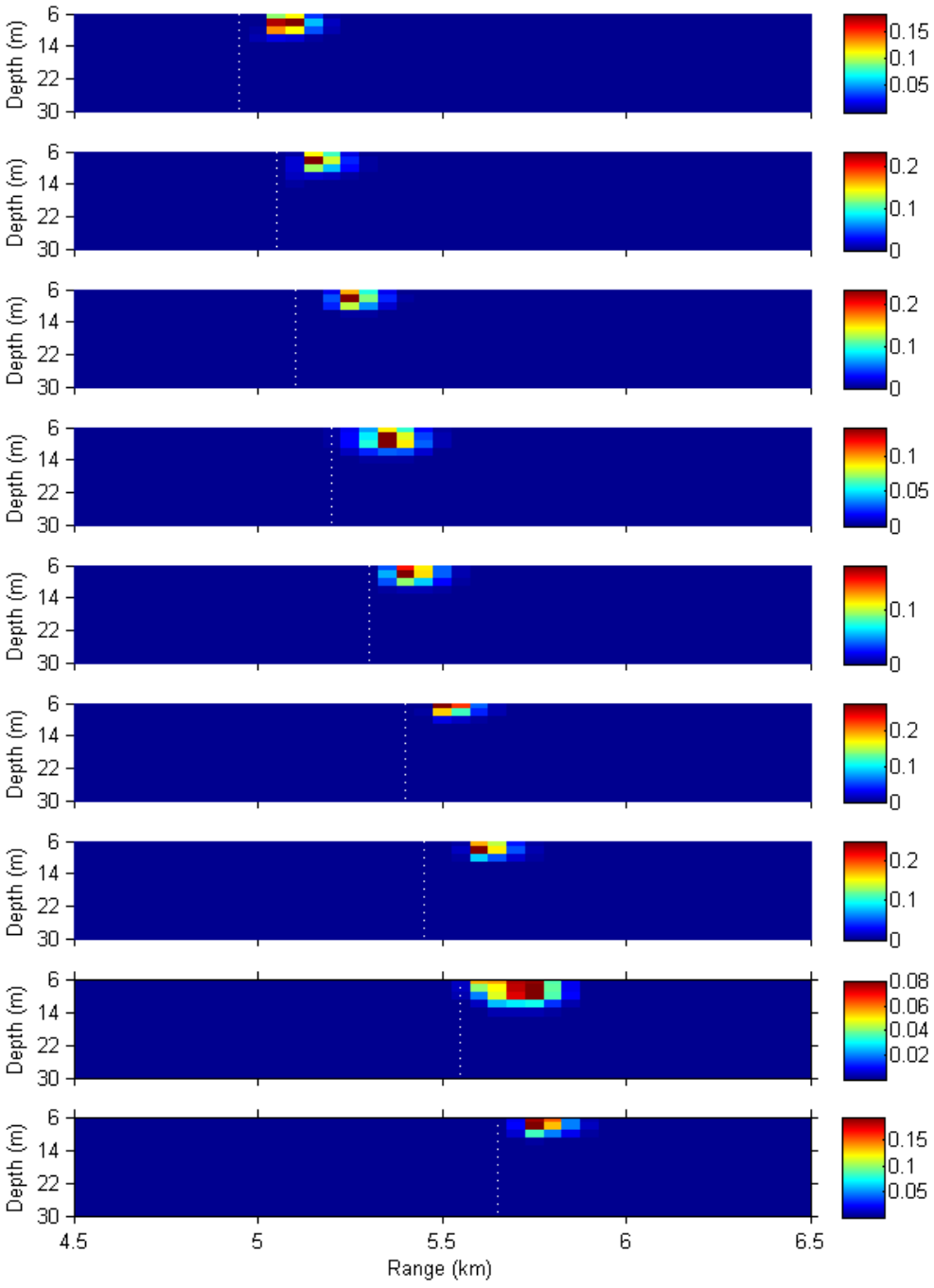

Figure 8.15: PASs computed for nine source positions for Barents Sea ship-noise data. True source ranges are indicated by dotted lines. Note that each panel is normalized independently, and that a sub-section of the full search grid in range and depth is shown.

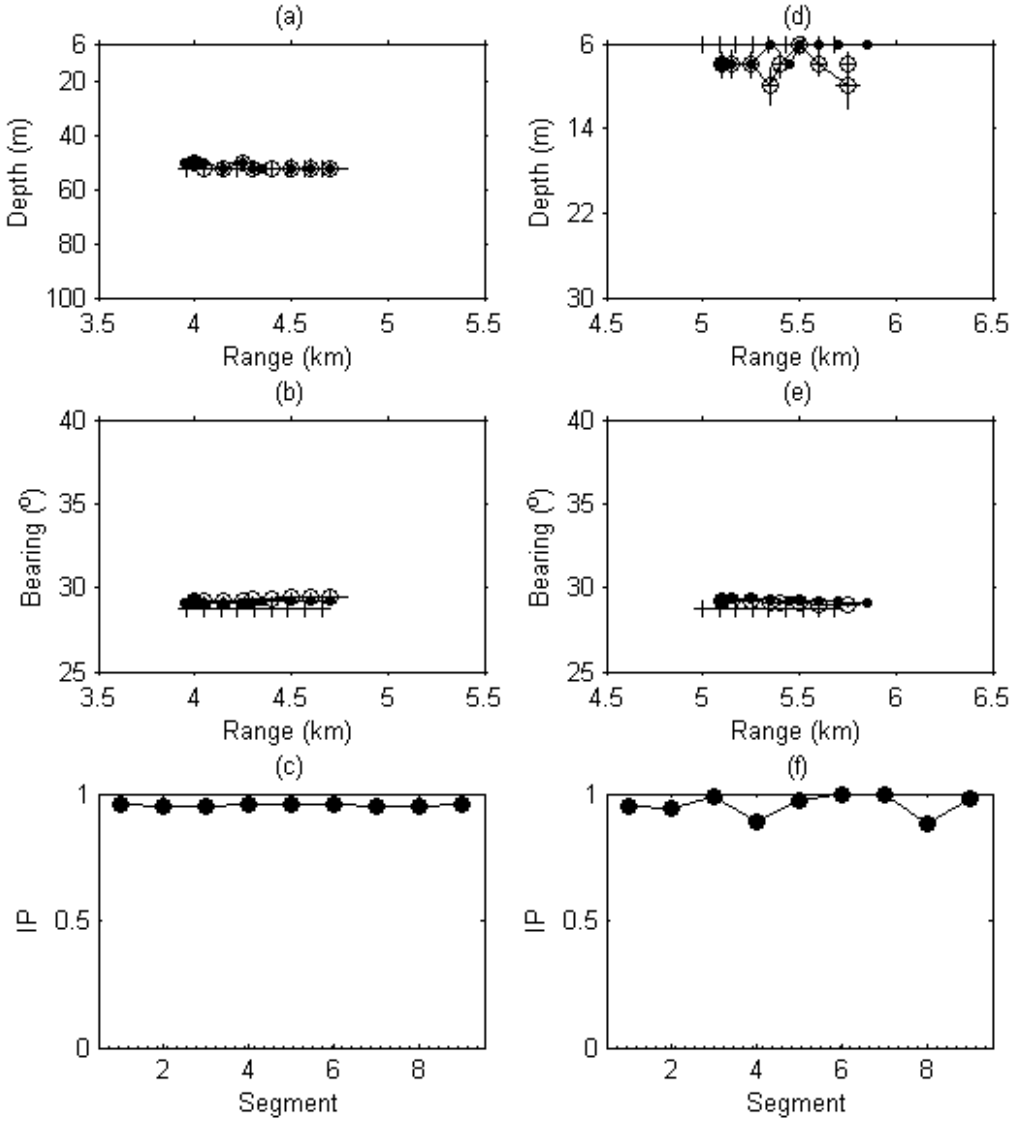

Figure 8.16: 3D tracking results for Barents Sea data: (a)–(c) towed-source, and (d)–(f) ship-noise. (a) and (d) range-depth plots of true track (crosses), Viterbi track from 3D marginalization-tracking (open circles), and MAP track from 3D focalization-tracking (small filled circles). Vertical and horizontal lines indicate depth and range uncertainties. (b) and (e) range-bearing plots of true track, Viterbi track, and MAP track. Vertical and horizontal lines indicate bearing and range uncertainties. Note that sub-areas of the full search grids/bounds in range, depth, and bearing are shown. (c) and (f) 3D integrated probability within 6 m in depth, 600 m in range, and 3º in bearing of true source positions.

show IP values; for both data sets these are close to unity, indicating very low uncertainty in the source position/depth estimates from the 3D marginalization-tracking algorithm.

Table 8.3 summarizes mean track errors for the Viterbi and MAP tracks, and mean absolute-deviation uncertainties in range, depth, and bearing for the Viterbi track. Track errors are measured with respect to the measured source position/depth for the towed-source data and ship stern position/propeller depth for the ship-noise data. Assumed uncertainties in these measurements are on the order of 50 m and 2 m, respectively (see Chapter 7.4).

	MAP track			Viterbi track		
	r (m)	*z* (m)	*b* (º)	*r* (m)	*z* (m)	*b* (º)
Towed source	22	0.7	0.4	21±73	0.5±2.5	0.5±0.2
Ship noise	161	0.7	0.4	83±36	2.2±1.3	0.3±0.1

Table 8.3: Mean track range (*r*), depth (*z*), and bearing (*b*) errors and uncertainties for Barents Sea data tracking via focalization-tracking (MAP track) and marginalization-tracking (Viterbi track).

For the towed-source data, the mean range and depth errors of the Viterbi track are 21 m and <1 m, respectively, with uncertainties of 73 m and ~3 m, respectively. These track errors are approximately equal to the MAP track errors, and less than the uncertainties in measured source positions and depths. For the ship noise, the mean range and depth errors of the Viterbi track are 83 m and ~2 m, respectively, with uncertainties of 36 m and ~1 m, respectively. The corresponding MAP track errors are 161 m and ~1 m. The Viterbi track here provides an appreciably better approximation than the MAP track to the true track in range. Finally, it is noteworthy that the Viterbi track

uncertainties are overall small, of the same order as the track errors as well as the uncertainties in measured source positions and depths.

8.5. Summary

This chapter developed and applied a 3D marginalization-tracking algorithm for application to HLA data. The algorithm integrates the PPD over unknown environmental parameters and source locations via a combination of Metropolis-Hastings sampling for environmental and bearing model parameters and Gibbs (heat-bath) sampling for source range and depth, with a priori track constraints on source velocity applied. Two-dimensional marginal distributions for source range/depth and source range/bearing, and marginal distributions for source bearing and environmental model parameters were derived. The Viterbi algorithm is applied to obtain the most probable 3D track, with uncertainties estimated from the marginal distributions.

The 3D marginalization-tracking algorithm was applied to simulated data in two synthetic environments: a soft-sediment seabed (Mediterranean) environment, and a hard-sediment (continental shelf) environment. Results for soft-sediment test cases indicated relatively large localization uncertainty; this uncertainty was related to the acoustic propagation characteristics in this environment, and shown not to be wholly attributable to prior bearing or environmental uncertainties. For the hard-sediment test cases, the marginalization-tracking algorithm provided excellent approximations to the true tracks, with small uncertainties in position estimates. In all cases, the marginalization-tracking algorithm provided better track estimates than the focalization-tracking algorithm, with

track position and depth errors within estimated uncertainties. Overall, these results demonstrate the utility of the 3D marginalization-tracking algorithm in application to HLA data. The algorithm was also applied to relatively low-SNR narrowband data from a towed submerged source and noise from a surface ship recorded on a bottom-moored HLA in the Barents Sea. The algorithm provided excellent approximations to the true source tracks with meaningful uncertainty estimates for both data sets.

Chapter 9 Summary and conclusion

This thesis applied a non-linear Bayesian method to matched-field inversion of horizontal line array data for seabed geoacoustic parameters, developed non-linear Bayesian approaches to three-dimensional tracking of a moving source in shallow water with uncertain environmental properties, and applied these methods to low-frequency experimental data collected with a bottom-moored HLA in the south-western Barents Sea.

Chapter 4 (Tollefsen and Dosso, 2007) examined the utility of HLAs for matched-field geoacoustic inversion with respect to array and experiment factors. A non-linear Bayesian inversion method was applied to synthetic data in realistic continental shelf environment scenarios that included high-level controlled sources and ship noise. The dependence of geoacoustic information content on array length and number of sensors was quantified in terms of widths of *a posteriori* marginal probability distributions of model parameters. It was observed that, for the environment studied, reasonable results in terms of well-defined geoacoustic parameter estimates were achieved for arrays of length at least approximately equal to the water depth and with at least a minimum number of sensors. The geoacoustic information content of an array meeting these requirements was shown to be comparable to that of a VLA spanning the water column. This is an important result in view of the previously often-perceived notion that MFI requires the use of a VLA. The study furthermore showed that, for longer arrays, the geoacoustic information content did not necessarily degrade as the source bearing moved

from endfire until the source is close to broadside. Finally, the study indicated that low-frequency ship-noise data can provide good geoacoustic inversion results.

Chapter 5 (Tollefsen, Dosso, and Wilmut, 2006) applied Bayesian geoacoustic inversion to controlled-source HLA data from the Barents Sea 03 experiment. A new approach was introduced to account for snapshot averaging in data error estimation, and effects of other approaches used in the literature, which may be considered either too optimistic or too pessimistic, were examined. Excellent agreement of the geoacoustic inversion results, in terms of consistent estimates and overlapping marginal probability distributions for seabed parameters, was obtained for data sets from several source positions at different ranges and bearings to the array. The estimates for the sediment sound-speed profile parameters and sediment density were in good agreement with independent geophysical measurements collected in the experiment, and with historic geophysical survey results from the south-western Barents Sea, further demonstrating the reliability of the inversion method.

Chapter 6 (Tollefsen and Dosso, 2008a) applied Bayesian geoacoustic inversion to ship-noise data from the Barents Sea 03 experiment. Ship noise allows for unobtrusive geoacoustic inversion, i.e., no new acoustic sources are introduced to the marine environment, and can have further potential interest to, e.g., long-term monitoring of seabed properties. A general problem with ship-noise data can be low SNR and few suitable frequency components for processing; this thesis showed that by combining data from multiple time segments in the inversion, uncertainty in geoacoustic parameter estimates can be significantly reduced. The geoacoustic inversion method employed furthermore allowed for meaningful comparison of results from inversions of different

data sets. The information content of noise from a relatively quiet research ship was shown to degrade with ship range and change in ship orientation (due to directional effects of the radiated noise), with smaller geoacoustic uncertainty for shorter ranges and for ship stern/propeller towards the array. Inversion results for short-range ship-noise data with the ship stern/propeller oriented towards the array were in excellent agreement with the results obtained from controlled-source data.

Chapter 7 (Tollefsen and Dosso, 2009) developed a non-linear Bayesian focalization approach to 3D tracking of a moving acoustic source in an uncertain environment. A simulation study investigated the performance of the algorithm as a function of track geometry, SNR, and prior environmental information. The performance in general increased with SNR and in several cases approached the results obtained with exact environmental knowledge. The effect of improved prior information on the environmental parameters was quantified and it was observed that, for the environment studied, improved prior information on seabed geoacoustic parameters allowed for wide prior bounds on water-column SSP parameters without significant degradation of tracking performance. The algorithm was applied to relatively low-SNR narrowband towed-source and ship-noise data from the Barents Sea 03 experiment, with excellent approximations to the true tracks of the source and ship obtained despite little prior information on seabed parameters.

Chapter 8 developed a non-linear Bayesian marginalization approach to 3D source tracking in an uncertain environment. The approach employed marginalization (integration) of the PPD over environmental parameters to obtain joint marginal distributions over source coordinates, from which the most probable 3D track was

extracted, and uncertainties in source positions were estimated. This required the application of an efficient PPD sampling algorithm based on the combination of Metropolis-Hastings sampling for environmental parameters and source bearing and Gibbs (heat-bath) sampling for source range and depth, the use of a proposal distribution that approximates the PPD, and non-unity temperature sampling. The approach was applied to test cases in two simulated environments, with track errors and uncertainties quantified. Marginalization-tracking generally provided better track estimates than the focalization-tracking algorithm, with track position and depth errors within estimated uncertainties. The approach was also applied to narrowband controlled-source and ship-noise data from the Barents Sea 03 experiment, with excellent approximations to the true source tracks and meaningful uncertainty estimates obtained for both data sets.

The overall goal of this thesis was to develop non-linear Bayesian methods for three-dimensional localization and tracking of a moving acoustic source in an ocean with uncertain environmental properties. As a precursor, Bayesian geoacoustic inversion was applied to estimate environmental parameters and their uncertainties, with specific application to horizontal line arrays of hydrophone sensors. Geoacoustic inversion applications reported to date have primarily used vertical line arrays and high-level controlled sources; this thesis demonstrated that inversion results of comparable quality can be obtained with horizontal line arrays and ship-noise sources. Inversion of controlled-source and ship-noise HLA data from the Barents Sea 03 shallow-water acoustic experiment provided sediment sound-speed profile and density estimates in good agreement with reference geophysical data. The ability to track a moving source in three dimensions despite environmental uncertainty is a new development of this thesis, and

provides a potentially important new capability for horizontal line arrays. The two new approaches, focalization-tracking and marginalization-tracking, provided excellent track estimates for Barents Sea 03 controlled-source and ship-noise data despite relatively low signal-to-noise ratio and little prior information on seabed parameters, and substantially outperformed alternative simpler tracking algorithms.

Bibliography

Arveson, P. T., and Vendittis, D. J. (2000), "Radiated noise characteristics of a modern cargo ship," *Journal of the Acoustical Society of America*, 107, 118-129.

Baggeroer, A. B., Kuperman, W. A., and Mikhalevsky, P. N. (1993), "An overview of matched field methods in ocean acoustics," *IEEE Journal of Oceanic Engineering*, 18, 401-424.

Barlee, R. M. S., Chapman, N. R., and Wilmut, M. J. (2005), "Geoacoustic model parameter estimation using a bottom moored hydrophone array," *IEEE Journal of Oceanic Engineering*, 30, 773-783.

Battle, D. J., Gerstoft, P., Hodgkiss, W. S., Kuperman, W. A., and Siderius, M. (2003), "Geoacoustic inversion of tow-ship noise via near-field matched-field processing," *IEEE Journal of Oceanic Engineering*, 28, 454-467.

Battle, D. J., Gerstoft, P., Hodgkiss, W. S., Kuperman, W. A., and Nielsen, P. L. (2004), "Bayesian model selection applied to geoacoustic inversion," *Journal of the Acoustical Society of America*, 116, 2043-2056.

Bhattacharyya, A. (1943), "On a measure of divergence between two statistical populations defined by their probability distributions," *Bulletin of the Calcutta Mathematical Society*, 35, 99-110.

Bhattacharyya, G. K., and Johnson, R. A. (1977), *Statistical Concepts and Methods*, New York: Wiley & Sons.

Bogart, C. W., and Yang, T. C. (1994), "Source localization with horizontal arrays in shallow water: Spatial sampling and effective aperture," *Journal of the Acoustical Society of America*, 96, 1677-1686.

Brooks, B. F., and Frazer, L. N. (2005), "Importance reweighting reduces dependence on temperature in Gibbs samplers: An application to the inverse coseismic geodetic problem," *Geophysical Journal International*, 161, 12-20.

Bucker, H. (1994), "Matched-field tracking in shallow water," *Journal of the Acoustical Society of America*, 96, 3809-3811.

Caiti, A., Jesus, S. M., and Kristensen, Å. (1996), "Geoacoustic seafloor exploration with a towed array in a shallow water area of the Strait of Sicily," *IEEE Journal of Oceanic Engineering*, 21, 355-366.

Chapman, N. R., Dizaji, R. M., and Kirlin, R. L. (2000), "Geoacoustic inversion using broad band ship noise," in *Proceedings of the Fifth European Conference on Underwater Acoustics*, edited by M. E. Zakharia, Lyon, France, pp. 787-792.

Collins, M. D., and Kuperman, W. A. (1991), "Focalization: Environmental focusing and source localization," *Journal of the Acoustical Society of America*, 90, 1410-1422.

Collins, M. D., Kuperman, W. A., and Schmidt, H. (1992), "Nonlinear inversion for ocean-bottom properties," *Journal of the Acoustical Society of America*, 92, 2770-2783.

Del Balzo, D. R., Feuillade, C., and Rowe, M. R. (1988), "Effects of water-depth mismatch on matched-field localization in shallow water," *Journal of the Acoustical Society of America*, 83, 2180-2185.

Dettmer, J., Dosso, S. E., and Holland, C. W. (2008), "Joint time/frequency-domain inversion of reflection data for seabed geoacoustic profiles and uncertainties," *Journal of the Acoustical Society of America*, 123, 1306-1317.

Dosso, S. E., Yeremy, M. L., Ozard, J. M., and Chapman, N. R. (1993), "Estimation of ocean-bottom properties by matched-field inversion of acoustic field data," *IEEE Journal of Oceanic Engineering*, 18, 232-239.

Dosso, S. E., Wilmut, M. J., and Lapinski, A. L. (2001), "An adaptive hybrid algorithm for geoacoustic inversion," *IEEE Journal of Oceanic Engineering*, 26, 324-336.

Dosso, S. E. (2002), "Quantifying uncertainty in geoacoustic inversion. I. A fast Gibbs sampler approach," *Journal of the Acoustical Society of America*, 111, 129-142.

Dosso, S. E., and Nielsen, P. L. (2002), "Quantifying uncertainty in geoacoustic inversion. II. Application to broadband, shallow-water data," *Journal of the Acoustical Society of America*, 111, 143-159.

Dosso, S. E., and Wilmut, M. J. (2002), "Quantifying data information content in geoacoustic inversion," *IEEE Journal of Oceanic Engineering*, 27, 296-304.

Dosso, S. E. (2003), "Environmental uncertainty in ocean acoustic source localization," *Inverse Problems*, 19, 419-431.

Dosso, S. E., and Wilmut, M. J. (2006), "Data uncertainty estimation in matched-field geoacoustic inversion," *IEEE Journal of Oceanic Engineering*, 31, 470-479.

Dosso, S. E., Nielsen, P. L., and Wilmut, M. J. (2006), "Data error covariance in matched-field geoacoustic inversion," *Journal of the Acoustical Society of America*, 119, 208-219.

Dosso, S. E., and Wilmut, M. J. (2007), "Bayesian focalization: Quantifying source localization with environmental uncertainty," *Journal of the Acoustical Society of America*, 121, 2567-2574.

Dosso, S. E., and Wilmut, M. J. (2008), "Uncertainty estimation in simultaneous Bayesian tracking and environmental inversion," *Journal of the Acoustical Society of America*, 124, 82-97.

Dosso, S. E., and Wilmut, M. J. (2009), "Comparison of focalization and marginalization for Bayesian tracking in an uncertain ocean environment," *Journal of the Acoustical Society of America*, 125, 717-722.

Eldholm, O., and Talwani, M. (1977), "Sediment distribution and structural framework of the Barents Sea," *Geological Society of America Bulletin*, 88, 1015-1029.

Fialkowski, L. T., Collins, M. D., Perkins, J. S., and Kuperman, W. A. (1997), "Source localization in noisy and uncertain ocean environments," *Journal of the Acoustical Society of America*, 101, 3539-3545.

Fialkowski, L. T., Perkins, J. S., Collins, M. D., Nicholas, M., Fawcett, J. A., and Kuperman, W. A. (2001), "Matched-field source tracking by ambiguity surface averaging," *Journal of the Acoustical Society of America*, 110, 739-746.

Fialkowski, L. T., Yang, T. C., Yoo, K., Kim, E., and Dacol, D. K. (2006), "Consistency and reliability of geoacoustic inversions with a horizontal line array," *Journal of the Acoustical Society of America*, 120, 231-246.

Gerstoft, P. (1994), "Inversion of seismoacoustic data using genetic algorithms and *a posteriori* probability distributions," *Journal of the Acoustical Society of America*, 95, 770-782.

Gerstoft, P., and Mecklenbräuker, C. F. (1998), "Ocean acoustic inversion with estimation of *a posteriori* probability distributions," *Journal of the Acoustical Society of America*, 104, 808-819.

Gilks, W. R., Richardson, S., and Spiegelhalter, D. J. (1996), *Markov Chain Monte Carlo in Practice*, Boca Raton: Chapman & Hall / CRC.

Gingras, D. F., and Gerstoft, P. (1995), "Inversion for geometric and geoacoustic parameters in shallow water: Experimental results," *Journal of the Acoustical Society of America*, 97, 3589-3598.

Hamilton, E. M. (1980), "Geoacoustic modeling of the sea floor," *Journal of the Acoustical Society of America*, 68, 1313-1340.

Huang, C.-F., and Hodgkiss, W. S. (2004), "Matched Field Inversion of Low-Frequency Source Tow Data From the ASIAEX East China Sea Experiment," *IEEE Journal of Oceanic Engineering*, 29, 952-963.

Huang, C.-F., Gerstoft, P., and Hodgkiss, W. S. (2006), "Uncertainty analysis in matched-field geoacoustic inversion," *Journal of the Acoustical Society of America*, 119, 197-207.

Huang, C.-F., Gerstoft, P., and Hodgkiss, W. S. (2009), "Statistical estimation of source location in presence of geoacoustic inversion uncertainty," *Journal of the Acoustical Society of America*, 125, EL171-EL176.

Ingber, L. (1989), "Very fast simulated re-annealing," *Mathematical and Computer Modelling*, 12, 967-973.

Jesus, S. M., and Caiti, A. (1996), "Estimating geoacoustic bottom properties from towed array data," *Journal of Computational Acoustics*, 4, 273-290.

Jiang, Y.-M., Chapman, N. R., and Badiey, M. (2007), "Quantifying the uncertainty of geoacoustic parameter estimates for the New Jersey shelf by inverting air gun data," *Journal of the Acoustical Society of America*, 121, 1879-1894.

Kirkpatrick, S., Gelatt, C. D., and Vecchi, M. P. (1983), "Optimization by Simulated Annealing," *Science*, 220, 671-680.

Knobles, D. P., Koch, R. A., Thompson, L. A., Focke, K. C., and Eisman, P. E. (2003), "Broadband sound propagation in shallow water and geoacoustic inversion," *Journal of the Acoustical Society of America*, 113, 205-222.

Koch, R. A., and Knobles, D. P. (2005), "Geoacoustic inversion with ships as sources," *Journal of the Acoustical Society of America*, 117, 626-637.

Lepland, A. (2004), "Results of analytical tests on FFI 2003 sediment cores," Technical Report 2004.019, Geological Survey of Norway, Trondheim, Norway.

Lindsay, C. E., and Chapman, N. R. (1993), "Matched-field inversion for geoacoustic model parameters using adaptive simulated annealing," *IEEE Journal of Oceanic Engineering*, 18, 224-231.

Lurton, X. (2002), *An Introduction to Underwater Acoustics*, Berlin: Springer.

Mecklenbräuker, C. F., and Gerstoft, P. (2000), "Objective functions for ocean acoustic inversion derived by likelihood methods," *Journal of Computational Acoustics*, 8, 259-270.

Mosegaard, K., and Sambridge, M. (2002), "Monte Carlo analysis of inverse problems," *Inverse Problems*, 18, R29-R54.

Nelder, J. A., and Mead, R. (1965), "A simplex method for function minimization," *Computer Journal*, 7, 308-313.

Nicholas, M., Perkins, J. S., Orris, G. J., Fialkowski, L. T., and Heard, G. J. (2004), "Environmental inversion and matched-field tracking with a surface ship and L-shaped receiver array," *Journal of the Acoustical Society of America*, 116, 2891-2901.

Nielsen, R. O. (1991), *Sonar signal processing*, London: Artech House.

Ó Ruanaidh, J. J. K., and Fitzgerald, W. J. (1996), *Numerical Bayesian Methods Applied to Signal Processing*, New York: Springer-Verlag.

Orsi, T. H., and Dunn, D. A. (1991), "Correlations between sound velocity and related properties of glacio-marine Sediments: Barents Sea," *Geo-Marine Letters*, 11, 79-83.

Richardson, A. M., and Nolte, L. W. (1991), "*A posteriori* probability source localization in an uncertain sound speed, deep ocean environment," *Journal of the Acoustical Society of America*, 89, 2280-2284.

Robins, A. J. (1991), "Reflection of a plane wave from a fluid layer with continuously varying density and sound speed," *Journal of the Acoustical Society of America*, 89, 1686-1696.

Rutherford, S. R., and Hawker, K. E. (1978), "Effects of density gradients on bottom reflection loss for a class of marine sediments," *Journal of the Acoustical Society of America*, 63, 750-757.

Sættem, J., Rise, L., and Westgaard, D. A. (1991), "Composition and properties of glacigenic sediments in the southwestern Barents Sea," *Marine Geotechnology*, 10, 229-255.

Sambridge, M., and Mosegaard, K. (2002), "Monte Carlo methods in geophysical inverse problems," *Reviews of Geophysics*, 40, 1-29.

Sen, M., and Stoffa, P. L. (1995), *Global optimization methods in geophysical inversion*, Amsterdam: Elsevier.

Shorey, J. A., Nolte, L. W., and Krolik, J. L. (1994), "Computationally efficient Monte Carlo estimation algorithms for matched field processing in uncertain ocean environments," *Journal of Computational Acoustics*, 2, 285-314.

Shorey, J. A., and Nolte, L. W. (1998), "Wideband optimal *a posteriori* probability source localization in an uncertain shallow ocean environment," *Journal of the Acoustical Society of America*, 103, 355-361.

Siderius, M., Nielsen, P. L., and Gerstoft, P. (2002), "Range-dependent seabed characterization by inversion of acoustic data from a towed receiver array," *Journal of the Acoustical Society of America*, 112, 1523-1535.

Siderius, M., Nielsen, P. L., and Gerstoft, P. (2003), "Performance comparison between vertical and horizontal arrays for geoacoustic inversion," *IEEE Journal of Oceanic Engineering*, 28, 424-431.

Solberg, C. E. (2004), "Geoacoustic models for the 2003 antenna experiment area compiled from shallow seismic data," Technical Report 2004/01602, Norwegian Defence Research Establishment, Kjeller, Norway.

Tantum, S. L., and Nolte, L. W. (1998), "Tracking and localizing a moving source in an uncertain shallow water environment," *Journal of the Acoustical Society of America*, 103, 362-373.

Tantum, S. L., Nolte, L. W., Krolik, J. L., and Harmanci, K. (2002), "The performance of matched-field track-before-detect methods using shallow-water Pacific data," *Journal of the Acoustical Society of America*, 112, 119-127.

Telford, W. M., Geldart, L. P., and Sheriff, R. E. (1990), *Applied Geophysics*, Cambridge: Cambridge University Press.

Tollefsen, D. (2004), "Array element positioning - the 2003 array experiment," Technical Report 2004/01657, Norwegian Defence Research Establishment, Kjeller, Norway.

Tollefsen, D., Wilmut, M. J., and Chapman, N. R. (2005), "Estimates of geoacoustic model parameters from inversions of horizontal and vertical line array data," *IEEE Journal of Oceanic Engineering*, 30, 764-772.

Tollefsen, D., Dosso, S. E., and Wilmut, M. J. (2006), "Matched-field geoacoustic inversion with a horizontal array and low-level source," *Journal of the Acoustical Society of America*, 120, 221-230.

Tollefsen, D., and Dosso, S. E. (2007), "Geoacoustic information content of horizontal line array data," *IEEE Journal of Oceanic Engineering*, 32, 651-662.

Tollefsen, D., and Dosso, S. E. (2008a), "Bayesian geoacoustic inversion of ship noise on a horizontal array," *Journal of the Acoustical Society of America*, 124, 788-795.

Tollefsen, D., and Dosso, S. E. (2008b), "Geoacoustic inversion of noise from ships-of-opportunity with unknown position," *Canadian Acoustics*, 36, 178-179.

Tollefsen, D., and Dosso, S. E. (2009), "Three-dimensional source tracking in an uncertain environment," *Journal of the Acoustical Society of America*, 125, 2909-2917.

Tolstoy, A. (1989), "Sensitivity of matched field processing to sound-speed profile mismatch for vertical arrays in a deep water Pacific environment," *Journal of the Acoustical Society of America*, 85, 2394-2404.

Tolstoy, A. (1993), *Matched Field Processing for Underwater Acoustics*, Singapore: World Scientific.

Trevorrow, M. V., Vasiliev, B., and Vagle, S. (2008), "Directionality and maneuvering effects on a surface ship underwater acoustic signature," *Journal of the Acoustical Society of America*, 124, 767-778.

van Leijen, A. V., Hermand, J.-P., and Meyer, M. (2009), "Geoacoustic inversion in the north-eastern Caribbean using a hydrographic survey vessel as a sound source of opportunity," *Journal of Marine Systems*, 78, S333-S338.

Viterbi, A. J. (1967), "Error bounds on convolutional codes and an asymptotically optimum decoding algorithm," *IEEE Transactions on Information Theory*, 13, 260-269.

Walpole, R. E., Myers, R. H., Myers, S. L., and Ye, K. (2007), *Probability & Statistics for Engineers & Scientists*, Upper Sadle River, NJ: Pearson Prentice Hall.

Westwood, E. K., Tindle, C. T., and Chapman, N. R. (1996), "A normal mode model for acousto-elastic ocean environments," *Journal of the Acoustical Society of America*, 100, 3631-3645.

Westwood, E. K., and Koch, R. A. (1999), "Elimination of branch cuts from the normal mode solution using gradient half spaces," *Journal of the Acoustical Society of America*, 106, 2513-2523.

Wilmut, M. J., Ozard, J. M., and Brouwer, P. (1995), "Evaluation of two efficient target tracking algorithms for matched-field processing with horizontal arrays," *Journal of Computational Acoustics*, 3, 311-326.